Static and Dynamic Connectivity Analysis of Human Brain via Functional Magnetic Resonance Imaging

A THESIS
SUBMITTED TO THE FACULTY OF THE GRADUATE SCHOOL
OF THE UNIVERSITY OF MINNESOTA
BY

Bhaskar Sen

IN PARTIAL FULFILLMENT OF THE REQUIREMENTS
FOR THE DEGREE OF
DOCTOR OF PHILOSOPHY

Advisor: Prof. Keshab K. Parhi

July, 2020

Acknowledgements

Foremost, I would like to express my sincere gratitude to my advisor Prof. Keshab K. Parhi for his continuous support of my PhD study and research, for his patience, motivation, enthusiasm, insightful comments, hard questions and immense knowledge. His guidance helped me in all the time of research and writing of this thesis. I am thankful to my PhD committee members Prof. Emad Ebbini, Prof. Mingyi Hong and Prof. Catherine Qi Zhao for their comments and insightful questions regarding my PhD research.

My sincere thanks go to fellow lab mates and gradaute students at the University of Minnesota Twin Cities, Tingting Xu, Yin Liu, Sayed Ahmad Salehi, Zisheng Zhang, Sandhya Koteshwara, Shu-Hsien Chu, Sandeep Avvaru, Xingyi Liu, Nanda Kumar Unnikrishnan and Lulu Ge for helpful discussions during the course of study. I am thankful to my friends Adway and Son for making my stay in Minneapolis very welcoming. I am also grateful to my parents for their sacrifice and guidance throughout my life.

Finally, I would like to thank my partner Sijie for spending the past three years by my side, without her support and motivation this would not be possible.

Abstract

Functional connectivity of brain refers to statistical dependence of brain functions among often remote neuronal units. This thesis addresses two novel ways to analyse brain functional connectivity. We provide an entropy based technique called *sub-graph* entropy to classify brain states. This metric is then used to classify adolescents suffering from obsessive compulsive disorder. The thesis also proposes a new tensor based decomposition to analyse *dynamic* functional connectivity of brain. In comparison with *static* connectivity, *dynamic* analysis assumes that brain network evolves and changes over time. Finally, a combined *static-dynamic* feature extraction model is used to classify adolescents suffering from major depressive disorder.

The first part of the dissertation considers analysis of human brain networks or graphs constructed from time-series collected from functional magnetic resonance imaging (fMRI). In the network of time-series, the nodes describe the regions and the edge weights correspond to the absolute values of correlation coefficients of the time-series of the two nodes associated with the edges. A novel information-theoretic metric, referred as *sub-graph* entropy is introduced to measure uncertainty associated with a *sub-graph*. Nodes and edges constitute two special cases of *sub-graph* structures. Node and edge entropies are used to rank regions and edges in a functional brain network. This work analyzes task-fMRI data collected from 475 subjects in the Human Connectome Project (HCP) study for gambling and emotion tasks. The proposed approach is used to rank regions and edges associated with these tasks. The *differential* node (edge) entropy metric is defined as the difference of the node (edge) entropy corresponding to two different networks belonging to two different classes. Differential entropy of nodes and edges are used to rank top regions and edges associated with the two classes of data. Using top node and edge entropy features separately, two-class classifiers are designed using support vector machine (SVM) with radial basis function (RBF) kernel and leave-one-out method to classify time-series for emotion task *vs*. no-task, gambling task *vs*. no-task and emotion task *vs*. gambling task. Using node entropies, the SVM classifier achieves classification accuracies of 0.96, 0.97 and 0.98, respectively. Using edge entropies, the classifier achieves classification accuracies of 0.91, 0.96 and 0.94, respectively.

Next, we describe two pertinent properties of *sub-graph* entropy. It is shown that when a graph is divided into multiple smaller graphs, the summation of their *sub-graph* entropy is always less than a constant. Additionally, this summation is always greater than the corresponding graph entropy. We also demonstrate that node entropy, a special case of *sub-graph* entropy, is stable. Experiments using both synthetic data and real world brain network data are carried out to further validate these points. Overall, node entropy has better stability compared to other centrality metrics.

As a relevant application of *static* connectivity analysis, we present a novel approach for classifying obsessive-compulsive disorder (OCD) in adolescents from resting-state fMRI data. Currently, the state-of-the-art for diagnosing OCD in youth involves interviews with adolescent patients and their parents by an experienced clinician, symptom rating scales based on Diagnostic and Statistical Manual of Mental Disorders (DSM), and behavioral observation. Discovering signal processing and network-based biomarkers from functional magnetic resonance imaging (fMRI) scans of patients has the potential to assist clinicians in their diagnostic assessments of adolescents suffering from OCD. We investigate the clinical diagnostic utility of a set of *univariate*, *bivariate* and *multivariate* features extracted from resting-state fMRI using an *information-theoretic* approach in 15 adolescents with OCD and 13 matched healthy controls. Results indicate that an *information-theoretic* approach based on *sub-graph* entropy is capable of classifying OCD *vs.* healthy subjects with high accuracy. Mean time-series were extracted from 85 brain regions and were used to calculate Shannon wavelet entropy, Pearson correlation matrix, network features and *sub-graph* entropy. In addition, two special cases of *sub-graph* entropy, namely node and edge entropy, were investigated to identify important brain regions and edges from OCD patients. A leave-one-out cross-validation method was used for the final predictor performance. The proposed methodology using *differential sub-graph* (edge) entropy achieved an accuracy of 0.89 with specificity 1 and sensitivity 0.80 using leave-one-out cross-validation with in-fold feature ranking and selection. The high classification accuracy indicates the predictive power of the sub-network as well as edge entropy metric.

The second part of the thesis explores the predictive capability of *dynamic* functional connectivity extracted from functional magnetic resonance imaging of the human brain.

First, a number of state-of-the-art features extracted from *static* functional connectivity of brain are employed to predict biological gender and intelligence using publicly available Human Connectome Project (HCP) database. Next, a *novel* tensor parallel factor (PARAFAC) decomposition model is proposed to decompose sequence of *dynamic* connectivity matrices into common connectivity components that are orthonormal to each other, common time-courses, and corresponding distinct subject-wise weights. The subject-wise loading of the components are employed to predict biological gender and intelligence using a random forest classifier (respectively, regressor) using 5-fold cross-validation. The results demonstrate that *dynamic* functional connectivity can indeed classify biological gender with a high accuracy (0.94, where male identification accuracy was 0.87 and female identification accuracy was 0.97). It can also predict intelligence with smaller normalized mean square error (0.139 for fluid intelligence and 0.031 for fluid ability metrics) compared with other functional connectivity measures (the nearest mean square error were 0.147 and 0.037 for fluid intelligence and fluid ability metrics, respectively using *static* connectivity approaches). Our work is an important milestone for the understanding of non-stationary behavior of hemodynamic blood-oxygen level dependent (BOLD) signal in brain and how they are associated with biological gender and intelligence. The paper demonstrates that *dynamic* behavior of brain can contribute substantially towards forming a fingerprint of biological gender and intelligence.

We further combine the *static* and *dynamic* approaches for classifying major depressive disorder (MDD) for adolescents from resting-state fMRI. This last part investigates various *static* and *dynamic* connectivity measures extracted from resting-state fMRI for assisting with MDD diagnosis. First, absolute pearson correlation matrices from 85 brain regions are extracted and they are used to calculate *static* features. An *information-theoretic* approach based on *sub-graph* entropy is found to classify MDD *vs.* healthy subjects with high accuracy. Next, approaches utilizing *dynamic* connectivity are employed to extract tensor-based, independent component based and principal component based subject specific attributes. Finally, features from *static* and *dynamic* approaches are combined to create a feature vector. A leave-one-out cross-validation method is used for the final predictor performance. Out of 49 adolescents with MDD and 33 matched healthy controls, a support vector machine (SVM) classifier using a radial basis function (RBF) kernel using *differential sub-graph* entropy combined with

dynamic connectivity features achieves an accuracy of 0.82 with specificity 0.79 and sensitivity 0.84 using leave-one-out cross-validation with in-fold feature ranking and selection. The high classification accuracy indicates the predictive power of combining the *static* and *dynamic* connectivity features for classification of adolescent MDD.

Contents

List of Tables

List of Figures

Chapter 1

Introduction

1.1 Background

When we walk, talk, listen or do any other work, several neuronal units of our brain work in conjunction to give rise to the particular behavior. Each unique behavior can be represented as a *state* in brain function and each *state* represents a specific pattern in brain connectivity. Finding patterns in those connectivity *states* are of utmost importance [5, 6]. Recently there has been a surge of interest in understanding brain connectivity pattern while a person performs a task through the use of network theory. Both the progress in complex network analysis and high resolution functional brain scans have helped marry these two seemingly different fields. This has progressed our understanding of human brain connectivity patterns corresponding to different unique behaviors or *states*. Although complex network measures have been applied to analyze brain connectivity networks, several areas within this particular sub-field remain unexplored. For example, there has been significant progress in *network information theory* in communication networks but its application to brain connectivity analysis has been slow. The main reason for this slow penetration might be due to the complexity of accurate calculation of the information-theoretic properties within brain networks.

In this research, we show that the use of *sub-graph* entropy and entropies of nodes and edges to analyze brain connectivity patterns can provide useful knowledge about the inner working complexity of brain for unique conditions or *states*. Moreover, this can facilitate the understanding of brain from the perspective of graph complexity. In the

later part of this thesis, we propose a new blind source separation algorithm using higher dimensional tensor decomposition to *dynamic* brain networks. We demonstrated that, the tensor components extracted from *dynamic* functional connectivity hold biologically interpretable regions and edges from human brain that are useful to discriminate traits like biological gender and intelligence performance.

1.1.1 Functional MRI (fMRI)

Functional magnetic resonance imaging (fMRI) provides a non-invasive way to measure activity of brain during resting state (rs-fMRI) or task (t-fMRI) for a person. Specifically, when a person is scanned, the change of blood-oxygen level density (BOLD signal) in the brain over time is measured. The resultant scan is a 4-D image where the first three dimensions are spatial and the fourth dimension is temporal. This provides an indirect way to measure the neuronal activities of the brain regions. When a subject performs a task, the corresponding regions associated with the task have a high inflow of oxygenated blood. This in turn gives rise to the so-called hemodynamic response in fMRI time series for the input impulse excitation. During t-fMRI, a subject is asked to perform a repetitive task to understand which part of the brain is involved in that particular task. For example, one experiment may investigate the brain regions involved while tapping the fingers. In this case, a healthy person while in scanner is asked to perform finger tapping at a particular interval (15 or 30 secs). This repetition ensures that we are able to filter out false positives found during the non-repetitive task by investigating the fMRI time series and identifying the regions corresponding to the repetitive task. In addition to a task, when a person is awake in rest condition, there are some regions in the brain that are always active (default mode network or DMN). During *resting-state* fMRI, the spontaneous regional interaction between brain regions are measured. This is due to the fact that even while not doing a task, some regions in brain are activated and this creates flow in BOLD signal. For many psychiatric diseases, the resting-state fMRI signal is highly meaningful as it is not confounded by any task based performance [7]. fMRI scans can consist of other signals (considered noise from neuroscience perspective), that involve breathing artifacts and eye-blinking etc. In this thesis we are only concerned about both the t-fMRI and rs-fMRI analysis.

1.1.2 Functional Connectivity

There are different ways to define brain connectivity. *Structural connectivity* refers to a range of physical links that connect a number of neuronal units. *Functional connectivity* captures patterns of deviations from statistical independence between distributed and often spatially remote neuronal units [8, 9]. Joint connectivity of brain graphs by combining structural and functional connectivity has also been investigated [10]. Deviations from statistical independence are generally taken to indicate *dynamic* coupling and can be measured, for example, by estimating the correlation or covariance, spectral coherence, or phase locking between pairs of time series. Unlike structural connectivity, functional connectivity is highly time dependent, and it can be statistically nonstationary. It is modulated by external task demands and sensory stimulation, as well as the internal *state* of the organism. The measurement of functional connectivity can be extracted from different brain imaging techniques like cellular recordings, electroencephalography (EEG), magnetoencephalography (MEG), functional magnetic resonance imaging (fMRI), or other techniques. Common tasks and behaviors induce a change in functional connectivity pattern in brain networks.

1.1.3 Static Connectivity

The emergence of fMRI as a tool to measure brain activities have facilitated the analysis of whole brain as a functional network of interconnected regions [11]. Here each region is a collection of neural elements that can be defined based on anatomy of brain tissues. Hence each region can be seen as a neuronal unit emitting a collective response of blood oxygen level dependent (BOLD) signal for an input excitation. The brain activities of each region are represented by different time series corresponding to different voxels and their average value can represent the behavior of the region over time. The whole brain is seen as an interconnected network communicating with each other through correlation in time or frequency. Thus *static* connectivity is captured through one-shot correlation of the mean time-series of different brain regions. This view is popular in fMRI literature and finds evidence through the works of [5, 12].

1.1.4 Dynamic Connectivity

A very interesting direction in fMRI neuroimaging study is the focus on variation over time in spatial coupling. *Dynamic* connectivity of brain refers to brain network that varies over time. This *dynamic* network can be captured through sliding window correlation matrices over mean time-series extracted from brain network [13]. Blind source separation (BSS) techniques, such as independent component analysis (ICA), nonnegative matrix factorization, and tensor decomposition, have been widely adapted in data-driven pattern studies [14–16]. Becasuse fMRI is spatio-temporal, one can conceive of the network of the spatial pattern to be *dynamic* instead of *static*. In an early example of this, an ICA was run on subsets of data over time to evaluate changes in the default mode network [16]. Because neither the temporal nor the spatial domain is constrained, the resulting decomposition successfully identifies the spatiotemporal dynamics in a data-driven manner. In this model, an atlas is used to parcellate the brain into spatial maps, each of which has its own characteristic time course. Next, time-varying changes among component time courses, called functional network connectivity (FNC) [17], is captured by calculating cross-correlation between brain networks (components) over time using windowing [18, 19]. Following this, ICA, IVA, PCA and k-means clustering are performed to find out the brain states. Although PCA and ICA are widely used for extracting *dynamic* functional connectivity, they suffer from two drawbacks. PCA decomposition constrains both connectivity maps as well as the time courses (activity level) of the maps to be orthogonal to other maps and time courses. This can severely hamper the expressiveness of model. ICA can overcome the orthogonality constraint in the time domain, although the uniqueness of spatial maps requires the sources to be non-Gaussian. Tensor decomposition can alleviate both concerns, as the required constraints can be added to a particular mode without affecting other modes.

1.2 Research Overview

This research focuses on the study of human brain network analysis using both *static* and *dynamic* functional connectivity approaches. A novel centrality metric is proposed for analysing *static* connectivity. This metric is then validated using classification performance to discriminate brain states. Also, the same metric is used to access brain

functional dysfunctions with applications for adolescent obsessive compulsive disorder (OCD). In the second part of the research, we propose a novel *dynamic* connectivity analysis approach using tensor decomposition. In this work, the new *dynamic* pattern analysis is employed for a number of classification and regression tasks. Furthermore, a joint *static-dynamic* approach is then employed to diagnose adolescent major depressive disorder (MDD) with high accuracy. Figure 1.1 shows the interdisciplinary research framework for the application of brain connectivity and network analysis.

Various signal processing, graph theory, machine learning and statistical analysis approaches are employed to process the neuroimaging data, and extract, select and validate discriminating features for diagnosing and understanding the illnesses. In the framework, neuroimaging data are firstly acquired from subjects. Raw data is preprocessed to remove noise, artifacts and other unwanted components images are reconstructed to characterize the brain functions. Advanced signal processing and graph theory approaches are employed to further process and model the preprocessed neuroimaging data, and create meaningful feature sets to characterize brain activity and neural connectome in terms of connectivity and network topological structure from different perspectives that are later used for machine learning and statistical analysis.

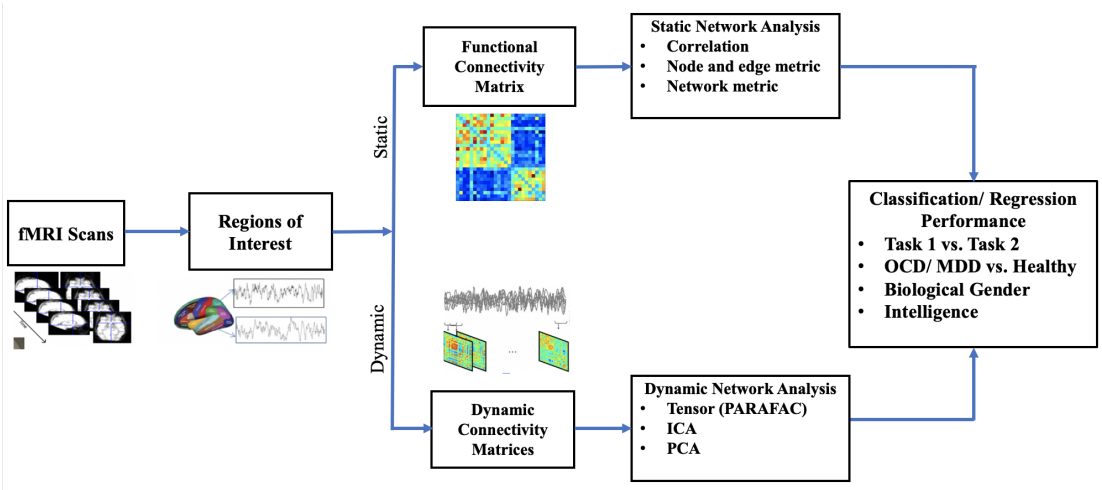

Figure 1.1: The framework of joint *static dynamic* approaches for classification of different biological traits.

From statistics point of view, boosting the number of features could lead to a significant number of type–I error by the multiple comparisons. Individual features showing high discriminating power or small p-value may be false discoveries due to multiple comparisons. Therefore, appropriate statistical tests are necessary to validate the significance of each feature and control the False Discovery Rate (FDR). In this work, we use Bonferroni correction for any statistical hypothesis testing. Additionally, permutation tests are carried out for understanding significance for the classifiers. Thus we employ application-specific statistical analysis methods, such as permutation tests and Network-based Statistics (NBS) and Bonferroni correction. Finally, the key features are interpreted using domain knowledge. For classification performance, accuracy, sensitivity and specificity are measured. For regression performance, mean squared error and mean absolute error are measured.

1.3 Summary of Contributions

The contribution of this research are in three directions. We proposed a new network centrality metrics in Chapter 2 and demonstrated that this centrality is able to discriminate between two brain states with high accuracy. Two main properties of this metric is described in Chapter 3. In Chapter 4, we proposed a new method to analyse *dynamic* functional connectivity. Specific contributions of each directions are described next.

1.3.1 Contribution of Chapter 2

Contributions of this chapter are three-fold. First, we propose the use of node and edge entropies as centrality metrics to compute the complexity of brain networks. Second, we propose ranking of nodes and edges of brain networks to extract *important* regions and edges between two *states*. We show that *sub-graph* entropy extracts some *important* regions, that the other network metrics can not identify. Third, using emotion and gambling t-fMRI data from the HCP dataset, we show that there is statistical difference of entropy measure between task *state vs.* no-task *state* and between two tasks. Node entropy and edge entropy are used as features to classify task *vs.* no-task or two different tasks with high accuracy. The proposed method outperforms other centrality measures for classifying two *states*. This validates the efficacy of *sub-graph* entropy as neural

correlates of *states* [20].

1.3.2 Contribution of Chapter 3

The contributions of this chapter are as follows. We derive the lower bound and upper bound for the summation of the *non-overlapping sub-graph* entropies from a bi-directional graph. We demonstrate that node entropy is stable in the sense that the difference in centrality values for a given node in two different graphs is bounded by a constant times the distance between these graphs. Furthermore, synthetic data and real world fMRI dataset are used to validate the results. It is shown that node entropy is more stable than strength, eigenvector and betweenness centrality.

1.3.3 Contribution of Chapter 4

The contribution of this chapter is to apply advanced rs-fMRI analytical approaches for analyzing rs-fMRI data to classify adolescents with OCD *vs.* healthy controls. We used time-series, absolute correlation coefficients and graph-theoretic properties of functional network for these classifications. Although many brain network statistics exist in the literature and have been used to rank regions (nodes) or functional connections (edges), the proposed approach has never been applied to brain networks for diagnosing psychiatric disorders. First we used *univariate* (*e.g.*, Shannon wavelet entropy of each time-series), *bivariate* (absolute value of Pearson correlation) and *multivariate* (network features, *e.g.*, *local efficiency, global efficiency* [21], [5], *clustering coefficient* [22], *betweenness centrality* [23], *modularity* [24], graph and *sub-graph* entropy [20]) features for predicting OCD. These measures describe *segregation* or *integration* within the network. Next, network measures such as *sub-graph* entropy [20] and specifically those of nodes and edges were used to rank important brain regions and edges in each group of brain networks. In addition, the nodes and edges were also ranked by the extent to which they differentiated groups. This led to extracting a sub-network containing 120 edges, which was used for classification of OCD *vs.* controls. We extracted a sub-network from resting-state fMRI data from two groups of adolescents that can predict whether a subject has OCD [25].

1.3.4 Contribution of Chapter 5

The chapter presents *yet* another method for extracting dFC from sliding window correlation using tensor decomposition. The uniqueness conditions for the tensor decomposition are formulated. In addition, we provide an algorithm utilizing alternating least square based approaches for finding the unique decomposition. The chapter investigates the importance of dFC for biological gender classification from fMRI. It is shown that gender can be predicted accurately from most of the task-related connectivity patterns in brain. The chapter successfully demonstrates the importance of dFC for prediction of intelligence metrics from fMRI. We find that subject-wise weights of *dynamic* spatio-temporal maps are predictive of intelligence. The chapter proposes a novel method to extract related *dynamic* sub-networks associated with gender and intelligence prediction. Statistical tests are also carried out to validate the significance of the proposed sub-networks.

1.3.5 Contribution of Chapter 6

This chapter investigates the efficacy for a number of rs-fMRI based *static* features, *e.g.*, absolute correlation coefficient values and network metrics for classifying adolescent MDD *vs.* healthy controls. *Bivariate* and *multivariate* features are used for feature selection and classification. The chapter formulates the use of *differential sub-graph entropy* to extract a *sub-network* of important regions and edges that can be input to a classifier to achieve a very high accuracy, sensitivity and specificity for classifying MDD *vs.* healthy controls among adolescents. The predictive accuracy is *statistically significant*. The proposed approach also outperforms previous network based measures [26] for this prediction task. This chapter ranks brain regions and edges in order of priority that have higher differential *sub-graph* entropy between MDD *vs.* healthy. Empirical results show that the regions and edges identified by the proposed method have biological significance. The chapter demonstrates the utility of *dynamic* connectivity profiles for identifying adolescent MDD. *Dynamic* components extracted using constrained-PARAFAC and ICA achieve high sensitivity but poor specificity for classification of MDD. Finally, we propose a joint *static* and *dynamic* feature concatenation process to classify MDD from rs-fMRI accurately.

Chapter 2

Ranking Regions, Edges and Classifying Tasks in Functional Brain Graphs by Sub-Graph Entropy

2.1 Introduction

The *state* of the human brain network changes dynamically from task to task or from resting-state to a task, where each state represents a specific pattern in brain connectivity. Finding patterns in those connectivity *states* are of utmost *importance* [5, 6]. Recently there has been a surge of interest in understanding brain connectivity patterns while a person performs a task through the use of network theory [22, 27, 28]. Although complex network measures have been applied previously to analyze brain networks, several areas within this particular sub-field remain unexplored. This chapter introduces the notions of graph entropy and *sub-graph* entropy and applications of these metrics to functional brain network analysis and classification. We propose the use of *sub-graph* entropy as an information-theoretic measure to compute complexity of brain networks. Special cases of *sub-graph* entropy include node entropy and edge entropy. It may be noted that, to the authors' best knowledge, this is the first attempt to make

use of *sub-graph* entropy to analyze brain networks. We also propose ranking of regions and edges of functional brain networks using these metrics. Node entropy and edge entropy are used as features for classifying *functional connectivity* patterns from task-fMRI (t-fMRI) corresponding to a number of unique *states*. The t-fMRI data is taken from emotion and gambling tasks from Human Connectome Project (HCP) dataset [29]. Although, emotion and gambling tasks are used in this chapter for illustration, the proposed information-theoretic metric is generalizable to other tasks and potentially to two different groups, *e.g.*, patients *vs.* controls, male *vs.* female etc.

There are multiple ways to define brain connectivity. *Structural connectivity* refers to a range of physical links that connect neuronal units. *Functional connectivity* captures patterns of deviations from statistical independence between distributed and possibly distant neuronal units [8, 9]. Joint connectivity captures links that connect neuronal units both physically and functionally [10]. Among these, *functional connectivity* is highly time dependent, and it can be statistically nonstationary. It is modulated by external task demands and sensory stimulation, as well as the internal *state* of the organism. In this chapter, we use *functional connectivity* extracted from t-fMRI as representative of brain *states*. In this representation, each region is a collection of neural elements, defined based on anatomy of brain tissues [11]. The brain activities of each region are represented by different time-series corresponding to different voxels and their average value can represent the behavior of the region over time. The functional brain network (graph) is represented by nodes and edges, where each node is associated with the mean time-series of a brain region and each edge weight corresponds to the *absolute value* of the correlation coefficient of the two time-series of the two vertices of the edge. This view is popular in fMRI literature and finds evidence through the works of [5, 12].

Task-fMRI studies of human brain have previously focused on finding a representative network connectivity corresponding to a *state* [6]. The application of network theory for analyzing the *states* has revealed that individual human brain exhibits centrality property [22], i.e., some human brain regions have higher *importance* in the whole network than others in terms of connections to other nodes. The centrality properties of a network are utilized to infer information about the *state*. For example, if a node has high *centrality* value in a network, the corresponding *state* can be understood in terms

of behavior of the node. Although, these network metrics are well suited to extract regions based on a particular definition of *importance*, how these measures can be applied to classify two *states* from brain connectivity networks remains unclear. We believe that information-theoretic approaches can be useful to address this challenge. We introduce information-theoretic entropy measures for analyzing and classifying brain networks in this chapter.

During the emotion and gambling t-fMRI experiment, a subject performs the task in blocks. The time periods when a task is performed are interleaved by rest periods. Hence from each subject, two functional networks each corresponding to a particular *state* (*e.g.,* task *vs.* no-task for emotion and gambling) of brain are extracted. For simplicity, we assume that the brain *state* remains similar for the whole duration of task or no-task. Hence each functional network can be seen as representative of that particular *state*.

Task State Network. The network connectivity for a task is constructed, by taking the abosolute Pearson correlation coefficient between anatomical regions from fMRI time points, when a subject is performing a task (*e.g.*, emotion, gambling) during a t-fMRI experiment [30–33]. Note that each subject has one network corresponding to a task *state*. In this work, t-fMRI time-series have been extracted from 475 subjects for emotion and gambling task from the Human Connectome Project [34].

No-Task State Network. The network connectivity for a no-task is constructed from fMRI time points when a subject is *not* performing a task during a t-fMRI experiment. These time points contain baseline hemodynamic signals during transition periods [35]. Note that each subject has one network corresponding to no-task *state*.

2.1.1 Hypothesis and Contributions

The main objective of the study is to understand whether brain *states* can be predicted using network measures from t-fMRI. First, we hypothesize that there are *important* nodes and edges in *functional connectivity*, that have significantly different network centrality measures for two different brain *states*. Our second hypothesis is that incorporating the *important* nodes, edges, and the corresponding centrality metrics to a classification model will lead to better prediction accuracy. Additionally, we hypothesize

that the network metric, which is most predictive of two *states*, will also be group differentiating and biologically meaningful. How the hypotheses are analyzed is described next.

Analysis of Hypothesis 1: Importance of Nodes and Edges. Using the information-theoretic network measures, we provide a novel way to identify *important* regions and edges from a network. Here, *important* regions (respectively, edges) are defined as the ones containing maximum entropy in *sub-graph*s. Also, how the regional *importance* changes between task *vs.* no-task or two different task conditions (emotion and gambling) is demonstrated. The *important* regions and edges extracted by this process are shown to be meaningful for classifying brain states.

Analysis of Hypothesis 2: Classifying Two Brain States. We use *sub-graph* entropy to characterize each of the *states* in a quantitative way. After the functional network is extracted, the entropies between two different groups of networks are compared. Binary classifiers are designed using the proposed and state-of-the-art network metrics to classify two *states*. The analysis pipeline for this is showed in Fig. 2.1. Classification accuracy and group statistical test (t-test and effect size) are computed for the entropy values to demonstrate that they are statistically different for different task conditions. The classification performance is also compared with previously known state-of-the-art network centrality metrics.

Contributions. Contributions of this chapter are three-fold. First, we propose the use of node and edge entropies as centrality metrics to compute the complexity of brain networks. Second, we propose ranking of nodes and edges of brain networks to extract *important* regions and edges between two *states*. We show that *sub-graph* entropy extracts some *important* regions, that the other network metrics can not identify. Third, using emotion and gambling t-fMRI data from the HCP dataset, we show that there is statistical difference of entropy measure between task *state vs.* no-task *state* and between two tasks. Node entropy and edge entropy are used as features to classify task *vs.* no-task or two different tasks with high accuracy. The proposed method outperforms other centrality measures for classifying two *states*. This validates the efficacy of *sub-graph* entropy as neural correlates of *states*.

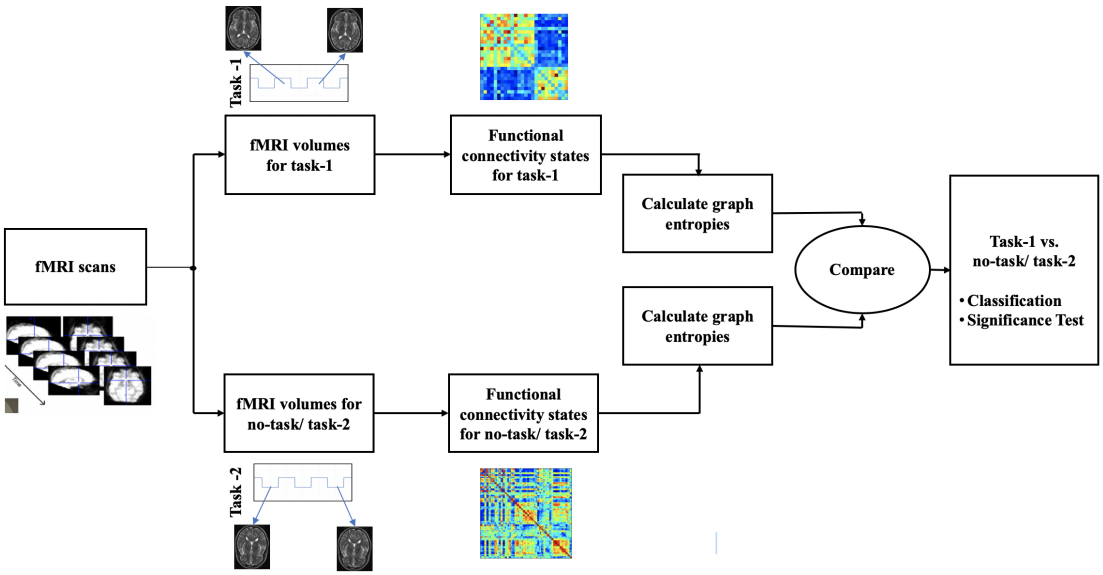

Figure 2.1: Pipeline for comparing group level entropy differences. After parcellating fMRI scans into regions, graph entropies are calculated for each subject's functional network. These entropies are then used to compare two different *states*.

2.1.2 Previous Work

Several metrics have been proposed in the neuroimaging literature [12, 36, 37] to compare different brain *states*. In this chapter, we represent each brain *state* as a network corresponding to different induced conditions as described before [13, 30–33, 38]. This section describes previous works on analysing brain network (corresponding to *states*) based on regional and edge *importance*.

Node importance. In a complex network, different nodes may have different usages. Some may be used more than others, whereas some nodes might be controlling the dynamics of the whole network. These measures describe the centrality properties of the graph [39]. Statistical significance tests are commonly used to infer about the most important regions and links associated with an external stimulation. Here we describe a statistical way to infer about important regions during task *states* using generalized linear models (GLM). Among the network-theoretic measures commonly used to infer about important nodes, we illustrate four centrality measures, namely, *degree* centrality, *eigenvector* centrality, *betweenness* centrality and *leverage* centrality. Generalized linear

models (GLM) [40] use multiple regression with false discovery rate controls to infer the most important regions during a task. *Degree* centrality [41] defines the central nodes to be the ones having the highest number of connections with other nodes. This centrality metric computes the *importance* of a node in the network by just the number of other nodes with which it directly interacts. *Eigenvector* centrality [42] takes into account the centrality of immediate neighbors when computing the centrality of a particular node. In particular, *eigenvector* centrality is a positive multiple of the sum of nearest node centralities. They are computationally very intensive compared to the other centrality metrics. *Betweenness* centrality [23] of a node represents the *importance* from the perspective of shortest paths in a graph. Particularly, this metric is calculated as the fraction of the shortest paths between all pairs of nodes (except the node in consideration) of a graph that contain the given node [43]. Joyece *et al.* [39] introduced a new measure of centrality called *leverage* centrality that finds out the influence of a node in a graph on other neighboring nodes based on their degree distribution. However, we note that the centrality measures may not only depend on degrees but also on the weight of the link between them. For example, if the weight of an edge is higher, it is more likely to be used. The information of the edge weights can be used to develop a new *importance* measure. In addition, all these centrality measures are only applicable when the topological structure of network is clearly known for every individual sample. In stochastic networks where the group behavior of a number of networks is of utmost *importance*, the extension of these measures is not straight-forward for differentiation between two groups. More details about these network measures can be found in [22].

Edge importance. There have been a few previous works for understanding the *importance* of edges in brain *states*. Among them, Network Based Statistics (NBS) [44] is a popular method for testing hypotheses about the edges in a network using t-test. It is used to identify connections and networks comprising the connectome associated with an experiment for a between-group difference.

Node and Edge Importance to Predict Brain States. This chapter introduces an information-theoretic approach to bridge the gap of understanding node and edge *importance* from brain networks (corresponding to *states*) to classify *states*. Here we note that information-theoretic centrality metrics have been proposed before, although in a different setting. Information-theoretic approaches have been used in communication

engineering since the seminal paper [45] of Shannon in 1949. The information-theoretic concepts have been applied to understand different types of complex systems, *e.g.*, in chemical graph theory [46, 47]. From a structural complexity viewpoint, graph entropy was first introduced by Trucco [48] and later formalized by Mowshowitz [49]. Structural graph entropy based on information-theoretic functional was introduced in [50]. The view of defining entropy based on intra-network communication between nodes was introduced in [51]. Mackenzie [51] showed that information-theoretic *importance* can be used as centrality in a communication network. Shetty *et al*. [52] defined an information-theoretic centrality measure [53] to find out leaders and followers from a communication pattern between employees of an organization. This formulation considered the communication pattern over a number of days between agents to infer their *importance*. An integrated approach for understanding node, edge *importance* and using them for prediction have never been accomplished before.

2.2 Results

This section proposes the information-theoretic metrics for analysing networks in order to extract important nodes and edges. It also demonstrates the classification results of applying node entropy and edge entropy to two different conditions on human brain networks.. First, graph entropy, *sub-graph* entropy, node entropy and edge entropy are illustrated using a simple example. Second, important regions and edges based on change in group (node and edge) entropy are ranked. Third, node and edge entropy values are used to design classifiers for classifying two connectivity *states* for emotion and gambling tasks. The classification performance is compared with the state-of-the-art network metrics for classification of *states*. The performance is also compared with a recently developed tensor based model for task prediction. Fourth, we compare *graph entropy* based centrality measure with commonly used centrality measures like *degree, betweenness, eigenvector and leverage*. A comparison of graph entropy based centrality with structural centrality is also shown in Subsection S.7 and Fig. A.13 in Appendix A. In addition, regions found through graph entropy are compared with the ones extracted by GLM and NBS. Lastly, the group-level differences of whole brain network between task *vs*. no-task (or task 1 *vs*. task 2) are investigated.

The brain region parcellation is based on [54]. In this thesis, for all subsequent brain networks, we use the regions of interest (85 in total) as defined in [54] viewed with BrainNet Viewer [55].

2.2.1 Illustration on Graph Entropy

For a graph $G = (V, E)$, let two nodes be v_i and v_j. The weight of the edge between two nodes v_i, v_j is denoted by e_{ij}. We illustrate the approach to calculate graph entropy using an example graph shown in Fig. 2.2.

The example graph depicted in Fig. 2.2(a) consists of 7-nodes and 10-edges. For simplicity assume that the edge weights are already normalized, i.e., they sum up to 1. In this scenario, we can calculate the graph entropy as follows.

- Identifying the normalized edges $q_{i,j}$. Let us identify adjacency matrix Q such as $Q(i, j) = q_{i,j}$

$$Q = \begin{bmatrix} 0 & 0.05 & 0 & 0 & 0.3 & 0 & 0 \\ 0.05 & 0 & 0.05 & 0 & 0 & 0.1 & 0 \\ 0 & 0.05 & 0 & 0.1 & 0 & 0 & 0 \\ 0 & 0 & 0.1 & 0 & 0.05 & 0 & 0.1 \\ 0.3 & 0 & 0 & 0.05 & 0 & 0.1 & 0.1 \\ 0 & 0.1 & 0 & 0 & 0.1 & 0 & 0.05 \\ 0 & 0 & 0 & 0.1 & 0.1 & 0.05 & 0 \end{bmatrix}$$

- Calculating the entropy as $H(G) = -\sum_{i,j} q_{i,j} \log_2(q_{i,j}) = -[4 \times 0.05 \times \log_2(0.05) + 5 \times 0.1 \times \log_2(0.1) + 0.3 \times \log_2(0.3)] = 3.0464$ bits.

In this example, a *sub-graph* is shown in Fig. 2.2(b). The normalized incidence matrix of this *sub-graph* is given by

$$Q'_s = \begin{bmatrix} 0 & 0.09 & 0 & 0 & 0.55 \\ 0.09 & 0 & 0.09 & 0 & 0 \\ 0 & 0.09 & 0 & 0.18 & 0 \\ 0 & 0 & 0.18 & 0 & 0.09 \\ 0.55 & 0 & 0 & 0.09 & 0 \end{bmatrix}$$

The entropy can be calculated as $H(G_s) = -\sum_{k,m} q'_{k,m} \log_2(q'_{k,m}) = -[2 \times 0.09 \times \log_2(0.09) + 2 \times 0.18 \times \log_2(0.18) + 0.55 \times \log_2(0.55)] = 1.8576$ bits. Note that, this *sub-graph* entropy is less than actual graph entropy, indicating that it contains less randomness compared to the previous graph.

Importance of a graph node can be thought to be dependent on the entropy of *sub-graph*s in its immediate neighborhood. In order to calculate the entropy of *sub-graph*s surrounding a node, we need to extract the structure of *sub-graph*s containing that node. After that, based on *sub-graph* complexity, we can calculate the *sub-graph* entropy. In this example, *sub-graph*s containing nodes 2 and 4, respectively, are shown in Fig. 2.2(c). The normalized incidence matrix of the *sub-graph* related to node 2 is given by

$$Q'_{v_2} = \begin{bmatrix} 0 & 0.25 & 0 & 0 \\ 0.25 & 0 & 0.25 & 0.5 \\ 0 & 0.25 & 0 & 0 \\ 0 & 0.5 & 0 & 0 \end{bmatrix}$$

The entropy of node 2 is given by $= -[0.5 \times \log_2(0.5) + 0.25 \times \log_2(0.25) + 0.25 \times \log_2(0.25)] = 1.500$ bits.

On the other hand, The normalized incidence matrix of the *sub-graph* related to node 4 is given by

$$Q'_{v_4} = \begin{bmatrix} 0 & 0.4 & 0 & 0 \\ 0.4 & 0 & 0.2 & 0.4 \\ 0 & 0.2 & 0 & 0 \\ 0 & 0.4 & 0 & 0 \end{bmatrix}$$

The entropy of node is 4 given by $= -[0.4 \times \log_2(0.4) + 0.4 \times \log_2(0.4) + 0.2 \times \log_2(0.2)] = 1.5230$ bits. Note that, although the degree of node 2 and 4 are the same, their entropy values are different. The node entropy proposed in this work is different from vertex *strength* [56] where the *strength* of vertex is calculated as sum of edge weights associated with the vertex.

In this example, a *sub-graph* containing edge $1 - 2$ is shown in Fig. 2.2(d).

The normalized incidence matrix of this *sub-graph* is given by

$$Q'_{e_{12}} = \begin{bmatrix} 0 & 0.1 & 0 & 0.6 & 0 \\ 0.1 & 0 & 0.1 & 0 & 0.2 \\ 0 & 0.1 & 0 & 0.0 & 0 \\ 0.6 & 0 & 0 & 0 & 0 \\ 0 & 0.2 & 0 & 0 & 0 \end{bmatrix}$$

The entropy can be calculated as $= -[0.6 \times \log_2(0.6) + 0.2 \times \log_2(0.2) + 0.1 \times \log_2(0.1) + 0.1 \times \log_2(0.1)] = 1.5710$ bits. This entropy is more than the node entropy calculated before, implying the edge contains more information.

Average Entropy from a Group of Graphs. In order to infer entropy information from a group of graphs, their sample average can be calculated. In this case, entropy values for each node and edge for each graph are calculated and the average value across all graphs is computed. This average entropy acts as an unbiased estimator for the group. For proof, see Subsection S.10 in the Appendix A.

2.2.2 Importance of Nodes and Edges

Ranking of Regions. The *importance* of nodes can be described by the complexity it contains. If the *sub-graph* entropy is able to explain most complexity of the network, then those *sub-graph*s are more important. In other words, if node entropy is higher, then that node is more important in the whole network. Hence, we rank the regions based on node entropy $H(G_{v_i})$. From a group of graphs, node entropy is calculated for each node for every graph in the group. Then we calculate the average of each node entropy for the whole group and rank the vertices based on the group averaged node entropy. The algorithm to rank the regions based on node entropy is given in Algorithm 1. The ranking pipeline is also illustrated in Fig. A.1 in Appendix A.

This scheme can be seen as maximizing mutual information between *sub-graph* and the whole graph. We provide a proof in the Appendix A Subsection S.11.

We use the node entropy to rank the regions of brain which are most *important* for different conditions (emotion task, gambling task, no-task) using Algorithm 1. The result of the ranking process for emotion task is shown in Table 2.1 and Fig. A.2 in Appendix A. The regions of *importance* were consistent almost for every *state*, i.e., the regions that carried the most entropy did not change between task *vs*. no-task *states*.

Algorithm 1: Ranking of Regions

Data: Adjacency matrices from a group of fMRI-data

Result: Ranking of Regions Based on Node Entropy

```
EntropyRegion = |V| × 1 Vector;
RegionRank = |V| × 1 Vector;
MeanEntropy = |V| × 1 Vector;
for each subject k do
    for v_i ∈ V do
        EntropyRegion(k,v_i) = H(G_{v_i});
    end
end
MeanEntropy = mean(EntropyRegion) over all subjects;
RegionRank = sort(MeanEntropy)
```

Ranking of Edges. In this experiment, the edges are ranked based on edge entropy $H(G_{e_{ij}})$. As before, the edge entropy of each edge for every graph is calculated from a group of graphs. Then we compute the average of each edge entropy for the whole group and rank the nodes based on the group averaged edge entropy. The algorithm to

rank the edges based on edge entropy is given in Algorithm 2.

Algorithm 2: Ranking of Edges

Data: Adjacency matrices from a Group of fMRI-data

Result: Ranking of Edges Based on Edge Entropy

```
EntropyEdge = |E| × 1 Vector;
Edgerank = |E| × 1 Vector;
MeanEntropy = |E| × 1 Vector;
for each subject k do
    for e_ij ∈ E do
        EntropyEdge(k,e_ij) = H(G_{e_ij});
    end
end
MeanEntropy = mean(EntropyEdge) over all subjects;
EdgeRank = sort(MeanEntropy)
```

Edge entropy is then used to rank the functional edges of brain according to the *importance* of priority for different conditions (emotion task, gambling task, no-task) using Algorithm 2. The result of this ranking process for emotion task is shown in Table 2.1. The top-100 active edges are shown in Fig. A.3 in Appendix A. The *importance* of priority edges was consistent for every *state*. In all the *states*, the most *important* edges are those criss-crossing two hemispheres. Also, the edges are mostly concentrated in the frontal regions of the brain. This is also consistent with the nodes found in regional ranking for each separate condition.

Ranking based on Differential Entropy. Between two groups of tasks (or task *vs.* no-task conditions), if the communication pattern among brain regions change, then the change in pattern can be captured using the above mentioned ranking procedure. In this scenario, the regions or links with the most change in entropies between two groups play a significant role in discriminating the two classes. Suppose, for region v_i, the conditional entropy for subjects belonging to group $G1$ (where $G1 \in$\{Emotion, Gambling\}) is given by $H_{G1}(v_i)$ and for group $G2$ (where $G2 \in$\{No-task, Other Task\}), $H_{G2}(v_i)$. The difference between these two values would encompass the change in graph entropies between two groups of subjects for region i. We calculate the change in entropy (defined differential entropy) as $|H_{G1}(v_i) - H_{G2}(v_i)|$ where $|x|$ is the absolute value of x.

Then we rank them based on decreasing value. The results from our experiment show empirically that this ranking can capture the significant distinguishing regions between two groups. The same argument and ranking procedure can be applied to edges as well. The algorithm is described in Algorithm 3.

Algorithm 3: Ranking of Regions and Edges for Two Groups based on Differential Entropy

Data: Adjacency matrices from two groups of fMRI-data

Result: Ranking of Regions and Edges Based on Differential Entropy

dEntropyRegion = $|V|$ Vector;
dRegionRank = $|V|$ Vector;
dEntropyEdge = $|E|$ Vector;
dEdgeRank = $|E|$ Vector;
for $v_i \in V$ **do**
    Estimate group $H_{G1}(G_{v_i})$ using Algorithm 1;
    Estimate group $H_{G2}(G_{v_i})$ using Algorithm 1;
    dEntropyRegion$(v_i) = |H_{G1}(G_{v_i}) - H_{G2}(G_{v_i})|$;
end
for $e_{ij} \in E$ **do**
    Estimate group $H_{G1}(G_{e_{ij}})$ using Algorithm 2;
    Estimate group $H_{G2}(G_{e_{ij}})$ using Algorithm 2;
    dEntropyEdge$(e_{ij}) = |H_{G1}(G_{e_{ij}}) - H_{G2}(G_{e_{ij}})|$;
end
dRegionrank = sort(dEntropyRegion) ;
dEdgerank = sort(dEntropyEdge) ;

There are regions that have maximum change of entropy between two *states*. Although, these regions may not be among the most complex regions, they provide the maximum change of entropy between two *states*. We extract the regions that are *important* from the perspective of change of information in Table 2.2 for different tasks. The corresponding regions of interest for emotion *vs.* no-task are shown in Fig. 2.3. In addition, the regions of interest for gambling *vs.* no-task and emotion *vs.* gambling are shown in Figs. A.4 and A.5, respectively (Appendix A).

The change in ranking for emotion *vs.* no-task was the highest for fusiform cortex in the right hemisphere. For emotion *vs.* gambling task, the regions with maximum change in ranking for individual tasks are: left hemisphere banks of the superior temporal sulcus, left caudal anterior cingulate and right fusiform cortex. In order to facilitate the visualization of edge ranking procedure, the top ranked edges are overlaid on a brain template. Following group ranking procedure based on edge entropy, this process extracts top edges from (a) emotion *vs.* no-task (Fig. 2.4), (b) gambling *vs.* no-task (Fig. A.6 in Appendix A) (c) emotion *vs.* gambling (Fig. A.7 in Appendix A). These edges are also listed in Appendix A Tables A.1 and A.2. Here the top 100 edges for each group are identified. A close inspection of the results reveals several observations. First, group ranking procedure reveals edges that are distributed throughout the whole brain and some of them criss-cross the hemispheres. Second, differential entropy elevates the edges that belong to frontal-parietal and frontal-subcortical areas, *e.g.*, frontal lobe, parietal lobe, temporal lobe, cingulate gyrus, limbic system, striatum, thalamus, stem, and amygdala.

2.2.3 Performance of Classifying Two Brain States

The leave-one-out classification performance using top-25 region and significant edge entropies are shown in Table 2.3. The classification performance is compared with state-of-the-art network metrics for nodes. In addition, the classification performance for edges is also compared to NBS measures. A number of classifiers were tested, *e.g.*, support vector machine (SVM), random forest, naive Bayes, and logistic regression. All the classifiers perform similarly with respect to the features. Therefore, the results from support vector machine with radial basis function are presented for illustration. The hyperparameters for the classifiers were tuned using in-fold validation. The support vector machine classifier with a radial basis function kernel and node entropy features performs better for classifying two *states* with highest accuracy, specificity and sensitivity between node and edge based features separately.

Intersection and Union Sub-Graphs: Two *sub-graphs* are created from the intersection and union of top regions and edges to compute *sub-graph* entropies for different groups. The *intersection sub-graph* contains subset of edges associated with the nodes of the top-25 regions. The *union sub-graph* contains top-25 regions and significant edges.

The node and edge entropies associated with *union* and *intersection sub-graphs* are also used for classification. These results are summarized in Table 2.3.

When we utilize the regional centrality measures based on the regions of Table 2.2 to classify task *vs.* no-task *states* or emotion *vs.* gambling *states*, the classifier achieves very good area under the curve (AUC) values (shown in Fig. A.8 in Appendix A). Compared to other centrality measurements, the proposed centrality achieves better prediction consistently for the whole range of receiver operating characteristics (ROC). Using edge entropies, the proposed classifier achieves very good mean AUC values as shown in Fig. A.9 in Appendix A.

2.2.4 Statistical Analysis of Results

Significance of Regions and Edges. The statistical significance of the top ranked regions that have highest change in node entropy is investigated using *nonparametric permutation t-test* separately on each highly ranked regions. For emotion *vs.* no-task, out of the 25 regions shown in Table 2.2, top 11 have significant change in node entropy. For gambling *vs.* no-task, top 15 regions have significant change in node entropy. The same procedure, using t-test, is also carried out using other four centrality measures, i.e., *degree, betweenness, eigenvector* and *leverage* centrality. The significant regions found using the other centrality measures are shown in Tables A.3 and A.4 in Appendix A. Node entropy measure is always able to extract the regions found to be significant by other measures. In addition, it finds some other *important* regions not found by the state-of-the-art centrality measures. For emotion task, the regions shown to be significant by node entropy, but not by other measures, include: left hippocampus, left amygdala, left accumbens, right caudate, right pallidum and right transversetemporal. Similarly, for gambling task, the regions shown to be significant by node entropy, but not by other measures, include: left pericalcarine, right pericalcarine, right postcentral and right transversetemporal.

For edges, *nonparametric permutation t-test* is carried out using edge entropy values on all edges, and the statistically significant edges are found using $p = 0.05$ with Bonferroni correction. The sub-network containing the significant edges are all top ranked edges from Algorithm 3. The number of edges, that had significant change in edge entropy values correspond to 102, 118 and 83, respectively, for emotion *vs.* no-task,

gambling *vs.* no-task and emotion *vs.* gambling. The sub-networks containing the edges are shown in Fig. 2.4 for emotion *vs.* no-task.

Stability of Top Regions and Edges. We use a rigorous leave-one-out technique to rank regions and edges in order to understand the stability of our method [58–61]. We run the proposed algorithm (Algorithm 3) 475 times, each time leaving one subject out and ranking the regions and edges based on Algorithm 3. We find that, the top regions and edges obtained from this leave-one-out method are very stable as shown by their histograms. For emotion task, top 21 regions (from Table 2.2) were ranked among top 25 regions 475 times, the rest four regions came up 474, 470, 447 and 412 times, respectively. For gambling task, top 20 regions (from Table 2.2) came up 475 time, the rest five regions were ranked *important* 474, 470, 465, 445 and 438 times, respectively. For differentiating emotion *vs.* gambling, top 21 regions (from Table 2.2) were ranked higher 475 time, the rest five regions came up 470, 375, 360, 325 times, respectively. Out of the significant edges for three tasks, 75%, 85%, 80% edges, respectively, came up 475 times. The number of occurrences of the regions (and edges) among top-25 (and significant edges, respectively) are illustrated in Figs. A.10 and A.10 (Appendix A), respectively. The histogram for each case is quite flat signifying that important regions and edges were similar across most subjects. This indicates a consistent group-level behavior for classification, i.e., same features are being used for classifying two *states*.

Quantifying Classification Significance. To further establish that the results are better than chance, we perform permutation tests. Performing permutation test involves computing a trivial baseline using permuted labels, i.e., the accuracy produced if there was "no signal" between the features and label. Then we determined if our learned model performed significantly better than the baseline. Here, for each dataset (emotion *vs.* no-task, gambling *vs.* no-task, emotion *vs.* gambling), we performed 1000 iterations: each time, we randomly permuted the subject labels to effectively remove any relationship between the input features and the label, then we trained a model on the training subset of this set and tested it on the remaining subset. Fig. S12 shows the distributions of accuracy scores for the three datasets. In each case, we see that there is a significant difference between the centers of the distributions and the accuracy obtained by node entropy ($p = 4.8213 \times 10^{-8}, 7.7689 \times 10^{-11}, 9.8659 \times 10^{-10}$, respectively, for three tasks). The same conclusion holds for edge entropy. In addition to

the permutation tests, we use a binomial test to compare the leave-one-out classification accuracies (using node and edge entropy) to baseline accuracies, to determine if each learner is significantly better than previous state-of-the-art classifiers. Node entropy performs significantly better than the next best method (tensor based) for classifying emotion *vs.* no-task with $p = 7.9637 \times 10^{-7}$. In addition, it is significantly better than eigenvector centrality for classifying gambling *vs.* no-task ($p = 7.3483 \times 10^{-4}$). Edge entropy is also better than NBS based methods for classification with $p = 4.0653 \times 10^{-4}, 1.5673 \times 10^{-15}, 5.8537 \times 10^{-6}$, respectively, for three classification tasks. The highest classification performance is achieved using node and edge entropy features associated with the *union sub-graph*.

Comparison of Node Entropy based Importance with Other Measures. To understand the relationship between the proposed measure and other well-known centrality measures in fMRI literature, we use a scatter plot of the node entropy values for both task and no-task conditions with other centrality measures in Fig. 2.5 for emotion task. The gambling task follows similar pattern and has not been shown here. In addition, we calculate mean correlation values of centrality measures for a group of graphs (both simulated and real world) in Table 2.4. The simulated graphs are first constructed using 85 nodes and edges following a uniform distribution (0-1). Next, the graphs are made sparse similar to the sparsity of real networks. For each graph, node entropies are measured and correlated with other centrality measures. Then the average and standard deviation values of correlation are calculated. Correlation values are similarly calculated for the data from emotion and gambling tasks. The scatter plot and the table indicate that our proposed centrality measure has very low correlation values with *degree*, *betweenness* and *leverage* centrality although it has a somewhat high correlation with *eigenvector* centrality. This implies that graph entropy provides a different dimension of *importance* in comparison with *degree*, *betweenness* and *leverage*, and provides somewhat similar information with *eigenvector* centrality.

We also performed GLM analysis of the two tasks. Based on the value of regression coefficients, we ranked the regions associated with each task separately. The ranked regions are shown in Table 2.5.

Comparison of Graph Entropies between Two States. The total graph entropy values between *states* corresponding to two conditions (task *vs.* no-task time

points or task 1 *vs.* task 2) are also compared. After the calculation of two types of graph entropies for each subject, a one-sided t-test is carried out to understand if the two *states* were significantly different. Graph entropy based *p-values* for *functional connectivity states* are shown in Table 2.6. All the changes were statistically significant ($p < 0.05$). The corresponding group mean entropy values are also plotted and compared for two different *states* (task *vs.* no-task conditions or others) in Fig. A.14 in Appendix A. We use standard box plot to visualize the span of entropy values for each group. For classification between two *states*, this feature achieves greater than 0.7 area under curve (AUC) for classification for all cases. The *sub-graph* entropies between two *sub-graphs* are also compared across different tasks and illustrated as box-plots in Figs. A.15, A.16, respectively, in Appendix A.

2.3 Discussion

The important regions and edges extracted using only one condition are similar across all subjects. They are concentrated mainly in the frontal part of the brain. There are no significant differences between important regions and edges for different conditions. These regions and their connectivities are commonly used in brain to transfer information during task. Many of the significant regions are in anterior cingulate gyrus, ventromedial frontal cortex, and inferior parietal brain regions. These regions are consistent with the previous works by Cole *et al.* [62], Tomasi *et al.* [63], Zuo *et al.* [36]. We provide theoretical justifications in Appendix A Subsections S.10, S.11 and S.12 for using edge strength and average graph entropy as a measure of group-level behavior of *states* and show that maximizing *sub-graph* entropy leads to maximizing mutual information between a sub-structure and whole graph. Some of the regions extracted using one condition consist of some small and noisy regions like left temporal pole and right temporal pole. These regions are ranked lower when using differential entropy. Generally, smaller and noisier regions will not rank higher when differential entropy is used.

Emotion Task. Our definition of important regions between two different conditions based on change of information flow could also extract regions most responsible

for the tasks. We also identify a number of useful brain functional areas that are activated mainly during emotion tasks as significant regions between task *vs.* no-task networks. These areas are amygdala, caudate region, fusiform, striatum, and basal ganglia. Fusiform gyrus has been identified as one of the main regions for face information processing in Mccarthy *et al.* [64]. This region is also identified as one of the main regions for face emotion processing [65, 66]. We find this region among top-5 regions in our ranking. Pallidum, part of basal ganglia, is also a very important region in terms of emotion processing. Nucleus accumbens area (both right and left hemisphere) is also identified as a significant region. Neuclus accumbens has been shown to be an important area for emotional processing in [67–69]. Specially, Floresco *et al.* [69] hypothesize it to be an intermediary region regulating cognition and action. Areas from anterior cingulate cortex have been related to cognition and emotion [70]. Moreover, regions from anterior cingulate cortex (ACC) are related to intelligent behavior, i.e., emotional self-control, focused problem solving, error recognition, and adaptive response to changing conditions [71]. Also, Etkin *et al.* [72] showed its involvement in negative emotional stimuli [72]. We find hippocampal areas to have significant changes during emotion both for emotion *vs.* no-task and emotion *vs.* gambling. Hippocampus has been correlated with emotional responses and acts in conjunction with amygdala for processing of emotional situations. The amygdala and hippocampal areas, two medial temporal lobe structures, are linked to two independent memory systems, each with their unique characteristic functions, respectively. The situation where a person faces emotional stimuli, the two regions interact to give rise to specific responses. Specifically, amygdala can have effect on both the formation and storing of memories that depend on hippocampal activation [73]. The hippocampus area is associated with the amygdala response by forming episodic representations of the emotional stimuli. Although these regions are independent with respect to memory organization, they act in concert when emotion stimuli meets memory representations [73].

The emotion task based on visual face information has a great effect on the regions from visual cortex specifically V1 areas. Calcarine sulcus areas from both right and left hemispheres have the most change in information flow in case of regions and edges. Areas from parietal lobule are also identified as important regions to explain the functional network. These regions may have been prominent as they have been shown to be

responsible for processing higher order facial features [74]. One of the surprising finding is the ranking of caudate neucleus as an important region during the task. Caudate has generally been correlated with emotional processing but not with respect to the reaction to the preference of face pictures [75, 76]. It has also been identified as neural correlate for emotion based heart rate variability [77]. Hence, apart from main hub locations for angry or fearful emotions, brains of the subjects may also try to process multiple dimensions of the visual stimuli. The edges extracted as important edges also support the regional involvement as most of the regions in the edges are similar as in Table 2.2. All the regions and edges have $p\text{-}value < 0.05$ indicating that they are statistically significant as well.

Gambling Task. The regions that have significant change in information belong to the reward circuitry of brain. Specifically regions from orbitofrontal [78], limbic system (amygdala, hippocampal) and basal ganglia neucleus (pallidum and striatum area caudate) were seen to have most change in entropies between gambling *vs.* no-tasks. One other area that has been shown to be involved from the proposed ranking method is neucleus accumbens. Knutson *et al.* have showed that activation in nucleus accumbens is prominent in people performing a gambling task. However, it is conjectured that this activity is associated with anticipation of reward prediction. This further reinforces the efficacy of differential entropy for ranking process using gambling task without the monetary reward [79, 80]. Moreover, reward processing is also correlated with reward-related functional activation in the nucleus accumbens [81]. In case of reward prediction, a behavior employed by the gambling task, significant activity is seen in the lateral orbitofrontal cortex and the striatum [82]. Basal ganglia region striatum is seen to be related to differentiating rewards from non-rewards [83]. Human brain limbic system is associated with neural responses for reward prediction [84]. Especially the difference between the actual gain and expected gain are associated with a neural circuitry of the mesolimbic dopamine system [85]. Gambling task also invokes areas related to decision making, *e.g.*, amygdala. Previous studies have shown that amygdala damage can interfere with decision-making [86]. Amygdala is critical in the neural system and it triggers somatic *states* from primary inducers that brings back emotions for a secondary event. Functional disconnectivity of the amygdala regions have been shown to impair acquisition of gambling tasks in rats. It also alters their decision making behavior [87].

Anterior cingulate cortex's involvement in cognition and conflict monitoring is well documented. Specifically, findings have posed specific challenges, especially concerning the way it addresses the processing of errors [88]. Dorsal ACC in adults are also active making risky selections. Furthermore, reduced activity in these areas are correlated with greater risk-taking performance making risky economic choices [89]. Other studies also suggest anterior cingulate is significantly correlated with performance on the gambling task [90] and risk anticipation [91]. In addition, we also extract significant regions from frontal lobe and parietal lobe whose entropy have changed significantly during the gambling task. As before, the top ranked edges extracted as important edges also supported the regional involvement as most of the regions in the edges are similar as shown in Table 2.2. All the regions and edges had $p\text{-}value < 0.05$ indicating that they are statistically significant as well.

Graph entropy values can be used as a representative metric for neural *state*. On the other hand, *sub-graph* entropy metric can be used to extract useful regions and edges that have significant differences between two *states*. Some of the regions found by *sub-graph* entropy are similar to traditional GLM (Table 2.5). Incorporating biologically meaningful regions, edges extracted through the differential entropy based ranking procedure also outperforms other centrality measures for classifying two *states*. In addition, the centrality information conveyed by graph entropy is different compared to *degree, betweenness and leverage* centrality. The scatter plots between node entropy and other centralities (Fig. 2.5) are flat and wide implying very little overlap in the information content. Many regions extracted through *sub-graph* entropy are different which indicates that *sub-graph* entropy conveys different information regarding *functional connectivity* compared to traditional methods.

2.4 Methods

2.4.1 Dataset

Two different task-fMRI datasets collected from 475 subjects from the Human Connectome Project (HCP) Young Adult study [29, 34] were used in this research. The tasks chosen were emotion and gambling. These data are publicly available from the ConnectomeDB database `https://db.humanconnectome.org`. All data were acquired

on a customized Siemens 3T Connectome Skyra scanner with the following parameters: task-fMRI was obtained with 2mm isotropic voxels with TR=720ms, TE = 33.1ms. Here emotion processing task was carried out with two runs of 2:16min with 176 frames per each run. Gambling task was continued for 3:12 mins with 253 frames per run for two runs [92, 93].

2.4.2 Description of Task

Emotion. This task was adapted from the one developed by Hariri *et al.* [3]. Participants are presented with blocks of trials that either ask them to decide which of the two faces presented on the bottom of the screen match the face at the top of the screen, or which of two shapes presented at the bottom of the screen match the shape at the top of the screen. The faces have either an angry or fearful expression. The task format is illustrated in Fig. 2.6. Here 6 trials of the same task (face or shape) are repeated with the stimulus presented for 2000 ms and a 1000 ms inter-task interval (ITI). Each block is preceded by a 3000 ms task cue ("shape" or "face") so that each block is 21 seconds long including the cue. Each of the two runs includes 3 face blocks and 3 shape blocks with 8 seconds of fixation at the end of each run. The task is described based on *WU-Minn HCP 500 Subjects Data Release Manual* available from `https://www.humanconnectome.org/`.

Gambling. This task was adapted from the one developed by Delgado *et al.* [4]. Participants play a card guessing game where they are asked to guess the number on a mystery card (represented by a question mask "?") in order to win or lose money. Participants are told that potential card numbers range from 1-9 and to indicate if they think the mystery card number is more or less than 5 by pressing one of two buttons on the response box. Feedback is the number on the card (generated by the program as a function of whether the trial was a reward, loss or neutral trial) and either: 1) a green up arrow with "$1" for reward trials, 2) a red down arrow next to -$0.50 for loss trials; or 3) the number 5 and a gray double headed arrow for neutral trials. The "?" is presented for up to 1500 ms (if the participant responds before 1500 ms, a fixation cross is displayed for the remaining time), followed by feedback for 1000 ms. There is a 1000 ms inter-task interval with a "+" presented on the screen. The task is presented in blocks of 8 trials that are either mostly reward (6 reward trials pseudo randomly interleaved with either

1 neutral and 1 loss trial, 2 neutral trials, or 2 loss trials) or mostly loss (6 loss trials pseudo-randomly interleaved with either 1 neutral and 1 reward trial, 2 neutral trials, or 2 reward trials). In each of the two runs, there are 2 mostly reward and 2 mostly loss blocks, interleaved with 4 fixation blocks (15 seconds each). The task format is shown in Fig. 2.7. The task is described based on *WU-Minn HCP 500 Subjects Data Release Manual* available from `https://www.humanconnectome.org/`.

2.4.3 Prepossessing

The HCP task-fMRI data was first processed following the HCP "fMRIVolume" pipeline (v3.4) [94], which includes gradient unwrapping, motion/distortion correction, registration to structural scan, nonlinear registration into MNI152 space, and intensity normalization as reported in [10]. Subsequently, spatial smoothing and activation maps generation using the generalized linear model implemented in FSL's FILM (FMRIB's Improved Linear Model with autocorrelation) [15] were performed. Additional details about the HCP "fMRIVolume" pipeline can be found in Barch et al. [93]. Using Freesurfer cortical parcellation atlas [54], 85 regions of interest were identified as shown in Table A.5 in Appendix A. An illustration of this pipeline is shown in Fig. 2.8. Mean time-series value of voxels in every region for each subject were then extracted separately for task and no-task conditions. The task blocks (respectively no-task blocks) were concatenated for each subject and for each region corresponding to task (respectively no-task). Also, linear, square and cubic trends were removed from these time-series.

2.4.4 Modeling the Brain Graph from fMRI

After mean time-series are extracted from predefined anatomical regions [54] from fMRI, a matrix of $R \times T$ (note that $R = |V|$) is generated. Here R is the number of regions and T is the number of time points. A node in the brain graph corresponds to a region of interest and is associated with one mean time-series. Absolute value of Pearson *correlation coefficient* between two mean time-series represents the edge weight associated with two nodes. This makes sure that we only have positively correlated edges. Absolute value of Pearson *correlation coefficient*s are computed separately for task *states* and no-task *states* as defined before. Specifically, the network connectivity for a task is

constructed from fMRI time points when a subject is performing a task (*e.g.*, emotion, gambling) during a t-fMRI experiment [30–33]. The network connectivity for a no-task is constructed from fMRI time points when a subject is *not* performing a task during a t-fMRI experiment [35]. Hence we get two adjacency matrices for each subject. The mapping process is shown in Fig. 2.9. Each adjacency matrix is made sparse by keeping top correlating edges. The edges had the same sparsity for all subjects. This was done by choosing $S = \frac{\log_2(R)}{\log_2(k)} = 1.8$ where k is average degree in the graph [39].

2.4.5 Centrality Measures

Throughout our analysis, we assume that an un-directed brain network is given by $G = (V, E)$ where V contains vertices or nodes, E contains weighted edges. Number of nodes is given by $|V|$ which is equal to number of regions or neuronal units (R). Number of edges is given by $|E|$. In this section, first we define graph entropy based on the edge weights of graph.

Edge Weight of Graph. The edge weight e_{ij} between two nodes (v_i, v_j) is defined by the absolute value of Pearson *correlation coefficient* between their corresponding time-series. Thus the measure of edge weight e_{ij} is proportional to the magnitude of correlation between the two time-series (v_i, v_j) as defined by $\rho(i, j) = E[v_i v_j] - E[v_i]E[v_j]$, where $E[X]$ represents average value of random variable X. This implies that if e_{ij} is higher, the two nodes behave more similarly, i.e., their interaction is more. Hence, the probability of communication between v_i, v_j is proportional to e_{ij}. We used 4 types of centrality measures for comparison namely *degree, betweenness, eigenvector and leverage* [39].

Degree Centrality. Degree [41] of node i is determined by the number of neighbors connected to node i.

Eigenvector Centrality. Eigenvector centrality [42] e_i is calculated by Equation 2.1.

$$e_i = \frac{1}{\lambda} \sum_{j=1}^{R} a_{ij} e_j \tag{2.1}$$

Here $a_{i,j}$ is $(i, j)^{th}$ entry of adjacency matrix corresponding to the graph and λ is a constant.

Betweenness Centrality. Betweenness Centrality [42] of node i, b_i, is defined by the Equation 2.2.

$$b_i = \frac{1}{(N-1)(N-2)} \sum_x \sum_y \frac{g_{xiy}}{g_{xy}} \tag{2.2}$$

Here g_{xy} is the number of shortest paths between any two nodes x and y. Also g_{xiy} is the number of paths among those passing through node i.

Leverage Centrality. Leverage centrality l_i is a measure of the relationship between the *degree* of a given node (k_i) and the *degree* of each of its neighbors (k_j), averaged over all neighbors (N_i) as reported in [39], and is defined in Equation 2.3.

$$l_i = \frac{1}{k_i} \sum_{N_i} \frac{k_i - k_j}{k_i + k_j} \tag{2.3}$$

The following two metrics are used for statistical comparison with graph entropy metrics.

Generalized Linear Model. Generalized linear model [40] is multiple regression of event blocks onto fMRI time-series. If there are two conditions, *e.g.*, task and no-task, the regression coefficients are estimated for each condition on each time-series. Their differences describe the activation map for each region. The regression coefficients are computed based on ordinary least square technique [95].

Structural Centrality. Structural centrality [96] of a network is defined as

$$C(G) = \frac{4R(R-1)}{R^2-4} \sum_{i=1}^{R} q_{i,j} \sum_{j=1, i \neq j}^{R} [q_{i,j} - \frac{1}{R(R-1)}] \tag{2.4}$$

where R is the number of nodes. If $C(G)$ is high, then the network is more central, i.e., they are influenced by a few leading nodes. A comparison of structural centrality and node entropy is shown in Subsection S.6 in Appendix A.

2.4.6 Proposed Metric: Graph Entropy

Entropy of Graph. For graph $G = (V, E)$, let two nodes be v_i and v_j. The weight of the edge between two nodes v_i, v_j is denoted by e_{ij}. Here e_{ij} represents the absolute

value of the correlation coefficient of the two time-series associated with time-series of regions v_i and v_j and specifies the interaction between two nodes (v_i, v_j). Let

$$q_{i,j} = \begin{cases} \frac{e_{ij}}{\sum(e_{ij} \in E)} & \text{when } i \neq j, \\ 0 & \text{when } i = j, \end{cases} \tag{2.5}$$

where $q_{i,j}$ is probability of correlation between nodes (v_i, v_j). It is easy to see that $\sum_{i,j} q_{i,j} = 1$. Note that $q_{i,j}$'s can also be identified as entries in the normalized incidence matrix Q of graph G such that $Q(i, j) = q_{i,j}$.

This definition allows us to define the *graph entropy* as

$$H(G) = -\sum_{\substack{e_{ij} \in E \\ q_{i,j} \neq 0}} q_{i,j} \log_2(q_{i,j}). \tag{2.6}$$

$H(G)$ can be seen as total amount of uncertainty in the whole network and its unit is bits. This entropy measure was introduced in [51]. Graph entropy has an inverese relationship with respect to *structural centrality* [96] .

Some mathematical properties of graph entropy as in Eq. 4.3 that are of interest are listed below.

- If some $q_{i,j} = 1$, then $H(G) = 0$. In that case, region i always communicates with region j. No other regions communicate with each other. Here i, j are leader nodes in the network.

- $H(G)$ takes its maximum value when all $q_{i,j}$'s are equally distributed. Here all regions participate equally in the communication process and the system is a homogeneous system. Hence, $H(G) \approx \log_2 R(R-1)$. In this scenario, no node is leader.

- The more uniform the distribution of the values of $q_{i,j}$, for any given number of communication channels, the larger the value of $H(G)$. That is, $H(G)$ is larger for those cases where there is no communication dominance or ranking of the participants. Communication dominance reduces the graph entropy in G.

Entropy of Sub-graphs. *Sub-graphs* can denote any portion or sub-structure of the main graph. For a *sub-graph* $G_s = (V_s, E_s)$, the modified incidence matrix Q' can

be computed using Eq. 2.7.

$$q'_{k,m} = \begin{cases} \frac{e'_{km}}{\sum(e'_{km} \in E_s)} & \text{when } k \neq m, \\ 0 & \text{when } k = m. \end{cases} \tag{2.7}$$

The *sub-graph* entropy can be computed as follows,

$$H(G_s) = -\sum_{\substack{k,m \in V_s \\ q'_{k,m} \neq 0}} q'_{k,m} \log_2(q'_{k,m}) \tag{2.8}$$

This measure is comparable among different *sub-graph*s of the same graph as the edges are normalized before computation of entropy.

Node Entropy. Let v_i be a node in graph G. Also, let *sub-graph* G_{v_i} contain the node v_i and its immediate 1-hop neighbors. Specifically, G_{v_i} consists of node v_i and the neighboring nodes that can be reached from v_i through its edges by hopping only once. Now let the set of nodes in G_{v_i} be V_{v_i} and the edges be the 1-hop edges from v_i denoted by E_{v_i}. Then the entries in modified incidence matrix can be calculated as

$$q'_{k,m} = \begin{cases} \frac{e'_{k,m}}{\sum(e'_{k,m} \in E_{v_i})} & \text{when } k \neq m, \\ 0 & \text{when } k = m, \end{cases} \tag{2.9}$$

where $q'_{k,m}$ is the normalized correlation coefficient between nodes (v_k, v_m) within that *sub-graph*. We define node entropy as given by,

$$H(G_{v_i}) = -\sum_{\substack{k,m \in V_{v_i} \\ q'_{k,m} \neq 0}} q'_{k,m} \log_2(q'_{k,m}) \tag{2.10}$$

Edge Entropy. Let e_{ij} denote the edge between vertices (v_i, v_j). The *sub-graph* corresponding to this edge is defined by combining 1-hop *sub-graph*s of nodes v_i and v_j. Assuming, $G_{v_i} = (V_{v_i}, E_{v_i})$ and $G_{v_j} = (V_{v_j}, E_{v_j})$, the new *sub-graph* for e_{ij} is $G_{e_{ij}} = (V_{e_{ij}}, E_{e_{ij}})$ where $V_{e_{ij}} = (V_{v_i} \cup V_{v_j})$ and $E_{e_{ij}} = (E_{v_i} \cup E_{v_j})$. Then the entries in modified incidence matrix can be calculated as

$$q'_{k,m} = \begin{cases} \frac{e'_{k,m}}{\sum(e'_{k,m} \in E_{e_{ij}})} & \text{when } k \neq m, \\ 0 & \text{when } k = m, \end{cases} \tag{2.11}$$

where $q'_{k,m}$ is the normalized correlation coefficient between nodes (v_k, v_m) within that *sub-graph*. We define edge entropy as given by,

$$H(G_{e_{ij}}) = -\sum_{\substack{k,m \in V_{e_{ij}} \\ q'_{k,m} \neq 0}} q'_{k,m} \log_2(q'_{k,m}) \tag{2.12}$$

2.4.7 Statistical Analysis

The node entropy and edge entropy values are compared across different *states* for all subjects. Based on their differences in entropy, they are ranked in descending order. We also calculate their corresponding *p-values* using a permutation t-test. The regions with significant change in entropies ($p \leq 0.05$) are illustrated in a table. The edges with significant change in entropies ($p \leq 0.05$), are plotted as sub-network in a brain template. To understand if the chosen rankings were stable enough, a leave-one-out subject scheme was implemented to select top regions and edges. In particular, in each iteration one subject is left out and the regions, edges are ranked based on the other 474 subjects. The occurrence of the most important regions and edges were plotted in a histogram [58–60]. To quantify the significance of classification performance, permutation tests are performed. This involves computing a trivial baseline—the accuracy produced by permuting the labels and then determining if the learned model performed significantly better than that. Here, we perform 1000 iterations for each of the datset, then we train a model on the training data and test it on the remaining instances. The classification performance of the proposed model is also compared with baseline methods using binomial tests. This involves using the baseline accuracies as parameter of a binomial distribution and calculating the probability of achieving the accuracy achieved by the proposed models.

In addition, graph entropy values for regions were correlated with other four centrality measures. We create a scatter plot containing regional entropy values *vs.* each of *degree, betweenness, eigenvector, leverage*. The correlation values between node entropy and other centralities for each subject are calculated. The total graph entropy measures were used to differentiate between task *vs.* no-task condition. We use t-test and effect size to differentiate these two *states* at a group-level. Furthermore, node and edge entropy values are compared using our algorithm and top-25 values are used to

classify task *vs.* no-task *states* in fMRI scan in each case (region, edge).

2.4.8 Software

MATLAB is used for running experiments and generating the results. Custom MATLAB code is created for extracting graph entropy measures. We used the brain connectivity toolbox (BCT) [22] to calculate the centrality metrics. SVM classifiers are designed using LIBSVM toolbox [97].

2.5 Conclusion

The main contribution of the study is to demonstrate that well defined brain *states* can be predicted using *sub-graph* entropy from t-fMRI data. We showed that there are *important* nodes and edges in *functional connectivity* that are sufficiently distinguishing between two different brain *states*. The current work has introduced the notion of *sub-graph* entropy in general and node and edge entropies in particular to rank regions and edges in brain graphs in a quantitative manner. Results obtained by the proposed method have been compared with that from the generalized linear model (GLM), *degree* centrality, *eigenvector* centrality, *betweenness* centrality and *leverage* centrality and network based statistics (NBS). In this chapter, node and edge entropies have been defined based on 1-hop neighbors. Whether node and edge entropies defined using 2-hop neighbors provide more accurate prediction of brain network state needs further research. Future work will be directed towards applications of the technique in identifying *dynamic* states from fMRI tasks as well as from other temporally rich signals such as electroencephalogram (EEG) [98, 99] and magnetoencephalogram (MEG) [100, 101]. While node and edge entropies have been used in this chapter, identifying *sub-graphs* corresponding to certain tasks requires further research. Investigating applications of the technique to understand differences in brain networks of populations with various diseases and healthy control is also of interest. In many disease preditcion applications, filtered versions of time-series have been found to be more discriminative of the disease state [26, 59–61]. Thus, sub-graph entropy features should be extracted from filtered fMRI and then used for classification; this topic needs to be investigated further.

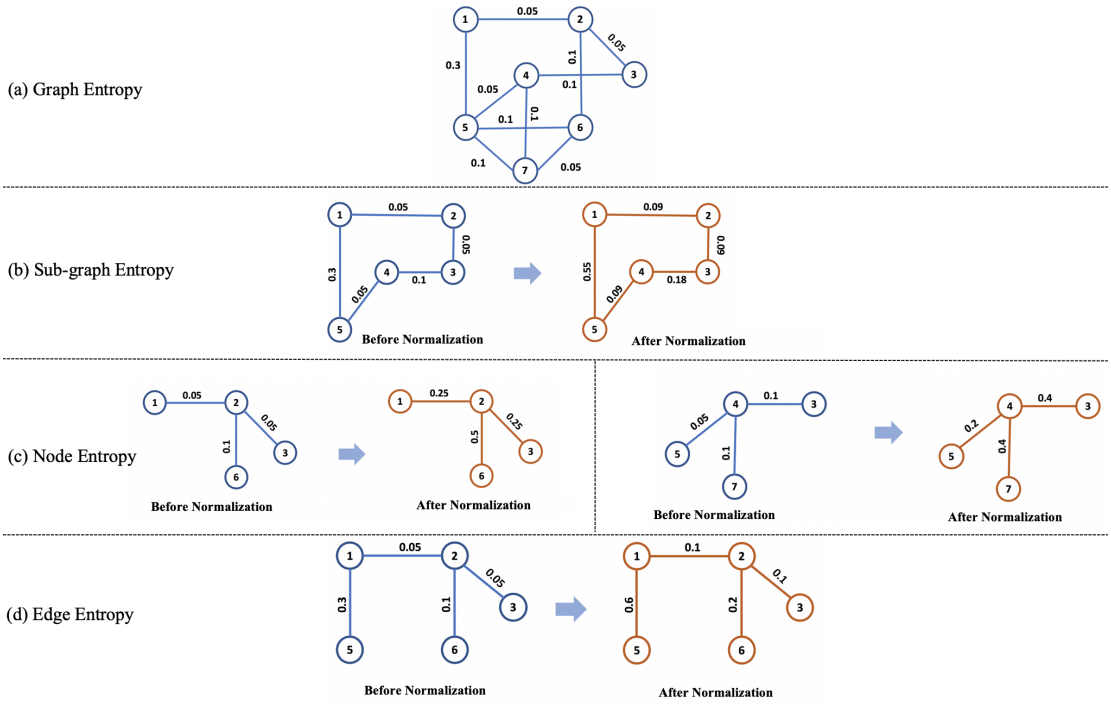

Figure 2.2: (a) An example of calculating graph entropy. This graph consists of 7-nodes. The weighted edges between them are normalized, i.e., they sum up to 1. (b) An example of *sub-graph* from the example in Fig. 2.2(a). To calculate the *sub-graph* entropy, we normalize the edge connection. *Left: sub-graph* before normalization. *Right: sub-graph* after normalization. This *sub-graph* consists of 5-nodes. As the weighted edge between them are normalized, they sum up to 1. (c) *Sub-graph* associated with node 2 (*left*) and node 4 (*right*) from the example in Fig. 2.2(a). To calculate the *sub-graph* entropy, we normalize the edge connection. These *sub-graphs* consist of 4-nodes. As the weighted edge between them are normalized, they sum up to 1. (d) An example of *sub-graph* containing edge $1-2$ from the example in Fig. 2.2(a). To calculate the *sub-graph* entropy, we normalize the edge weights. This *sub-graph* consists of 5-nodes. As the weighted edges between them are normalized, they sum up to 1.

Table 2.1: *Left*: Top regions employed for emotion task according to Algorithm 1. *Right*: To edges associated with the emotion task according to Algorithm 2.

Region	**Entropy**
Temporal Pole - R	5.9912
Temporal Pole - L	5.8128
Parstriangularis - L	5.6191
Insula - R	5.6073
Parstriangularis - L	5.5606
Entorhinal - R	5.3320
Insula - L	5.3212
Amygdala - R	5.2477
Parsopercularis - R	5.2355
Inferiortemporal - R	5.2300
Parsopercularis - L	5.0683
Inferiortemporal - L	5.0670
Putamen - R	5.0523
Parsorbitalis - R	5.0105
Superiortemporal - R	4.9332
Rostralmiddlefrontal - R	4.9240
Entorhinal - L	4.7726
Frontalpole -R	4.7241
Medialorbitofrontal - R	4.7214
Fusiform - R	4.7196
Rostralanteriorcingulate - R	4.7017
Fusiform - L	4.6306
Superiortemporal - L	4.5888
Caudalanteriorcingulate - L	4.4629
Bankssts - L	4.3983

Edge		**Entropy**
Parstriangularis - L	Temporalpole - R	6.7815
Insula - L	Temporalpole - R	6.7339
Temporalpole - L	Temporalpole - R	6.7341
Parstriangularis - L	Insula - R	6.6970
Temporalpole - L	Insula - R	6.6936
Parsopercularis - L	Temporalpole - R	6.6602
Temporalpole - L	Parstriangularis - R	6.6488
Inferiortemporal - L	Temporalpole - R	6.6433
Temporalpole - L	Parsopercularis - R	6.6427
Parstriangularis - L	Entorhinal - R	6.6381
Entorhinal - L	Temporalpole - R	6.6161
Putamen - R	Temporalpole - L	6.6110
Temporalpole - L	Entorhinal - R	6.6097
Superiortemporal - L	Temporalpole - R	6.6034
Insula - L	Parstriangularis - R	6.6027
Amygdala - R	Parstriangularis - L	6.6012
Fusiform - L	Temporalpole - R	6.5989
Temporalpole - L	Inferiortemporal - R	6.5952
Parstriangularis - L	Parstriangularis - R	6.5944
Temporalpole - L	Rostralmiddlefrontal - R	6.5925
Parstriangularis - L	Parsopercularis - R	6.5889
Parstriangularis - L	Inferiortemporal - R	6.5767
Temporalpole - L	Parsorbitalis - R	6.5754
Putamen - R	Parstriangularis - L	6.5752
Bankssts - L	Temporalpole - R	6.5649

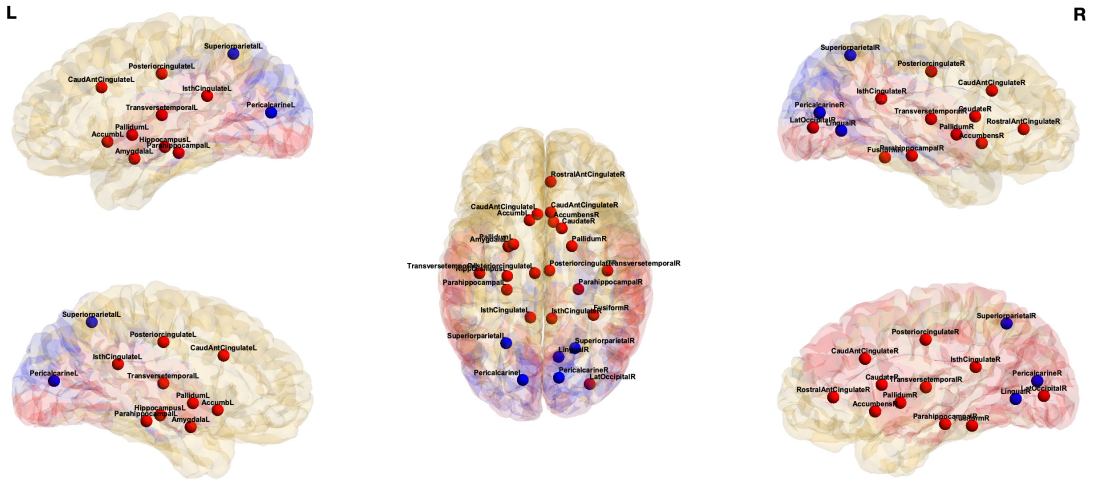

Figure 2.3: Visualization of *important* regions that have highest differential entropy between two *states* for emotion task *vs.* no-task. *Red:* regions that have higher node entropy during emotion task, *blue:* regions that have higher node entropy during no-task.

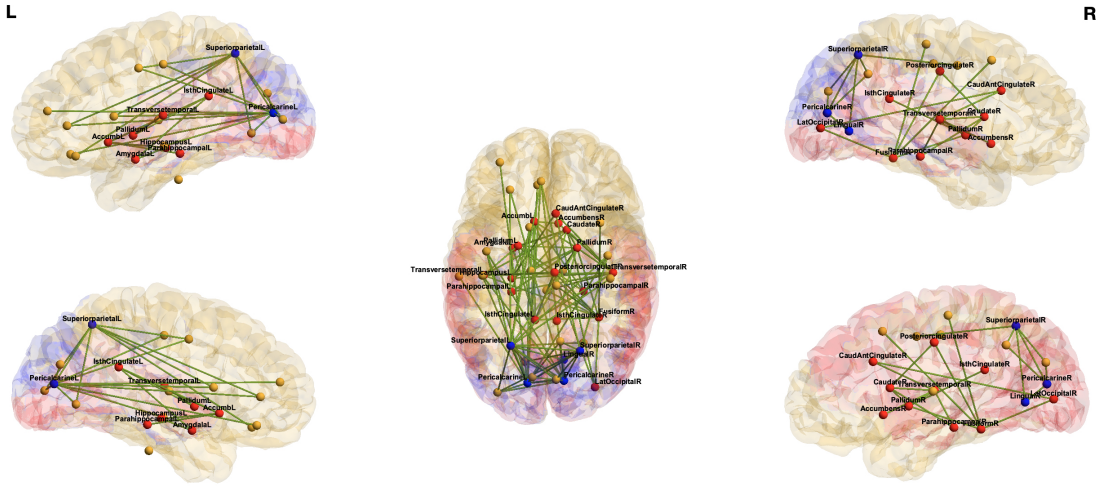

Figure 2.4: Visualization of *important* edges that have highest differential entropy between two *states* for emotion task *vs.* no-task. *Red:* regions that have higher node entropy during emotion task, *blue:* regions that have higher node entropy during no-task, *yellow:* regions that are not significant based on node entropy.

Table 2.2: Ranking of *important* regions that have differences in entropy between two tasks. The regions with significant change in entropy values are ranked among top 15 regions.

Emotion *vs.* No-task		**Gambling *vs.* No-task**		**Emotion *vs.* Gambling**	
Regions	**Diff. Entropy**	**Regions**	**Diff. Entropy**	**Regions**	**Diff. Entropy**
Pericalcarine - L	0.1347	Accumbens - L	0.1355	Hippocampus - L	0.5736
Superiorparietal - L	0.1343	Pallidum - L	0.1209	Cuneus - L	0.5039
Fusiform - R	0.1212	Caudate - R	0.118	Pericalcarine - L	0.4924
Pallidum - R	0.1068	Lingual - L	0.1138	Pallidum - R	0.4222
Superiorparietal - R	0.1055	Accumbens - R	0.1055	Precuneus - L	0.4031
Amygdala - L	0.1008	Precentral - R	0.1028	Fusiform - R	0.3810
Caudate - R	0.0992	Pericalcarine - L	0.1005	Parahippocampal - R	0.3675
Pericalcarine - R	0.0981	Postcentral - L	0.0993	Putamen - L	0.3640
Hippocampus - L	0.0969	Superiorfrontal - R	0.0985	Caudalanteriorcingulate - L	0.3519
Accumbens - L	0.0964	Transversetemporal - R	0.0976	Brain Stem	0.3468
Transversetemporal - R	0.0961	Amygdala - R	0.0967	Bankssts - L	0.3370
Caudalanteriorcingulate - R	0.0912	Posteriorcingulate - R	0.0965	Supramarginal - R	0.3362
Parahippocampal - L	0.0880	Postcentral - R	0.0878	Superiorparietal - R	0.3255
Rostralanteriorcingulate - R	0.0784	Pericalcarine - R	0.0872	Pericalcarine - R	0.3080
Isthmuscingulate - L	0.0767	Brain Stem	0.0863	Left Pallidum	0.3069
Parahippocampal - R	0.0762	Precentral - L	0.0788	Putamen - R	0.3049
Pallidum - L	0.0757	Parahippocampal - L	0.0771	Lateraloccipital - R	0.2851
Lateraloccipital - R	0.0714	Lateralorbitofrontal - L	0.0739	Accumbens - R	0.2810
Posteriorcingulate - R	0.0708	Inferiorparietal - L	0.0734	Hippocampus - R	0.2783
Transversetemporal - L	0.0648	Parsopercularis - L	0.0720	Transversetemporal - L	0.2604
Posteriorcingulate - L	0.0635	Cerebellum Cortex - R	0.0700	Transversetemporal - R	0.2584
Lingual - R	0.0566	Caudate - L	0.0696	Parsorbitalis - R	0.2538
Caudalanteriorcingulate - L	0.0550	Frontalpole - L	0.0684	Cerebellum Cortex - L	0.2373
Accumbens - R	0.0521	Lateralorbitofrontal - R	0.0667	Superiorfrontal - L	0.2303
Isthmuscingulate - R	0.0519	Amygdala - L	0.0658	Rostralmiddlefrontal - R	0.2224

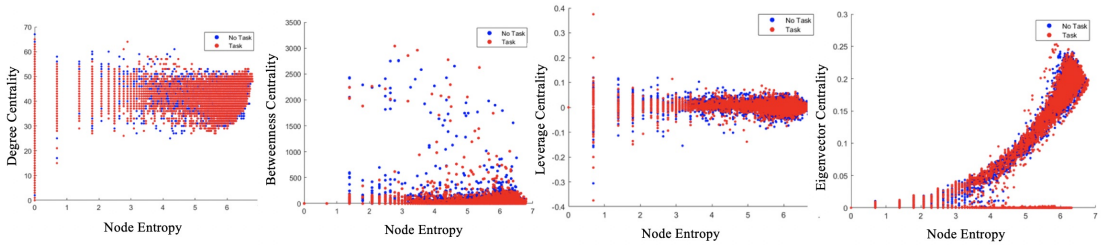

Figure 2.5: Comparing centrality measures for *emotion* task. *Left* to *right*: Information-theoretic centrality *vs.* *degree, betweenness, leverage, eigenvector* centrality. For each region the measures were plotted and overlaid for all subjects. Number of points for task and no-task are same.

Table 2.3: Classification performance for three classification tasks. Performance of node entropy is compared with other region based centrality measures. Performance of edge entropy is compared with NBS. In addition, classification performance for sub-graph containing intersection and union of top regions and edges are demonstrated. Sub-graph - 1 (intersection) contains top-25 regions and significant edges where nodes belong to top-25 regions. Sub-graph - 2 (union) contains top-25 regions and significant edges.

	Emotion *vs.* No-task				**Gambling *vs.* No-task**				**Emotion *vs.* Gambling**			
Region Performance	**# features**	**Accuracy**	**Specificity**	**Sensitivity**	**# features**	**Accuracy**	**Specificity**	**Sensitivity**	**# features**	**Accuracy**	**Specificity**	**Sensitivity**
Node Entropy (proposed)	25	**0.96**	**0.94**	**0.98**	25	**0.97**	**0.96**	**0.97**	25	**0.94**	**0.97**	0.91
Degree [41]	85	0.85	0.90	0.82	85	0.92	0.94	0.89	85	0.91	0.90	0.93
Eigenvector [42]	85	0.90	0.87	0.93	85	0.94	**0.96**	0.94	85	**0.94**	0.92	**0.95**
Betweenness [23]	85	0.82	0.87	0.80	85	0.89	0.91	0.89	85	0.86	0.88	0.84
Leverage [39]	85	0.83	0.85	0.81	85	0.87	0.83	0.91	85	0.83	0.87	0.80
Tensor based [57]	1280	0.91	0.93	0.89	1280	0.92	0.88	0.94	1280	0.90	0.85	**0.95**
Edge Performance	**# features**	**Accuracy**	**Specificity**	**Sensitivity**	**# features**	**Accuracy**	**Specificity**	**Sensitivity**	**# features**	**Accuracy**	**Specificity**	**Sensitivity**
Edge Entropy (proposed)	102	**0.91**	**0.94**	**0.87**	118	**0.96**	**0.96**	**0.95**	83	**0.94**	**0.94**	**0.95**
NBS [44]	536	0.86	0.81	0.90	1527	0.8	0.86	0.75	1496	0.88	0.92	0.85
Sub-graph Performance	**# features**	**Accuracy**	**Specificity**	**Sensitivity**	**# features**	**Accuracy**	**Specificity**	**Sensitivity**	**# features**	**Accuracy**	**Specificity**	**Sensitivity**
Sub-graph - 1 (Intersection)	77	0.95	0.94	0.96	89	0.94	0.96	0.93	42	0.91	0.93	0.90
Sub-graph - 2 (Union)	127	**0.97**	**0.95**	**0.98**	143	**0.97**	**0.96**	**0.97**	108	**0.95**	**0.97**	**0.94**

Table 2.4: Comparison of correlation values between graph entropy and other centralities.

	***Degree vs.* Node Entropy**	***Betweenness vs.* Node Entropy**	***Leverage vs.* Node Entropy**	***Eigenvector vs.* Node Entropy**
Simulated	0.3899 ± 0.0928	0.6865 ± 0.0451	0.36450 ± 0.0883	0.9412 ± 0.0120
Emotion	0.2478 ± 0.1867	0.2672 ± 0.0689	0.0343 ± 0.0430	0.5912 ± 0.0499
Gambling	0.2475 ± 0.1782	0.2666 ± 0.0686	0.0346 ± 0.0410	0.5876 ± 0.0487

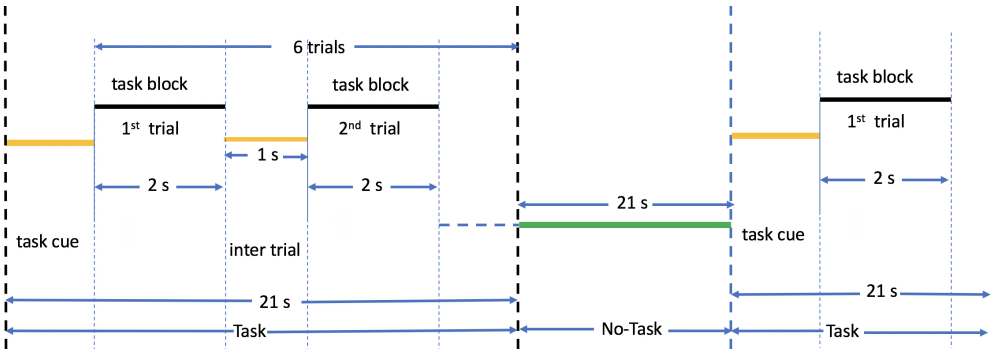

Figure 2.6: Emotion task pipeline. Each task block consists of 6 trials of emotion task paradigm following [3] of duration 21 s. This follows by a no-task block of 21 s. There are 3 task blocks and 3 no-task blocks in total.

Table 2.5: Regions with high regression coefficients from generalized linear model analysis. The regression coefficients are divided by the highest coefficient. Ranked regions from entropy models are also shown for comparison. The common regions are in bold.

Emotion *vs.* No-task				**Gambling *vs.* No-Task**			
Entropy Based		**GLM Based**		**Entropy Based**		**GLM Based**	
Regions	**Entropy**	**Regions**	**Reg. Coeff**	**Regions**	**Entropy**	**Regions**	**Reg. Coeff**
Pericalcarine - L	0.1347	**Lateraloccipital - R**	1	Accumbens - L	0.1355	Caudalanteriorcingulate - R	1
Superiorparietal - L	0.1343	Lateraloccipital - L	0.9727	Cuneus - L	0.1209	Caudalanteriorcingulate - L	0.9749
Fusiform - R	0.1212	**Fusiform - R**	0.9492	**Caudate - R**	0.1180	**Superiorfrontal - R**	0.9568
Pallidum - R	0.1068	Amygdala - R	0.8540	Lingual - L	0.1138	Superiorfrontal - L	0.9359
Superiorparietal - R	0.1055	Fusiform - L	0.8443	Accumbens - R	0.1055	Rostralanteriorcingulate - R	0.9172
Amygdala - L	0.1008	**Pericalcarine - R**	0.7019	Precentral - R	0.1028	**Caudate - L**	0.8908
Caudate - R	0.0992	**Amygdala - L**	0.6902	Pericalcarine - L	0.1005	Rostralmiddlefrontal - L	0.8893
Pericalcarine - R	0.0981	Lingual - L	0.6223	Postcentral - L	0.0993	Rostralanteriorcingulate - L	0.8832
Hippocampus - L	0.0969	**Caudalanteriorcingulate - L**	0.6091	**Superiorfrontal - R**	0.0985	Thalamus - L	0.8789
Accumbens - L	0.0964	Temporalpole - L	0.5611	Transversetemporal - R	0.0976	Insula - L	0.8769
Transversetemporal - R	0.0961	Lingual - R	0.5485	**Amygdala - R**	0.0967	**Amygdala - R**	0.8719
Caudalanteriorcingulate - R	0.0912	**Caudalanteriorcingulate - R**	0.5450	Posteriorcingulate - R	0.0965	Insula - R	0.8708
Parahippocampal - L	0.0880	Superiorparietal - L	0.5385	Postcentral - R	0.0878	Thalamus - R	0.8689
Rostralanteriorcingulate - R	0.0784	Bankssts - R	0.5156	Pericalcarine - R	0.0872	**Caudate - R**	0.8624
Isthmuscingulate - L	0.0767	Rostralanteriorcingulate - L	0.5080	**Brain Stem**	0.0863	Hippocampus - L	0.8502
Parahippocampal - R	0.0762	Pericalcarine - L	0.4778	Precentral - L	0.0788	Rostralmiddlefrontal - R	0.8496
Pallidum - L	0.0757	Entorhinal - L	0.4725	Parahippocampal - L	0.0771	Parsopercularis - R	0.8494
Lateraloccipital - R	0.0714	Supramarginal - R	0.4621	Lateralorbitofrontal - L	0.0739	**Parsopercularis - L**	0.8460
Posteriorcingulate - R	0.0708	Superiorparietal - R	0.4389	Inferiorparietal - L	0.0734	**Brain Stem**	0.8387
Transversetemporal - L	0.0648	Rostralanteriorcingulate - R	0.4320	**Parsopercularis - L**	0.0720	Parstriangularis - L	0.8360
Posteriorcingulate - L	0.0635	Supramarginal - L	0.4300	Cerebellum Cortex - R	0.0700	Parstriangularis - R	0.8341
Lingual - R	0.0566	**Posteriorcingulate - R**	0.4274	**Caudate - L**	0.0696	**Amygdala - L**	0.8316
Caudalanteriorcingulate - L	0.0550	Precentral - L	0.4140	Frontalpole - L	0.0684	Hippocampus - R	0.8278
Accumbens - R	0.0521	Postcentral - L	0.4131	Lateralorbitofrontal - R	0.0667	Caudalmiddlefrontal - L	0.8276
Isthmuscingulate - R	0.0519	Brain Stem	0.4047	**Amygdala - L**	0.0658	Caudalmiddlefrontal - L	0.8244

Table 2.6: Graph entropy difference between two conditions for brain network

	Emotion Task *vs.* No-task	**Gambling Task *vs.* No-task**	**Gambling Task *vs.* Emotion Task**
	***p-value* (Effect Size)**	***p-value* (Effect Size)**	***p-value* (Effect Size)**
Graph Entropy	2.1344e-31 (0.57)	1.8636e-21 (0.45)	1.0721e-09 (0.29)

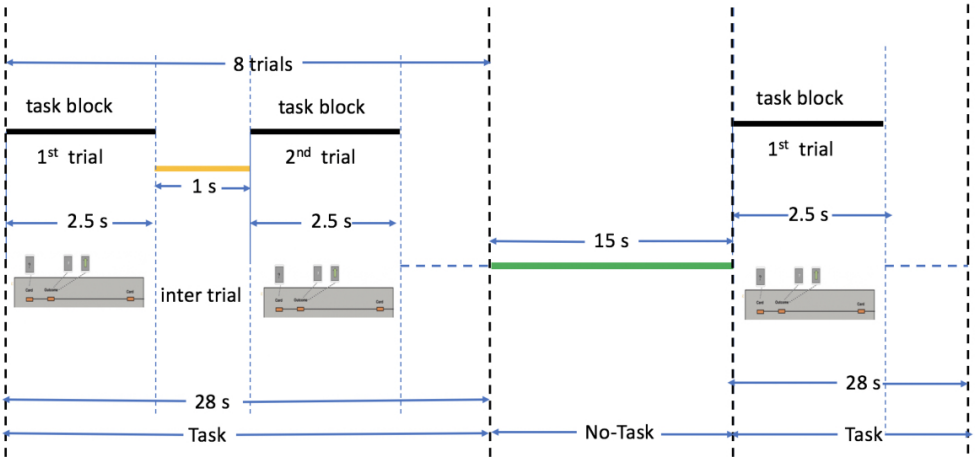

Figure 2.7: Gambling task pipeline. Each task block consists of 8 trials of gambling task paradigm following [4] of duration 28 s. This follows by a no-task block of 15 s. There are 4 task blocks and 4 no-task blocks in total.

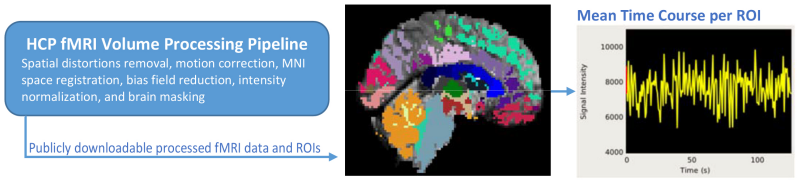

Figure 2.8: Preprocessing pipeline for extraction of fMRI time-series corresponding to anatomical regions.

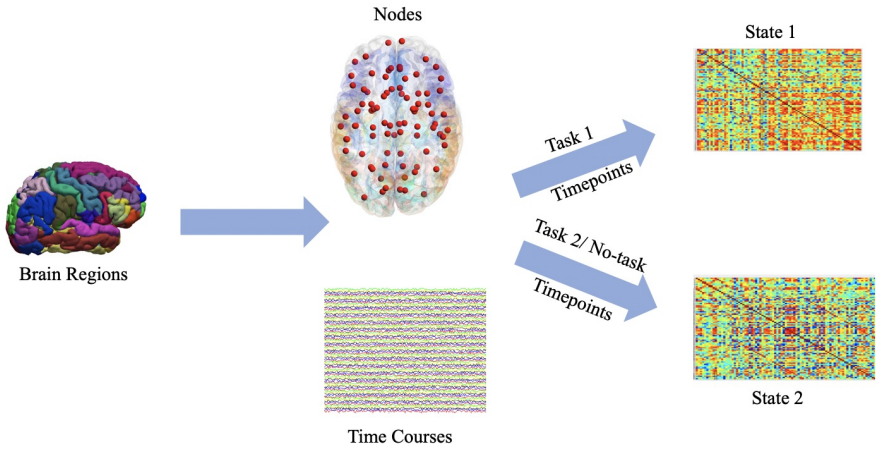

Figure 2.9: Pipeline for associating node and time-series to *states*.

Chapter 3

Graph-Theoretic Properties of *Sub-Graph* Entropy

3.1 Introduction

This chapter describes two important properties of *sub-graph* entropy, a centrality metric for bi-directional graphs, recently developed in [20]. *Sub-graph* entropy is used to rank important nodes in functional networks of brain. It can also be utilized as features for classification of brain states and diagnosis of psychiatric disorders [25]. Additionally, graph entropy has been used to understand the important event-based *dynamic* states of brain [102], and to diagnose epilepsy from electroencephalogram (EEG) [103]. Different operators have been used to represent bidirectional graphs, *e.g.*, [104, 105]. In this chapter, the shift operator for a graph is assumed to be the adjacency matrix [106]. We show that summation of *sub-graph* entropies is always lower bounded by the actual graph entropy. Additionally, we demonstrate that the summation of *sub-graph* entropies is also upper bounded by a constant. This constant depends on the properties of the graph such as the number of *sub-graphs* as well as the number of edges. Next, following the definition in [107], it is shown that node entropy (an instance of *sub-graph* entropy) is stable. Other sensitivity metrics have also been reported in literature, *e.g.,* [108]. We empirically show that node entropy is the most stable when compared with three other commonly used centrality measures: degree or strength [109], eigenvector [42], and betweenness [110]. Using synthetic dataset as well as real-world functional magnetic

resonance imaging (fMRI) data, we illustrate the applicability of these two properties in bi-directional graphs. Two types of fMRI data are used: resting state fMRI (rs-fMRI) [25] and task fMRI (t-fMRI) [20].

Although different measures of centrality may lead to different interpretations of node importance in a graph [39], it is imperative to understand the stability of these measures [111–114]. The comparison of stability properties of the aforementioned metrics were carried out in [107]. This chapter derives a new stability property for the node entropy measure in a bi-directional graph. Moreover, extensive experiments based on synthetic as well as real world data suggest that node entropy is the most stable over a range of nodes and varying noise [115] levels.

3.1.1 Contribution

The contributions of this chapter are as follows,

- This chapter derives the lower bound and upper bound for the summation of the *non-overlapping sub-graph* entropies from a bi-directional graph.
- The chapter demonstrates that node entropy is stable in the sense that the difference in centrality values for a given node in two different graphs is bounded by a constant times the distance between these graphs.
- Synthetic data and real world fMRI dataset are used to validate the results. It is shown that node entropy is more stable than strength, eigenvector and betweenness centrality.

3.2 Preliminaries

Definition 1. Sub-graph entropy [20]: *Sub-graphs* can denote any portion or sub-structure of the main graph. For a *sub-graph* $G_s = (V_s, E_s)$, of main graph $G = (V, E)$, the *sub-graph* entropy can be computed as:

$$H\left(G_s\right) = -\sum_{x,x' \in V_s} q(x,x') \log\left(q(x,x')\right)$$

where $q(x, x')$ denotes the normalized edge weight between nodes (x, x') for *sub-graph* G_s. For calculating the node entropy of node x, only the *sub-graph* containing the 1-hop neighborhood of node x is used. Here logarithm is computed with respect to base 2.

Graph entropy as a centrality measure has been demostrated in [51,52,96] and extended to *sub-graph* entropy in [20].

We also mention the definition of other types of centrality to be compared with node entropy later.

Strength centrality: Strength of node x is calculated as the summation of the edge weights connected to node x.

Eigenvector centrality: Eigenvector centrality e_x is determined by

$$e_x = \frac{1}{\lambda} \sum_{x'=1}^{N} w(x, x')$$

where $w(x, x')$ is $(x, x')^{th}$ entry of the adjacency matrix corresponding to the graph, λ is a constant, and N is number of nodes.

Betweenness centrality: For a node x, betweenness Centrality, b_x, is defined by

$$b_x = \frac{1}{(N-1)(N-2)} \sum_i \sum_j \frac{g_{ixj}}{g_{ij}}$$

Here g_{ij} is the number of shortest paths between any two nodes i and j. Also g_{ixj} is the number of paths among those passing through node x.

Definition 2. Stability [107]: Stability is defined as described in [107]. A centrality measure C is stable if, for every vertex set V, edge set E, adjacency matrix W, and any two graphs $G, H \in \mathcal{G}_{(V,E)}$, where $\mathcal{G}_{(V,E)}$ is a set of graphs sampled from the same distribution.

$$\left| C^G(x) - C^H(x) \right| \leq K_G d_{(V,E)}(G, H)$$

for every node $x \in V$, where K_G is a constant for every graph $G, C^G(x)$ is the centrality value of node x in graph G and similarly for H. Here $d_{(V,E)}(G, H) = \sum_{(x,x') \in E} |w(x, x') - w'(x, x')|$, where w's are entries in W.

3.3 Main Results

Theorem 1. If a graph $G = (V, E, W)$ is divided to K non-overlapping *sub-graphs* $G_1, G_2, \ldots, G_K$ then $H(G) \leq H(G) + \sum_k \log(\frac{1}{c_k}) \leq H(G_1) + H(G_2) + \ldots + H(G_K) \leq K \log \frac{|E|}{K}$, where c_k is the normalization constant for the k^{th} *sub-graph*, where $|E|$ is the number of edges in the graph.

Proof.

Part 1. Upper Bound.

$H(G)$ is computed as follows: $H(G) = -[w_1 \log(w_1) + w_2 \log(w_2) + ... + w_{|E|} \log(w_{|E|})]$ and $\sum_i w_i = 1, 0 < w_i < 1$. If G is divided into smaller graphs, then each smaller graph entropy involves normalization of weights. Let the normalized edge weights be denoted by w'_i.

Thus,

$$\begin{aligned}
&H(G_1) + H(G_2) + .. + H(G_K) = \\
&- [w'_1 \log(w'_1) + w'_2 \log(w'_2) + ... + w'_{|E|} \log(w'_{|E|})] \\
&\leq -(\sum_i w'_i) \log \frac{(\sum_i w'_i)}{|E|} (\text{ by log-sum inequality}) \\
&= -K \log \frac{K}{|E|} = K \log \frac{|E|}{K} \blacksquare
\end{aligned}$$

Part 2. Lower Bound.

$$\begin{aligned}
&H(G_1) + H(G_2) + .. + H(G_K) = \\
&- [w'_1 \log(w'_1) + w'_2 \log(w'_2) + ... + w'_{|E|} \log(w'_{|E|})] \\
&= H(G) - H(G) - [w'_1 \log(w'_1) + w'_2 \log(w'_2) + ... \\
&+ w'_{|E|} \log(w'_{|E|})] \\
&= H(G) + [(w_1 \log(w_1) - \frac{w_1}{c_1} \log(\frac{w_1}{c_1})) + \\
&(w_{|E|} \log(w_{|E|}) - \frac{w_{|E|}}{c_{|E|}} \log(\frac{w_{|E|}}{c_{|E|}}))] \text{ [} c_i \text{ normalization constant]} \\
&= H(G) + \sum_i [w_i \log(w_i)(1 - \frac{1}{c_i}) + \sum_i \frac{w_i}{c_i} \log(\frac{1}{c_i}) \\
&\geq H(G) + \sum_{k=1}^{K} \log(\frac{1}{c_k}) \text{ (Second term above is always } > 0) \\
&\geq H(G) \blacksquare
\end{aligned}$$

Corollary. If a graph G is divided into multiple non-overlapping *sub-graphs* the summation of the *sub-graph* entropy is always more than the original graph entropy.

Theorem 2. For a network with normalized edge weight $0 < \sigma \leq q(x, x') \leq 1$ for

each *sub-graph*, node *sub-graph* entropy is stable for $K_G = |\frac{\log \sigma}{c}|$, *i.e.*, for any node x,

$$\left|C^G(x) - C^H(x)\right| \leq |\frac{\log \sigma}{c}| d_{(V,E)}(G,H)$$

Here σ is the minimum value of normalized non-zero edge weights of all *sub-graphs* (we define $0 \log 0 = 0$), and c is the lowest normalization constant among all node *sub-graphs*.

Proof. Let us consider two arbitrary graphs $G = (V, E, W)$ and $H = (V, E, W')$. Let $w(x, x')$, $q(x, x')$ denote un-normalized weights of the graph and normalized weights in *sub-graphs*, respectively.

For *sub-graph* entropy,

$$\begin{aligned}
&\left|C^G(x) - C^H(x)\right| = |\sum_{x'|(x,x')\in E} q(x,x')\log(q(x,x')) \\
&- \sum_{x'|(x,x')\in E'} q'(x,x')\log(q'(x,x'))| \\
&= \left|\sum_{x'|(x,x')\in E} [q(x,x')\log(q(x,x')) - q'(x,x')\log(q'(x,x'))]\right| \\
&\leq \sum_{x'|(x,x')\in E} \left|q(x,x')\log(q(x,x')) - q'(x,x')\log(q'(x,x'))\right|
\end{aligned}$$

Following *Lemma 1* in Appendix, $|q(x,x')\log(q(x,x')) - q'(x,x')\log(q'(x,x'))|$ $\leq |\log\sigma|\,|q(x,x') - q'(x,x')|$. Thus using this result,

$$\begin{aligned}
&\left|C^G(x) - C^H(x)\right| \\
&\leq \sum_{x'|(x,x')\in E} \left|q(x,x')\log(q(x,x')) - q'(x,x')\log(q'(x,x'))\right| \\
&\leq \sum_{x'|(x,x')\in E} |\log\sigma|\,\left|q(x,x') - q'(x,x')\right| \\
&\leq \sum_{x'|(x,x')\in E} |\frac{\log\sigma}{c_x}|\,\left|w(x,x') - w'(x,x')\right| \ \ (\textit{Lemma 2} \text{ in Appendix.})
\end{aligned}$$

Here c_x is the normalization constant for *sub-graph* containing node x.

$$\leq \sum_{(x,x')\in E} |\frac{\log\sigma}{c}|\,\left|w(x,x') - w'(x,x')\right| = |\frac{\log\sigma}{c}| d_{(V,E)}(G,H) \blacksquare$$

Hence node entropy is stable.

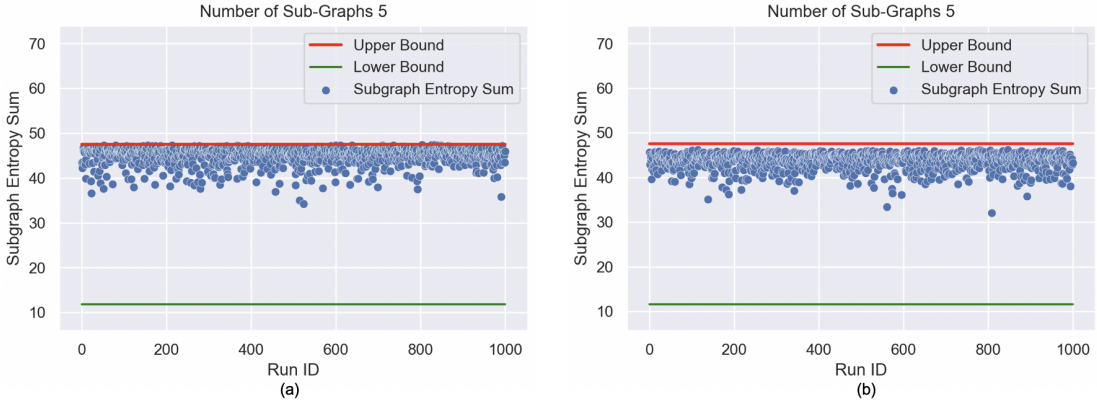

Figure 3.1: Upper bound and lower bound for a) Synthetic b) Real data. The division process was carried out 1000 times and the blue circles denote summation of *sub-graph* entropies for each run.

Experiments and Discussion

Graph Partitioning:

In order to understand the behavior regarding graph partitioning, a synthetic graph was created with edge weights uniformly distributed in the range $[0, 1]$. Next the graph was divided into non-overlapping graphs. Two types of division were considered, where number of *sub-graphs* were 5 and 50, respectively. Each of these divisions was carried out randomly 100 times and the summation of the *sub-graph* entropy values was calculated. The result of the simulation for the synthetic graph with 5 *sub-graphs* is shown in Fig. 3.1(a). The results for division with 50 *sub-graphs* is illustrated in Fig. 3.2.

The same process was repeated using real world data from rs-fMRI with regional percellations as mentioned in [20]. Here 85 time-series corresponding to 85 regions were extracted and a graph was created using the absolute Pearson's correlation between the time-series. The result for 100 runs using 5 non-overlapping *sub-graphs* is shown in Fig. 3.1(b) whereas results for 50 *sub-graphs* is illustrated in Fig. 3.2.

It is apparent that for lower number of graph divisions, the summation of *sub-graph* entropies is closer to the upper bound whereas for the higher number of graph divisions, the number is closer to the lower bound. Between the synthetic and real-world data (for number of *sub-graphs* $= 5$), the real-world brain network has lower values of *sub-graph*

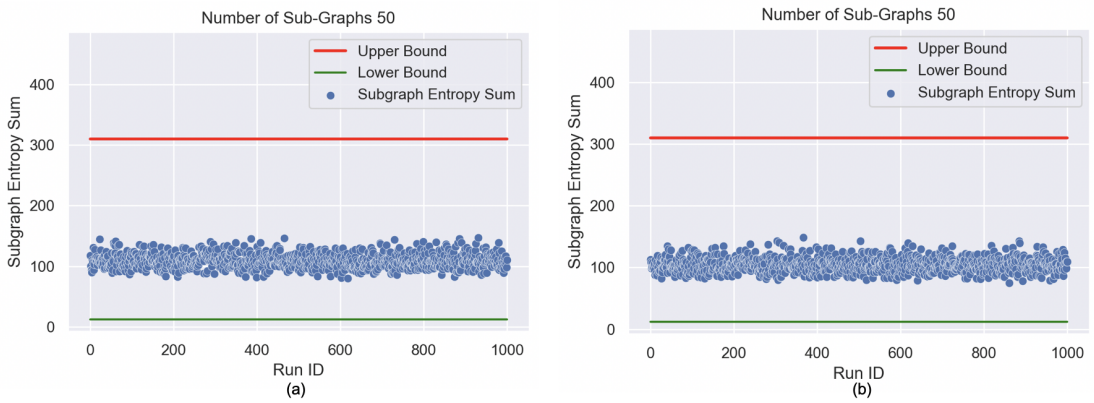

Figure 3.2: Upper bound and lower bound for a) Synthetic b) Real data. The division process was carried out 100 times and the blue circles denote summation of *sub-graph* entropies for each run.

entropy compared to the random network with weights uniformly chosen between $[0, 1]$. This may indicate that in real world brain data, the weights of the *sub-graphs* are more skewed which is representative of small-world properties of functional brain networks. On the other hand, when a graph is divided into many small sub-networks (Fig. S1 in SI), each *sub-graph* has almost similar uniform weight distribution. This makes the summation of *sub-graph* entropies similar for both real and synthetic dataset. For the synthetic data, lower bound and upper bound were 11.81 and 309.58, respectively, whereas for the real-world data, lower bound and upper bound were 11.56 and 309.58, respectively. In both cases, the upper bound is fixed. The graph entropy for the brain network is less than the synthetic network as well.

Stability for Sub-graph *(Node) Entropy:*

Synthetic Data. We followed the stability experiments described in [107] to create a synthetic graph dataset. For a node set V, a random network is defined as one that has edge between nodes (x, x') with with probability $q = 10/N$. The weight for each edge is picked from a uniform distribution $[0.5, 1.5]$. The stability or robustness is measured by change in node ranking when two types of noise are applied on edges. The noise has two parameters: the probability of change in the edge values and the amplitude of changes in values δ. A noisy version from a network is formed by first

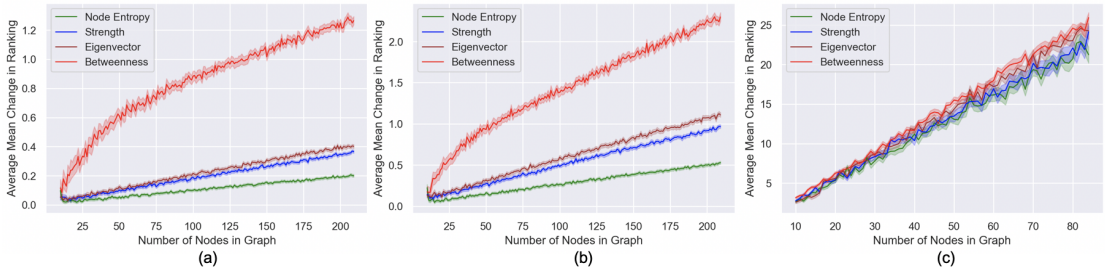

Figure 3.3: Results for different noise levels a) Type 1 noise with $p = 1$ and $\delta = 0.01$, b) Type 2 noise with $p = 0.1$ and $\delta = 0.1$, c) Results for rs-fMRI brain network. The bands around the curves represent 95% confidence interval. Node entropy always has lower average change in ranking.

choosing an edge by probability p and multiply the edge with a value sampled from uniform distribution $[1 - \delta, 1 + \delta]$. Type 1 noise has $p = 1$ and $\delta = 0.01$, and type 2 noise has $p = 0.1$ and $\delta = 0.1$. The first type of noise changes every weight with maximum 1% perturbation whereas the second type of noise changes 10% of weights with maximum 10% perturbation. 100 random networks were generated for number of nodes $n \in [10, 210]$. Each of the graphs was then perturbed using two types of noise. In order to illustrate the stability of *sub-graph* (node) entropy, the nodes were ranked for each network and its noisy version. The mean changes in ranking for 100 networks were calculated for networks with number of nodes $n \in [10, 210]$. We show the results in Fig. 3.3(a) for type 1 noise and Fig. 3.3(b) for type 2 noise. Node entropy is also compared with strength, eigenvector centrality and betweenness centrality.

From Figs. 3.3(a) and 3.3(b), node entropy has relatively less change in ranking. For all the centrality metrics, average mean change in ranking increases as number of nodes in the graph increases. For both type 1 and type 2 noise, the maximum average change in ranking is not more than 1 position. For strength and eigenvector, type 1 noise induced change in ranking is less than 1 for synthetic data. However, type 2 noise affects strength and eigenvector more, where the average change in ranking almost reaches 1 for large number of nodes. In both cases, betweenness centrality has relatively higher change in ranking between the original and noisy graphs compared to the other three types of centrality metrics [107, 116]. For type 1 noise, average change in ranking

reaches more than 1 position for betweenness centrality whereas for type 2 noise, the change is more than 2 positions.

Additionally, the maximum change in ranking were also computed for these two types of noises and the results are shown in Fig. 3.4(a) and 3.4(b). As expected, the average maximum change in ranking increases for all of the centrality metrics. For type 1 noise, maximum change is in range 0-2 for node entropy and 0-10 for others. For type 2 noise, maximum change is in range 0-5 for node entropy and 0-15 for others.

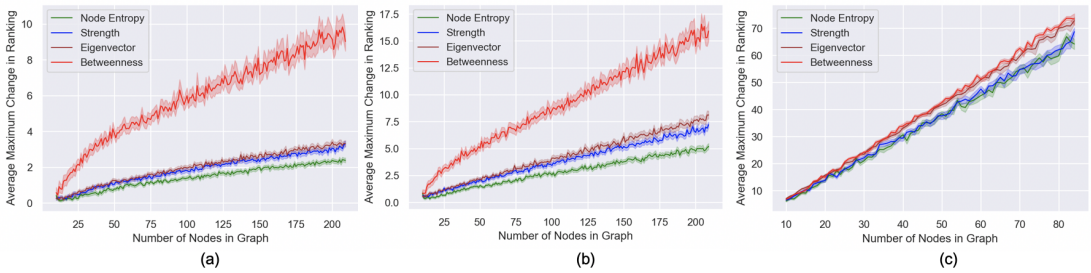

Figure 3.4: Results for different noise levels for maximum change in ranking a) Type 1 noise with $p = 1$ and $\delta = 0.01$, b) Type 2 noise with $p = 0.1$ and $\delta = 0.1$ c) Results for rs-fMRI brain network. The bands around the curves represent 95% confidence interval. Node entropy always has lower average maximum change in ranking.

Real-World fMRI Data. For the real-world data, 475 fMRI scans were taken from Human Connectome Project (HCP) database [29]. Each fMRI scan was converted into a brain network consisting of 85 regions following the regional percellations as mentioned in [20]. Two types of experimental conditions were chosen − a) resting state fMRI scan of each subject, and b) resting state and task (motor) fMRI scans of each subject.

In the first setting, we consider data of one subject as pure and data of another subject as an impure/noisy version of the network in this setting. In order to understand the effect of stability *vs.* number of nodes, a fixed subset of nodes were chosen at each run, and average and max changes in ranking were computed. Thus for each number of nodes and each run, one subject is chosen at random while its noisy version is chosen from the network of another subject. The process is run 100 times for number of nodes $\in [10, 85]$. For this experimental setting, average changes of ranking for noise for four centrality measures are plotted in Fig. 3.3(c). Additionally, maximum changes of ranking for noise for four centrality measures are plotted in Fig. 3.4(c). It is evident that

compared to betweenness centrality, the other three centrality metrics have less change in ranking. Although the 95% confidence intervals of node entropy falls within the corresponding intervals for strength, the estimated change in ranking for node entropy is lowest among all. However, there is a drastic change in mean and maximum change in rankings. The mean changes in ranking for node entropy vary between $2 - 21$ positions whereas the maximum changes vary between $5 - 65$.

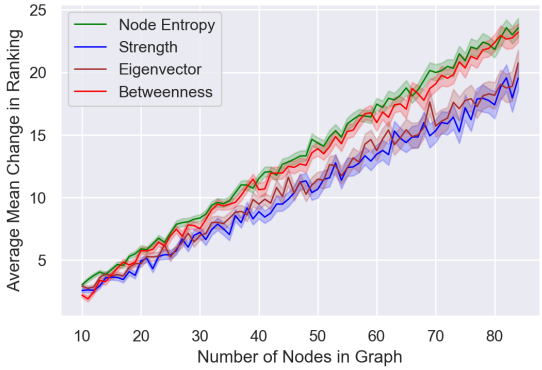

Figure 3.5: Results for mean change in ranking rest *vs.* task (motor) brain networks. The bands around the curves represent 95% confidence interval. Node entropy has relatively higher average change in ranking.

In the second setting, both resting state and task fMRI (motor) are considered. In this case, each person's resting state network is considered as the original graph and the corresponding task fMRI network is considered as noisy graph. Like the first setting, a fixed number of nodes were chosen at each run, and average and max changes in ranking were computed. Thus for each number of nodes and each run, one subject is chosen at random and its rs-fMRI network is used as the non-noisy network. Its noisy version is then defined from the t-fMRI network of the same subject. This process is run 100 times for number of nodes $\in [10, 85]$. The result for this experiment is illustrated in Fig. 3.5. In this case, node entropy has highest change in ranking, followed by betweenness, eigenvector and strength. Although node entropy shows little stability for change in fMRI tasks, that may indicate that the assumption of considering rs-fMRI and t-fMRI as noisy version of each other may not be justified. It is more probable that these two networks belong to two different classes of graph structures and thus the centrality

metrics have greater changes in rankings.

Conclusion and Future Work

In this chapter, two important properties of *sub-graph* entropy were derived. We demonstrated that dividing a graph into multiple non-overlapping *sub-graphs* increases the entropy. We showed that node entropy is stable compared to strength, eigenvector and betweenness centrality measures. We also illustrated that for real-world brain networks with two different induced states, node entropy has relatively higher change in ranking. Future work will be directed towards understanding the properties of *sub-graph* entropy with n-hop neighborhood.

Appendix

Lemma 1. For $0 < a, b < 1$, $|a \log a - b \log b| \leq |\log \sigma|\,|a - b|$, where $0 < \sigma \leq a, b$.

Proof.

Note that, $|a \log a - b \log b| \leq |a \log \sigma - b \log b|$, and $|b \log b - a \log a| \leq |b \log \sigma - a \log a|$, Thus,

$$|a \log a - b \log b| \leq |a \log \sigma - b \log \sigma| \leq |\log \sigma||a - b| \blacksquare$$

Lemma 2. For $w_1, w_2, c_1 \sim c_2 > 0$, $|(w_1/c_1) - w_2/(c_2)| \leq |1/c_1||w_1 - w_2|$

Proof.

$$\begin{aligned} &|(w_1/c_1) - (w_2/c_2)| \\ &= |(w_1/c_1) - (w_2/c_1) + (w_2/c_1) - (w_2/c_2)| \\ &\approx |(w_1/c_1) - (w_2/c_1)| \leq |1/c_1||w_1 - w_2| \blacksquare \end{aligned}$$

Chapter 4

Sub-graph Entropy based Network Approaches for Classifying Adolescent Obsessive-Compulsive Disorder from Resting-State Functional MRI

4.1 Introduction

Obsessive-compulsive disorder (OCD) is a serious psychiatric illness that affects about 2 - 3% of the population worldwide [117]. Onset of OCD is associated with excessive intrusive, unwanted thoughts (obsessions) and repetitive behaviors (compulsions). This chapter addresses discriminating and classifying the brain state of adolescents with OCD from healthy controls using resting-state functional magnetic resonance imaging (fMRI). Identifying features for discriminating OCD in adolescents is an important topic of research that could lead to useful clinical tools to aid in the diagnosis and management of youth with OCD. The current psychiatric diagnostic practices for adolescents include

interviews with youths and their parents by experienced clinicians, symptom rating scales and behavioral examinations [118] [119]. However, there are no evidence-based neurobiological markers available to aid clinicians in the diagnosis. Finding the brain regions and functional connections that are affected during OCD among adolescents is still an active area of research.

Past research has shown that fMRI is a useful tool for understanding psychiatric disorders [120] [121]. Broadly, fMRI provides a non-invasive way to measure activity of the brain during resting-state (rs-fMRI) or task (t-fMRI) using the change of blood-oxygen level dependent (BOLD) signal [122]. The fMRI scans of a person can be used to generate the functional connectivity network of the brain. In particular, rs-fMRI measures the spontaneous fluctuation of BOLD signal during awake rest. In case of many psychiatric diseases, the rs-fMRI signal is highly meaningful as it is not confounded by any task-based performance [7, 123]. The rs-fMRI signal from a given brain region can yield particular properties of neurobiological interest such as amplitude and signal entropy [120]. In this chapter, we are only concerned about the rs-fMRI analysis for adolescents with OCD and healthy controls.

The human brain is a network of interconnected nodes or regions functionally connected with each other [11]. Each regional brain activity is described by a time-series that is calculated by averaging all the time-series corresponding to the voxels for that region and the functional connection is measured by correlation coefficients between the regions [5, 12] . Recent advancements in neuroimaging and network theory offer tools that may be useful to advance understanding of psychiatric illnesses such as OCD. For example, entropy is a concept with origins in physics but more recently adopted by information theory and indexes unpredictability and complexity. A univariate measure of entropy can be calculated from any time-series data from a particular brain region. A multivariate measure of entropy can also be calculated to describe the complexity of a graph. We recently introduced the approach of examining entropy of *sub-graphs* which was capable of classifying brain states with high accuracy [20]. Furthermore, *sub-graph entropy* can be used to rank regions and edges within a brain network with respect to their differential values between two groups, and the ranking carries useful information about the disruption in brain network due to a disorder.

The goal of this study was to apply advanced rs-fMRI analytical approaches for

analyzing rs-fMRI data to classify adolescents with OCD *vs.* healthy controls. We used time-series, absolute correlation coefficients and graph-theoretic properties of functional network for these classifications. Although many brain network statistics exist in the literature and have been used to rank regions (nodes) or functional connections (edges), the proposed approach has never been applied to brain networks for diagnosing psychiatric disorders. First we used *univariate* (*e.g.*, Shannon wavelet entropy of each time-series), *bivariate* (absolute value of Pearson correlation) and *multivariate* (network features, *e.g.*, *local efficiency, global efficiency* [21], [5], *clustering coefficient* [22], *betweenness centrality* [23], *modularity* [24], graph and *sub-graph* entropy [20]) features for predicting OCD. These measures describe *segregation* or *integration* within the network. Next, network measures such as *sub-graph* entropy [20] and specifically those of nodes and edges were used to rank important brain regions and edges in each group of brain networks. In addition, the nodes and edges were also ranked by the extent to which they differentiated groups. This led to extracting a sub-network containing 120 edges, which was used for classification of OCD *vs.* controls.

Some of the above network measures have been used previously for comparing characteristics between two groups (*e.g.*, schizophrenia *vs.* healthy [120, 124], Alzheimer's disorder *vs.* healthy [123, 125], borderline personality disorder *vs.* healthy [61], and obsessive-compulsive disorder *vs.* healthy [126]). While these traditional association studies can extract statistically significant neural correlates for a disorder, in this chapter we extract a sub-network from resting-state fMRI data from two groups of adolescents that can predict whether a subject has OCD.

Table 4.1: Demographic and clinical characteristics of the OCD and control groups. CY-BOCS: Children's Yale-Brown Obsessive Compulsive Scale [1, 2]

Demographic Information	OCD	Control	t or χ^2	p-value
# of samples (n)	15	13	-	-
Age at onset − mean (SD)	9.5 (4.0)	-	-	-
Age at assessment − mean(SD, maximum, minimum)	15.3 (2.1, 19, 12.3)	16 (1.8, 18.8, 12.3)	$t = 0.98$	0.34
Male n(%)	8 (53)	7 (54)	$\chi^2 = 0.001$	0.98
Clinical Information − CY-BOCS	OCD	Control	t or χ^2	p-value
Obsessions, mean (SD)	9.4 (2.2)	0.1(0.3)	$t = 15.9$	< 0.001
Compulsions, mean (SD)	10.3 (1.7)	0.0 (0.0)	$t = 22.1$	< 0.001
Total, mean (SD, maximum, minimum)	19.7 (3.5, 27, 12)	0.1 (0.3)	$t = 19.9$	< 0.001

4.2 Materials and Methods

4.2.1 Dataset and Preprocessing

We describe the dataset and the preprocessing steps following the procedure outlined in [127]. Fifteen adolescents with OCD and 13 matched healthy control subjects were enrolled for the study. There were no significant differences between the OCD and control groups in terms of age, gender, socioeconomic status, IQ, ethnicity and handedness [127]. Children's Yale-Brown Obsessive-Compulsive Scale (CY-BOCS) checklist [1] was used to calculate scores on 4 factor-analyzed symptom dimension [2]. OCD patients had mean Y-BOCS score of 19.7 (standard deviation SD = 3.5, max 27, min 12) whereas the healthy controls had mean Y-BOCS score 0.1 (SD 0.3). Mean age for onset of the disease is 9.5 ± 4.0 years. The mean duration of the patients for the disease is 5.8 ± 4.2 years. Twelve out of 15 OCD subjects were on psychotropic medication. Details about age at assessment and clinical information for the adolescent are given in Table 4.1. More specifically, the mean age at the assessment for OCD subjects and controls were 15.3 (maximum 19, minimum 12.3) and 16 (max 18.8, min 12.3), respectively. Number of males in the groups were 8 and 7 for OCD and control groups, respectively. Resting-state fMRI scans (2 sessions each of 12 minutes duration) were taken using a novel multiband EPI sequence that accounts for acquiring multiple slices simultaneously [128]. The rs-fMRI scans were acquired with the following parameters TR = 1.15 s, TE = 30 ms, voxel size = 2mm isotropic, 60 slices, multiband factor = 4, echo spacing = 0.57 ms and number of 3D volumes = 600. During the scans, the subjects were asked to remain awake, eyes closed and not to think about anything in particular. More details about the data can be found in [127]. The experimental procedures involving human subjects described in this chapter were approved by the University of Minnesota *Institutional Review Board*.

FSL tool [129] was used for the pre-processing of the fMRI data. The steps included skull removal, distortion correction, motion correction and registration to Montreal Neurological Institute space (**MNI**). Using FSL program **melodic**, we analyzed the independent components and those corresponding to artifacts (heart rate, respiration, movement, white matter or cerebrospinal fluid) were removed. More details of the preprocessing can be found in [127]. After the preprocessing step, Desikan atlas [54]

was used to extract mean time-series for each of the 85 cortical and sub-cortical regions available in the atlas. The list of the regions used for the analysis is given in Appendix A Table A.5. Each time-series was then filtered by a band-pass filter with pass-band between 0.01 Hz - 0.15 Hz, followed by a decomposition into two frequency bands using a db-4 wavelet filter: lower (B1: 0.01-0.08Hz) and higher (B2: 0.08-0.15 Hz) [61].

4.2.2 *Univariate* Features

The complexity of rs-fMRI time-series was first investigated by using a *univariate* approach following [120]. Here we estimated the complexity of mean time-series extracted from each brain region through Shannon wavelet entropy [130]. We only focused our investigation of two frequency bands described above. Lower frequency band oscillations of BOLD signal have been shown previously to be adversely affected during a psychiatric disease *state* [131]. The Shannon wavelet entropy was estimated using techniques developed in [132] and [133] and implemented in the MATLAB Wavelet Toolbox (function wentropy.m). In short, the Shannon wavelet entropy is defined as:

$$E(s) = -\sum_i s_i^2 \log(s_i^2)$$

Here s is the mean time-series of a brain region for an individual, and s_i's are the coefficients of s in the orthonormal wavelet basis.

4.2.3 *Bivariate* Features

Pearson correlation coefficient ($P_{i,j}^f$) was calculated for each frequency band and the regions (r_i and r_j) where $i, j \in \{1, ..85\}$ as described in [60]. Let r_i^f be the mean time-series from frequency band f and region i from fMRI. Then, the Pearson correlation coefficient between two regions i, j is calculated by

$$P_{i,j}^f = P_{j,i}^f = \frac{E[(r_i^f - \hat{r}_i^f)(r_j^f - \hat{r}_j^f)]}{\sqrt{E[(r_i^f - \hat{r}_i^f)^2]}\sqrt{E[(r_j^f - \hat{r}_j^f)^2]}} \tag{4.1}$$

where $\hat{r}_i^f$ is the estimated mean of the time-series from frequency band f and region i. Thus two adjacency matrices were created for each pair of regions corresponding to two frequency bands. These matrices can also be seen as edges in a graph where each

node corresponds to one region. The total number of features for each frequency band was $\frac{85\times84}{2} = 3570$. Absolute values of Pearson correlations were used as features.

4.2.4 *Multivariate* Features

For each subject, two 85×85 adjacency matrices [60] containing absolute Pearson correlation were extracted. Suppose that a group of N brain networks from R regions and N subjects is specified by the adjacency matrix $C^k_{R\times R}$ where $k \in \{1, N\}$. $R \times R$ is the size of the adjacency matrix. Here $C^k(i, j)$ is the connectivity between two regions (i, j) for subject k. Ideally $C^k_{R\times R}$ is a binary matrix where existence of an edge is given by 1 and non-existence is given by 0. However, connectivity matrices extracted from fMRI are correlation values which are non-binary. In order to calculate the network features, first the matrices were *binarized* by keeping $\{5\%,\ 20\%,\ 35\%,\ 50\%\}$ of the edges. The sparsity of the networks for all subjects remained the same for a specific density.

Network Features

Adjacency matrices were used to calculate network characteristics using *Brain Connectivity Toolbox* (BCT) [1] . At a local (node) level in the network, three features, namely *local efficiency (LE), clustering coefficient (CC)* and *betweenness centrality (BC)*, were computed [60, 61]. At a global level, we calculated two features: *modularity* and *global efficiency* [60]. The local and global features in the network represent complementary viewpoints of the network for *segregation* and *integration* of nodes, respectively. Hence from each subject, we extracted $85 \times 3 \times 2$ (for 3 features at each node) $+ 2 \times 2$ (for *modularity and global efficiency*) $= 514$ network features corresponding to two frequency bands.

An overview of the network based features is discussed next as described in [134]. *Local efficiency* is computed using the summation of inverse of the shortest paths to the neighbors of a node. This metric is used to understand how efficient a node is for transferring information between two neighboring nodes. *Clustering coefficient* is calculated by the number of triangles created around a node out of all possible triangles. *Betweenness centrality* of a node is calculated as the percentage of shortest paths that contain

[1] `https://sites.google.com/site/bctnet/`

the node. *Modularity* metric measures how a network is sub-divided into smaller dense sub-networks with sparse inter-connections. *Global efficiency* describes the efficiency of information transfer within the whole graph. In addition, Network Based Statistics (NBS) [44] is used to extract important edges between two groups. NBS is a popular method for testing hypotheses about the edges in a network using t-test. It is used to identify connections and networks comprising the connectome associated with an experiment for a between-group difference. These network measures were also previously used for classifying OCD *vs.* healthy from fMRI data as described in [60]. More details of the network measures can be found in [22].

Sub-graph Entropy

We have recently shown that *sub-graph* entropy can effectively classify brain *states* for two different tasks [20]. *Sub-graph* entropy captures the interaction of local neighborhood of a brain region or functional connection in an entropy formulation. Although *sub-graph* entropy of a network (G) can be computed in multiple ways (*e.g.*, see [135], [136]), the scope of this chapter is restricted to only the complexity associated with the entries in the adjacency matrix for the network. Within this limit, the current model achieves remarkable accuracy for diagnosing a common psychiatric disorder. In particular the *sub-graph* entropy is defined as the number of bits required to encode the adjacency structure of the network [51] [23]. A brief description of *sub-graph* entropy (node and edge entropy) is presented next following [20].

A normalized adjacency matrix from one subject is defined as

$$Q^k = \frac{C^k}{\sum\limits_{i,j,j\neq i}^{R,R} C^k(i,j)}. \tag{4.2}$$

This definition normalizes the entries in the adjacency matrix so that their summation is 1. For bi-directional networks, we just normalize the upper triangular part of C^k. We also define $q^k_{i,j} = Q^k(i,j)$.

In this case, the graph entropy is calculated by [51]

$$H(G) = -\sum_{i=1}^{R}\sum_{j=1,i\neq j}^{R} q_{i,j}\log_2(q_{i,j}). \tag{4.3}$$

In our work we calculated the the matrix consisting of the indices $q_{i,j}$ as in Eq. 4.2. Graph entropy for a subset of a network was also computed and referred as *sub-graph* entropy.

Node Entropy: Node entropy was calculated based on the *sub-graph* containing a region and its neighbors. We defined neighbors based on the 1-hop distances from the node, *i.e.*, *sub-graph* containing nodes that are one edge away. Experiments involving 2-hop neighbors were also carried out and results from this analysis are presented in the Appendix B. The entries only signifying the interaction between one region and its neighbor were kept. All the other entries are forced to be zeros. Let the node entropy of node v_i is denoted by $H^k(G_{v_i})$ for subject k, then

$$H^k(G_{v_i}) = -\sum_{m=1}^{M} q_m^k \log_2(q_m^k), \tag{4.4}$$

where q_m denotes the normalized edge weight for neighborhood, and M represents the number of edges in the *sub-graph*.

After calculating node entropy for individual subjects, the node entropy from a group of N subjects can be estimated as follows.

$$H(G_{v_i}) = \frac{1}{N}\sum_{k=1}^{N} H^k(G_{v_i}) \tag{4.5}$$

An algorithm for ranking important regions based on node entropy is given in Algorithm 1.

Edge Entropy: Suppose region i is connected to j through edge e_{ij} where $i \neq j$. Similar to node entropy, the edge neighbors were also defined based on the 1-hop distances from the edge e_{ij}. In this case, we computed the edge entropy of subject k as $H(G_{e_{ij}})$ [20],

$$H^k(G_{e_{ij}}) = -\sum_{m=1}^{M} q_m^k \log_2(q_m^k), \tag{4.6}$$

where q_m denotes the normalized edge weight for neighborhood, and M is number of edges in the *sub-graph*.

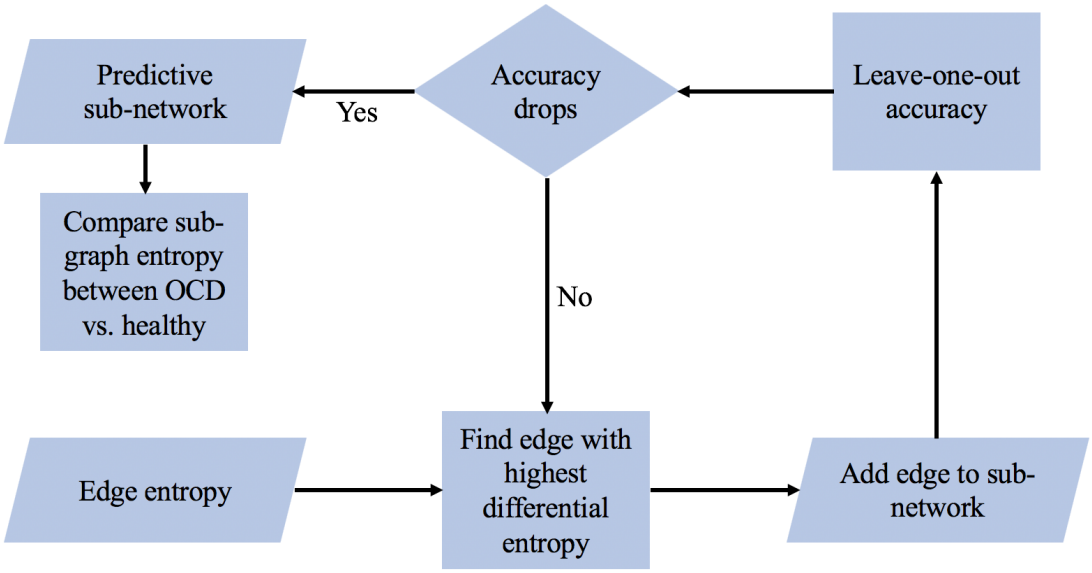

Figure 4.1: Procedure for extracting a predictive sub-network for OCD *vs.* healthy. Edges with highest *differential entropy* are selected to identify the sub-network based on leave-one-out accuracy. The sub-network's *sub-graph* entropy is compared between two groups using t-test for validation.

After calculating edge entropy for individual subjects, the group edge entropy from an ensemble of graphs can be estimated as follows:

$$H(G_{e_{ij}}) = \frac{1}{N}\sum_{k=1}^{N} H^k(G_{e_{ij}}). \tag{4.7}$$

An algorithm for ranking important edges based on node entropy is given in Algorithm 2.

Differential Sub-graph (Node and Edge) Entropy:

Between two groups of subjects, if the local *segregation* of brain regions change, the change in pattern can be captured using *differential entropy* [20]. In this case, the regions or edges which have the most change in entropies between two groups are most affected due to the change in the brain *state*. Suppose, for region i, the node entropy for subjects belonging to group G_1 (where $G_1 \in$\{Healthy, OCD etc\}) is given by $H_{G_1}(G_{v_i})$ and for group G_2, $H_{G_2}(G_{v_i})$. The difference between these two values would encompass *differential entropy* between two groups of subjects for region i. The change in entropy

is calculated as $|H_{G_1}(G_{v_i}) - H_{G_2}(G_{v_i})|$ where $|x|$ is the absolute value of x. This metric is called *differential node entropy* [20]. In our experiment, *differential node entropy* was calculated for each brain region and they were ranked based on *differential entropy* in decreasing value. The same argument and ranking procedure was applied to *differential edge entropy* as well. The algorithm is given in Algorithm 4. This process extracted nodes and edges that had changed the most due to the functional altercation during the disease.

Algorithm 4: Ranking of Regions and Edges for Two Groups

Data: Normalized adjacency matrices from two groups of fMRI-data

Result: Ranking of Regions and Edges Based on Differential Sub-graph Entropy

dEentropyRegion = $R \times 1$ Vector;
dRegionrank = $R \times 1$ Vector;
dEntropyEdge = $\frac{R(R-1)}{2} \times 1$ Vector;
dEdgerank = $\frac{R(R-1)}{2} \times 1$ Vector;
for $1 \leq i \leq R$ **do**
    Calculate $H_{G1}(G_{v_i})$ using Eq. (4.5);
    Calculate $H_{G2}(G_{v_i})$ using Eq. (4.5);
    dEentropyRegion(i) = $|H_{G1}(G_{v_i}) - H_{G2}(G_{v_i})|$;
end
for $1 \leq e_{ij} \leq \frac{R(R-1)}{2}$ **do**
    Calculate $H_{G1}(e_{ij})$ using Eq. 4.7;
    Calculate $H_{G2}(e_{ij})$ using Eq. 4.7;
    dEntropyEdge(e_{ij}) = $|H_{G1}(e_{ij}) - H_{G2}(e_{ij})|$;
end
dRegionrank = sort(dEntropyRegion) ;
dEdgerank = sort(dEntropyEdge) ;

4.2.5 Extracting Predictive Sub-network Based on Edge Entropy

In order to understand if *sub-graph* entropy measures contain predictive information, we used the edge entropy values for classification between two groups of subjects. Brain network measures have been used to discriminate between two groups in a number of previous papers to understand the significance, *e.g.*, see [60], [137]. In this framework, starting with the top-ranked edge, additional edges were added to the network in an iterative manner until the classification accuracy started dropping. At each iteration, the edge entropies of the sub-network were used in a leave-one-out fashion [138] for classifying OCD *vs.* healthy controls. Leave-one-out is a common cross-validation method for alleviating overfitting in case of small sample size classification problems which is often the case in psychiatry domain [124]. The classifier used in this case was support vector machine (SVM) with radial basis kernel based on testing different models where SVM resulted in a better performance. The procedure for finding the predictive *sub-network* is shown in Fig. 6.1.

Additionally, two more *sub-graphs* containing *union* and *intersection* of statistically different regions and edges were tested for predictive performance [20]. An anatomically defined *sub-graph* containing regions from CSTC network [127] was also used for baseline comparison of performance. In order to address the challenge of overfitting and establish the stability of predictive sub-network, the ranking procedure was run 28 times in a leave-one-out fashion. At each iteration, ranking was performed for 27 subjects except the left out. A histogram was then plotted for finding how many times top edges are extracted in the predictive sub-network.

4.2.6 Statistical Analysis

The *univariate*, *bivariate* and *multivariate* features along with node entropy and edge entropy values were compared using a 2-sided t-test across different groups. Their corresponding p-values were also calculated and shown. Furthermore, leave-one-out classification accuracy, specificity and sensitivity were calculated to validate our approach.

Table 4.2: Leave-one-out classification results

	Features	Accuracy	Specificity	Sensitivity
Proposed (edge) sub-network	120	**0.89**	**1**	**0.80**
Union sub-graph	145	**0.89**	**1**	**0.80**
Intersection sub-graph	114	0.86	0.92	0.80
CSTC sub-network	120	0.71	0.85	0.60
Node entropy [20]	85	0.71	0.62	0.80
Correlation [60]	5	0.71	0.85	0.60
Network features [60]	5	0.75	0.77	0.73
Correlation + Network features [60]	10	0.78	0.85	0.73
NBS [44]	95	0.64	0.54	0.73
Shannon wavelet entropy [120]	85	0.54	0.38	0.66

4.3 Results

4.3.1 Univariate Analysis

The classification performance of regional features using Shannon wavelet entropy is shown in last row of Table 6.1. In healthy controls and OCD patients, Shannon wavelet entropy was heterogeneously distributed throughout the brain with lowest Shannon wavelet entropy found in regions of the postcentral, cuneus, superiorparietal, paracentral and the highest was found in entorhinal, hippocampus, pallidum and thalamus. The regions that have significant difference in Shannon wavelet entropy are found in caudate, putamen, paracentral, postcentral, precuneus with $p < 0.05$ for band B1 (lower frequency band). Frequency band B2 (higher frequency band) did not have any statistical difference for Shannon wavelet entropy. The regions are shown in a brain template in Appendix B Fig. B.1.

4.3.2 Bivariate Analysis

Using a minimum redundancy maximum relevance (mRMR) in-fold feature selection [139], 5 features that are most important according to the criterion, were selected. The selected features belong to lower frequency sub-band (B1). The classification performance

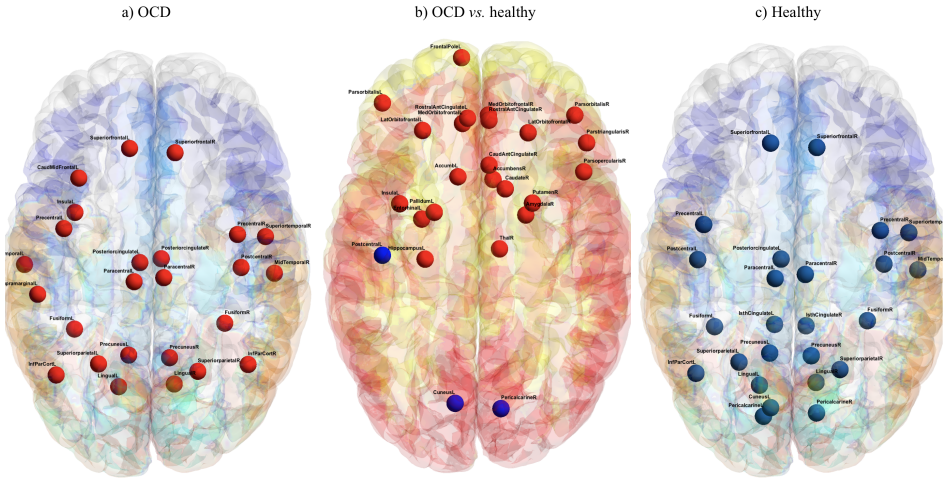

Figure 4.2: Visualization of important regions that have differences in entropy between OCD and healthy groups corresponding to frequency band B1 at network sparsity 35%. a) OCD, *red:* regions that have higher entropy. b) Differentiating regions between OCD *vs*. healthy, *red:* regions that have higher entropy for OCD, *blue:* regions that have higher entropy for healthy. c) Healthy *blue:* regions that have higher entropy for healthy.

by leave-one-out method was 0.71 with specificity 0.85 and sensitivity 0.60 (shown in Table 6.1) using the absolute Pearson correlation coefficients. The results showed that Pearson correlation between superior temporal gyrus - temporal pole was selected 26 out of 28 times during the mRMR feature selection and leave-one-out classification. Additionally, the edge weight between precuneus - precentral gyrus was selected 25 out of 28 times. The other important edge connections (absolute pearson correlation) are inferior frontal gyrus - mid frontal gyrus, pars operculum - insular cortex and inferior temporal gyrus- mid temporal gyrus [60].

4.3.3 Multivariate Analysis

Network Features

Following the *bivariate* experiment as described in previous section, an in-fold mRMR feature selection was employed (with 5 most significant features) using network based

features extracted from the functional brain graphs containing 85 regions. The leave-one-out classification accuracy using these five features was 0.75 with 0.73 sensitivity and 0.77 specificity (Table 6.1). Note that, clustering coefficient of putamen (at sparsity 35%) and hub property of cingulate gyrus (at sparsity 50%) were selected in each fold by the feature selection algorithm. The features and corresponding values for different sparsity levels for two groups are shown in Appendix B Fig. B.2. The selected features belong to lower frequency sub-band (B1).

Ranking of Brain Regions

The lower frequency band (B1) at network sparsity level 35% was used for calculating *sub-graph* entropy based on the classification performance. All results presented in the chapter and the Appendix B correspond to frequency band B1 and network sparsity level 35%. Using the strategy for group ranking as formulated in Eq. 4.5 and Algorithm 1, we identified important regions for OCD and healthy group separately (Fig. 4.2). The regions identified among the top-25 in each group are shown in Fig. 4.2(a) and 4.2(c), respectively. Most of the regions identified in this process belong to the default mode areas that are well known to be active during resting condition [7] [140]. A more interesting ranking process is the ranking of regions affected during OCD. This information is captured using the *differential node entropy* of nodes. The regions extracted using this procedure (Algorithm 4) are illustrated in two ways − 1) visualizing the nodes corresponding to highly ranked regions as shown in Fig. 4.2(b), and 2) listing the top-25 regions in Table 6.2. Furthermore, the corresponding *differential entropy* value and p-value for each region's node entropy are also shown in the same Table. There are 13 regions with statistically significant difference ($p < 0.05$) in node entropy among the 25 regions.

Note that the ranking can be validated for OCD by considering the regions from CSTC circuitry [127]. Our ranking methodology is able to capture the regions from that circuit in top 15% of these most important nodes. We illustrate the differential node entropy values for the regions in sorted order in Fig. B.3 (Appendix B). In addition, we also show the mean *differential entropy* value and standard deviation (SD) in the same figure. There are 13 regions with *differential entropy* more than 1-SD away from mean. Also, 38 regions have differential entropy values more than mean. Another

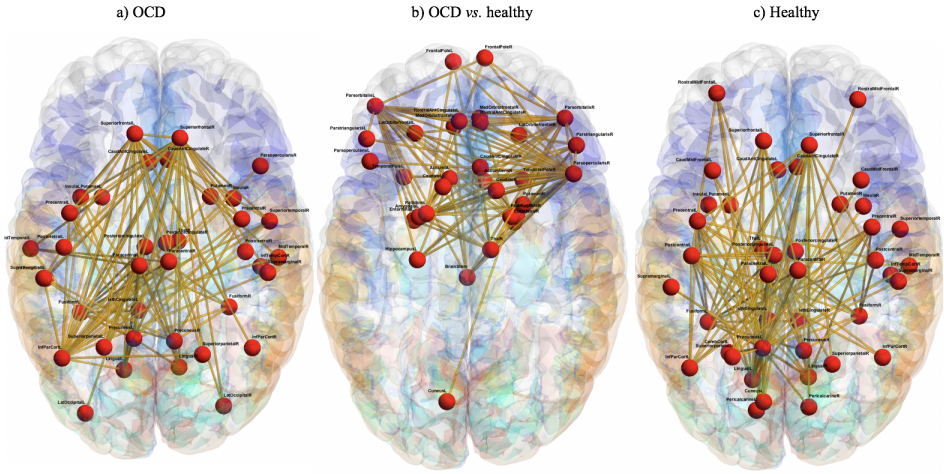

Figure 4.3: Visualization of important edges that have differences in entropy between OCD and healthy groups corresponding to frequency band B1 at network sparsity 35%. a) OCD, b) Differentiating edges between OCD *vs.* healthy. c) Healthy.

ranking scheme using 2-hop neighbors (here neighborhood for a node is defined based on distance of 2 edges from a node) revealed the most important regions to be similar to 1-hop neighbors (Table B.1 in Appendix B). The leave-one-out classification performance using all node entropy values is shown in Table 6.1 and is 0.71.

Ranking of Edges

The most important ranked edges are visualized by overlaying them on an MNI brain using BrainNet toolbox [55] (Fig. 4.3). The group ranking procedure based on edge entropy (Eqn. 4.7 and Algorithm 2 extracts top edges from healthy, and OCD separately as shown in Fig. 4.3(a) and 4.3(c), respectively. Top 100 edges were identified using the ranking process for each group. Additionally, the ranking based on *differential edge entropy* is also visualized in Fig. 4.3(b). A close inspection of the results reveals several observations. First, for each group ranking procedure reveals edges that are distributed throughout the lateral and medial cortical part of the brain and some of them belong to the default mode network. Second, *differential entropy* elevates the edges that belong to fronto-parietal and frontal-subcortical areas. The regions that are connected using

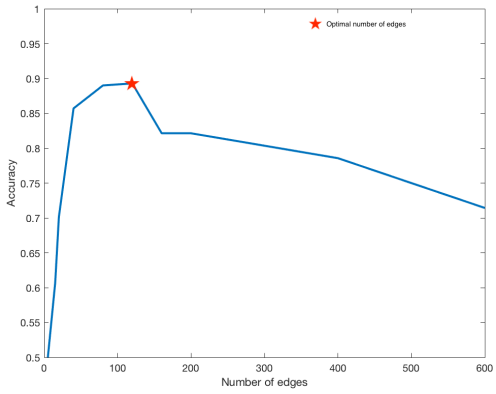

Figure 4.4: Average Leave-one-out accuracy *vs.* number of edges in sub-network.

the edges belong to frontal lobe, parietal lobe, anterior and posterior cingulate gyrus, thalamus proper, default mode (DMN), accumbens (striatal area) and amygdala. The corresponding differential entropy values for the edges are shown in sorted order in Fig. B.1 (Appendix B).

4.3.4 Extracting Predictive Sub-network

Accuracy of Predictive Sub-network

Following the method as outlined in Fig. 6.1, we ran our edge ranking procedure Algorithm 4 for edges 28 times, each time selecting top edges for leave-one-out classification. The change in classification accuracy with the number of edges using SVM and radial basis function kernel (using only selected edges) is shown in Fig. 4.4. The classification accuracy has a behavior similar to traditional feature selection algorithms where it improves up to 120 edges and then starts to decrease. In order to understand the significance of the current work with the information about sub-network, the result is compared with a number of baseline network based features in terms of classification accuracy. The comparisons of leave-one-out classification results are shown in Table 6.1. In addition, results for repeated random sub-sampling validation (cross-validation process run 100 times, each time randomly splitting the dataset into training 23 subjects and testing 5 subjects) are shown in Appendix B Table B.3. Edge entropies of the proposed predictive sub-network achieved 0.89 accuracy and correctly classify all healthy

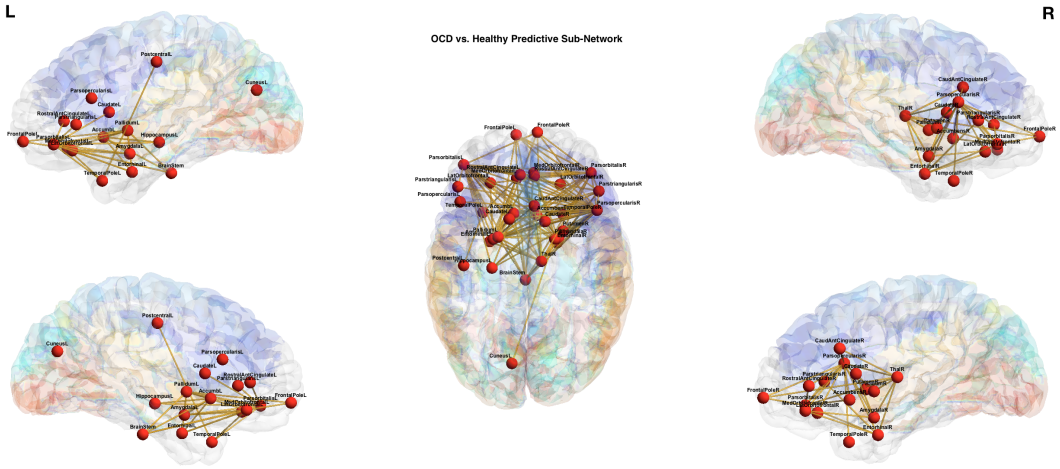

Figure 4.5: Predictive sub-network extracted using *differential edge entropy* and leave-one-out analysis. This network corresponds to frequency band B1 and density threshold of 35%.

and 12 out of 15 OCD subjects. Using 2-hop neighbor scheme for classification did not improve the accuracy (see Table B.2 in Appendix B). In our study, SVM was chosen based on the performance of multiple classifiers (e.g., support vector machine, linear discriminant analysis, artificial neural network and random forest). Their comparison of performance is shown in Appendix B Table B.4.

Sub-network Visualization

The identified sub-network comprising 33 region and 120 edges is shown in Fig. 6.2. In B.5 (Appendix B), we list the regions from predictive sub-network as well as well as the CSTC network. Top-50 edges from the sub-network are also listed in Table B.6 (Appendix B). In both cases, whether the regions or edges belong to CSTC network are also illustrated.

Statistical Analysis

We selected the top-120 features in each iteration for leave-one-out training, and plot their occurrence using a histogram as shown in Fig. B.5 in SI. The top ranked edges shown in Fig. 6.2 are also very important for classification as they are selected most of

the times as top edges. In addition, the predictive sub-network achieves a p-value of 0.0071 for a t-test of *sub-graph* entropies between OCD *vs*. healthy as demonstrated in Table 4.4. Similarly, CSTC sub-graph entropy is significantly reduced (p=0.0077) for OCD. The box plot for the t-test is shown in Fig. 6.3. To validate that the classifier performs significantly better than chance, permutation tests were performed, the results of which are shown in Fig. 4.7.

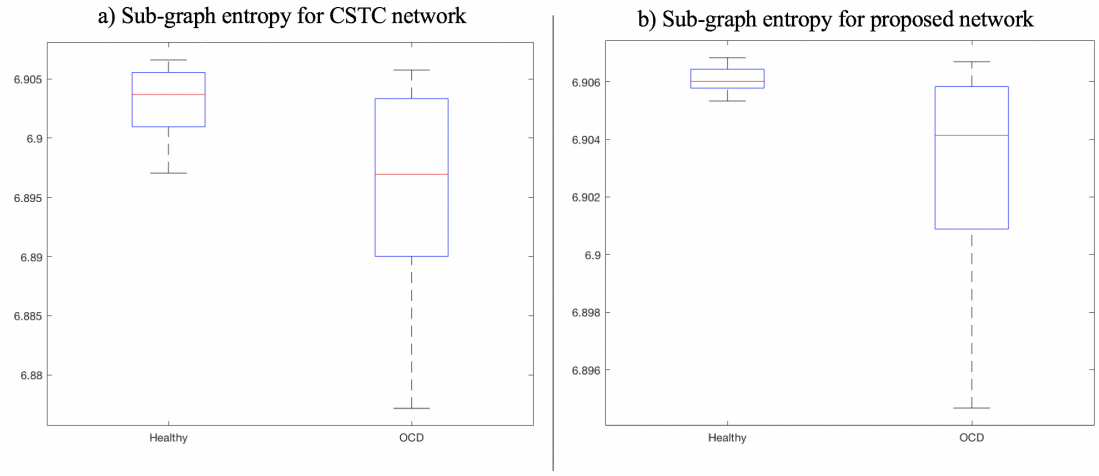

Figure 4.6: Box-plot of *sub-graph entropy* values for OCD *vs*. healthy, a) CSTC sub-network, b) predictive sub-network.

4.4 Discussion

This chapter investigates the feasibility of automated classification of adolescent OCD *vs*. matched healthy controls. It proposes the use of *information-theoretic sub-graph* entropy for ranking regions and edges from a group of brain scans and extracting a predictive sub-network for differentiating adolescent OCD patients from healthy. The predictive frequency band was found to be B1 (low frequency BOLD oscillation) at network sparsity level 35%. Key observations from different classification approaches are discussed in this section.

4.4.1 Regions and Edges

The present findings advance the method of resting-state fMRI analysis to examine neural networks in youth with OCD by network analysis; all prior methods had used standard, traditional approaches to examining functional connectivity [127, 141, 141–143]. Fitzgerald *et al.* [141] have found lower functional network connectivity in the cortico-striato-thalamo-cortical circuitry for youth OCD subjects in the age range 8-12. [141] also reported decreased amount of functional connections in the anterior cingulate cortex, striatal and thalamus areas. Gruner *et al.* [143] and Weber *et al.* [142] used independent component analysis (ICA), a multivariate blind source separation technique, to analyze whole brain functional network of adolescent OCD subjects. Functional connectivity scores corresponding to each component were observed to be significantly higher among OCD patients in comparison with matched healthy controls in anterior/ posterior cingulate cortical areas and significantly sparser in visual cortical areas. [142] also reported reduced functional connections in the cingulate cortex. Bernstein *et al.* [127] found decreased connectivity between putamen and lateral prefrontal cortex. Also, [127] found lower connectivity between the putamen and the right insula and operculum.

Using the methods described here, we were able to capture previously known regions for resting-state fMRI scans from healthy humans [144]. Notably, all of the top-ranked regions that were identified to have high node entropy values for each group are default mode network nodes associated with resting-state. In addition, the OCD group showed higher regional entropy for regions such as thalamus, hippocampus, accumbens, putamen, anterior cingulate, postcentral gyrus, amygdala, pars-orbitalis and pars-opercularis as shown in Fig. 4.2. Interestingly, the high ranking of the thalamus and hippocampus regions by the proposed differential entropy approach is consistent with the traditional hypothesis that these regions are affected for subjects suffering from OCD. The regions and edges that had most difference between healthy *vs.* OCD consist of accumbens, amygdala, thalamus, pallidum which are part of the CSTC circuit [127] in brain. This circuit is shown in Fig. B.6 in Appendix B. The intersection between CSTC and predictive sub-network is also illustrated in Fig. B.7 (Appendix B).

In Fig. 4.3 and Fig. 6.2, we show the top ranked predictive edges between important brain nodes for two groups (OCD *vs.* controls). The predictive network consists of many regions that act as hub [12], *i.e.*, they consist of a number of edges that differentiated

OCD group from healthy controls. Some of the edges include connection from operculum to putamen, accumbens, thalamus. Furthermore, edges from frontal pole to striatal regions also form a substantial part of the predictive network. The edge between amygdala and occipital lobe (cuneus) also distinguished OCD patients and healthy, which is notable as it represents a connection linking the default mode network and the limbic network. Edges that are not common between CSTC and predictive network are shown in Fig. B.8 and B.9, respectively. These plots illustrate how the proposed sub-network differs from the CSTC network. While the use of the edge entropies of the CSTC sub-network achieved an accuracy of 0.71, that of the proposed sub-network led to an accuracy of 0.89. This emphasizes the importance of including whole-brain data in the analysis, rather than focusing on just the CSTC. Although classifying OCD with high accuracy has been known to be difficult, the proposed sub-network improves the achievable accuracy significantly compared to all prior approaches.

At a group level, the top discriminating links between OCD *vs.* controls are also statistically significant ($p < 0.05$). The individual edge entropy measures are useful metrics for classification as the proposed classifier significantly outperforms the classification with Pearson correlation coefficient values. However, the *sub-graph entropy* has significant reduction for OCD patients for both CSTC network and predictive sub-network as shown in Fig. 6.3.

Fig. 4.2 shows a number of nodes that differentiated OCD versus controls, and they are mostly *red*, signifying that they had higher entropy in OCD than controls. However Fig. 6.3 shows that for both the CSTC network and the predictive network *sub-graph* entropy is lower. Although the nodes in OCD subjects tend to have higher node entropy, the *sub-graphs* used to calculate the node entropy consider only the neighbors the node is connected with. The predictive *sub-graph* is a different *sub-graph* that is extracted considering the most predictive edges based on edge entropy. The apparent difference in these two indicate that, although the nodes (that might be part of predictive sub-network) may have higher node entropy, the overlap of the edges (containing the nodes) that belong to the predictive sub-network is lower. In addition, this also indicates that the edge weights (in the predictive sub-network) are relatively well distributed in healthy controls (that lead to higher *sub-graph* entropy), and skewed in OCD patients (the lead to low *sub-graph* entropy).

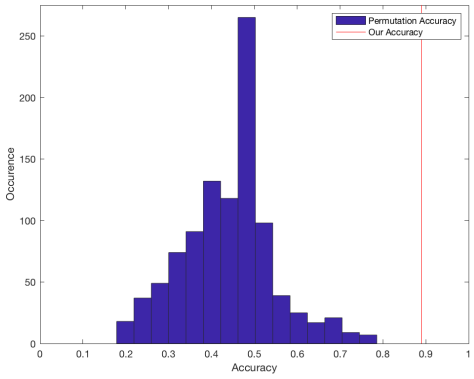

Figure 4.7: Results of permutation test on OCD data. The labels for healthy and OCD are permuted and a SVM classifier is fitted to each new dataset. Histogram of accuracies and accuracy on actual data is shown.

4.4.2 Misclassified Subjects

The OCD severity (CY-BOCS) of the patient group varied between 12-27. The mean, standard deviation and median were 19.7, 3.5, and 20, respectively. The OCD severity of misclassified subjects were 12, 15 and 19, respectively. Two of the misclassified subjects were under medication and one was non-medicated. The misclassified subjects fall in the lower end of CY-BOCS for the group of subjects. The inability of the classifier to distinguish these patients may indicate that these subjects had relatively mild level of OCD symptoms as indicated by their CY-BOCS score. The classifier identified them to fall in healthy group. A histogram illustrating the OCD severity of subjects and the CY-BOCS score for misclassified subjects is shown in Appendix B Fig. B.10.

4.4.3 Validation

The binomial test on the classification using the proposed sub-network also shows that they have statistically significant predictive performance ($p = 7.9497 \times 10^{-06}$ for OCD *vs.* healthy with respect to a naive classifier and $p = 0.0009$ with respect to [60]). In order to further validate the *information-theoretic* model, a sub-network containing only regions from CSTC circuits is extracted as shown in Fig. B.6 and the *sub-graph* entropy between patient *vs.* control group is compared as shown in Fig. 6.3. CSTC *sub-graph* entropy is significantly reduced (p=0.0077, as illustrated in Table 4.4) for OCD. In

order to avoid potential problem with overfitting, leave-one-out classification with in-fold feature selection was used in every experimental setting. Note that this makes sure that the classifier is learning features from the training set and using the learned feature for finding the test accuracy in order to generalize the diagnosis to previously unseen subject.

Although the classification used in this chapter is leave-one-out, the result is robust even in the case of 5-fold cross validation and repeated random sub-sampling validation. For 5-fold CV, the dataset was divided into 5 sets each consisting of 5, 5, 6, 6, 6 subjects (5-folds), respectively. In each fold, one set was used for testing and others for training. We found out that edge entropy with 120 features achieve the same accuracy, specificity and sensitivity as leave-one-out. For repeated random sub-sampling validation, the cross-validation process was run 100 times, each time randomly splitting the dataset into training (23 subjects) and testing (5 subjects). The results for this procedure for each types of features are shown in Appendix B Table B.3. Edge sub-network and Union sub-graph achieved accuracy of 0.87, specificity of 0.96 and sensitivity of 0.79. All these values are within 4% of leave-one-out accuracy and better than the performance of other features.

In order to reinforce our conclusion that the classification performance of the extracted predictive network from the model are better than baseline models, permutation tests were performed. In this vein, a 'naive' baseline model was created effectively by permuting the labels in the training and test set. Thus the baseline model removed all the signals associated with OCD from the labels − the leave-one-out classifier then learned the relationships between the edge entropy and permuted labels. The actual learned model performed significantly better than baseline which suggests that the classification scheme outlined before is also statistically significant. Here, for OCD *vs.* healthy dataset, 1000 iterations were performed where each time, labels were permuted and then trained using an SVM model on the training subset of this set and tested on the rest. Fig. 4.7 shows the distributions of accuracy values for the dataset. In this scenario, there is a significant distance between the centre of the accuracy distribution and the accuracy produced by the predictive sub-network.

4.4.4 Predictive Sub-network as Part of Other Known Networks

Our results implicate regions and edges from a number of large-scale brain networks. Here we discuss potential interpretations for the involvement of these networks in adolescent OCD.

Default Mode Network (DMN)

The default mode network of human brain consists of regions that are active when a person is awake but resting and not doing any particular task [7,145]. The DMN regions are typically associated with mind wandering, day dreaming, thoughts about the self, and ruminations etc. In our analysis, the top regions, edges and predictive network extracted using *sub-graph* entropy consist of regions from the DMN. This may indicate that adolescents suffering from OCD can get "stuck" in repetitive thought patterns. Previous works also support the hypothesis that OCD involves abnormalities of the DMN [146–148].

Dorsal Attention + Salience

The dorsal attention network contains regions that show increased activation when a subject is deciding where to focus the attention in a proactive way. The salience network provides the mechanism to attend the important cues that stand out compared to the background. In our results, the predictive sub-network contains regions (entorhinal) from dorsal attention [149, 150] network. Moreover, it contains the hippocampus which is part of salience network [151–154]. The functional regions and edges containing salience and dorsal attention indicate that OCD subjects may deploy attention and attending visual cues differently from healthy adolescents [155–157].

Executive Network

The executive network, which consists of fronto-parietal brain regions, is responsible for high level cognition functions, such as, problem solving, and decision-making. The predictive sub-network implicated for adolescent OCD includes many regions from frontal part of the brain (Fig. 6.1), *e.g.*, orbitofrontal, fontal pole, parsorbitalis, and also parietal part of brain, *e.g.*, postcentral gyrus. Their involvement in prediction performance

may indicate the change in executive functions in OCD patients compared with healthy subjects [147, 158, 159].

Limbic Network

Finally, the predictive sub-network contains the following regions from limbic system - hippocampus and amygdala. Limbic regions play a critical role in mediating emotional responses and forming new memories. This functional network has been shown to be affected for OCD patients in a number of previous studies [160–162]. Specifically, amygdala had higher node entropy value compared with controls, which may indicate its utility for relieving the elevated anxiety level for OCD patients.

4.5 Conclusion and Future Work

Using an *information-theoretic* network approach, this chapter has identified a predictive sub-network of the brain that can be used to discriminate brain networks of adolescents with OCD from healthy controls. The regions and edges that are found to be most important based on *differential entropy* are also found to be statistically significant. The predictive sub-network contains brain regions from well known large-scale brain functional networks. Their involvement implies possible impairment of brain function of adolescents suffering from OCD. However, one limitation of the current work is the small number of participants in each group. Therefore, future work needs to be directed towards analysis of datasets with larger sample size. In addition, features and classifier models need to be developed to predict the onset of OCD and other psychiatric disorders like depression. Future work may also be directed towards classification based on frequency-domain features.

Table 4.3: Top-25 regions extracted using *differential node entropy* for OCD *vs.* healthy controls.

Rank	Region / Hemisphere	Diff. Entropy	p-value
1	Parsopercularis - R	1.5099	**0.0002**
2	Thalamus Proper - R	0.9660	**0.0129**
3	Parsorbitalis - L	0.9252	**0.0459**
4	Cuneus - L	0.9098	**0.0153**
5	Accumbens Area - L	0.9095	**0.0159**
6	Postcentral - L	0.9021	**0.0065**
7	Parsorbitalis - R	0.8944	**0.0427**
8	Pallidum - L	0.8514	0.0944
9	Medial Orbitofrontal - L	0.8303	**0.0476**
10	Parstriangularis - R	0.8233	**0.0500**
11	Medial Orbitofrontal - R	0.8090	**0.0392**
12	Amygdala - R	0.7317	0.1534
13	Hippocampus - L	0.7103	0.1503
14	Lateral Orbitofrontal - L	0.6737	0.1846
15	Caudate - R	0.6620	**0.0234**
16	Rostral Anterior Cingulate - R	0.6574	0.1239
17	Rostral Anterior Cingulate - L	0.6378	0.1657
18	Lateral Orbitofrontal - R	0.6201	0.2251
19	Pericalcarine - R	0.6192	**0.0188**
20	Caudal Anterior Cingulate - R	0.6165	0.2049
21	Entorhinal - L	0.6147	0.1431
22	Frontal Pole - L	0.5782	0.2752
23	Insula - L	0.5692	0.1392
24	Putamen - R	0.5565	**0.0318**
25	Accumbens Area - R	0.5419	0.1184

Table 4.4: Statistical analysis of predictive sub-network and CSTC network using *sub-graph* entropy.

	# of nodes	# of edges	Sub-graph entropy		p-value
			Mean	SD	
Proposed sub-network	33	120	Healthy: 6.9061 OCD: 6.9028	Healthy: 0.0004 OCD: 0.0039	**0.0071**
CSTC sub-network	16	120	Healthy: 6.9030 OCD: 6.8951	Healthy: 0.0032 OCD: 0.0090	**0.0077**

Chapter 5

Predicting Biological Gender and Intelligence from fMRI via Dynamic Functional Connectivity

5.1 Introduction

This chapter presents classification and regression approaches to predict gender and intelligence of humans from the functional magnetic resonance imaging (fMRI) of the brain. In particular, the chapter investigates the predictive power of *dynamic* functional connectivity (dFC) for classifying biological gender and intelligence metrics. The results are compared with *static* connectivity and it is shown that dFC is predictive of two important phenotypes in humans. We use a large dataset containing task and resting state fMRI data of 475 subjects (each subject performed 7 tasks, *e.g.*, *emotion, gambling, working memory, relational, social, motor, language* as well as rest) from the Human Connectome Database [29] to test the classification method.

Dynamic functional connectivity of human brain refers to change in spatio-temporal organization of neuronal units over time [13, 38]. *Dynamic* connectivity was known previously to exist for brain scanning modalities with rich temporal resolution, *i.e.*, electroencephalography (EEG), magnetoencephalography (MEG) [163–167]. However, only recently dFC was shown to be present in functional magnetic resonance imaging

(fMRI) [168]. Since then, several papers have investigated how dFC correlates with demographic characterization (e.g., age [169], gender [170], intelligence [171] and cognition [172]). *Dynamic* functional connectivity has also been demonstrated to be associated with disease states [173–175]. There has been an interest in using dFC for individual characterization specifically for prediction studies − dFC was used in [176, 177] for classifying gender [176], psychiatric disorders [178] and for predicting attention load [179].

Given the plethora of work with evidence that dFC is an important phenomena in *neuroimaging*, our understanding is still constrained about the possible personal characteristics that can be predicted based on dFC. This chapter shows that dFC can contribute substantially towards forming a *fingerprint* for classifying biological gender and predicting intelligence quotient (IQ) based on behavioral tasks. Predicting IQ from dFC has not been reported in literature before, and is a major contribution of our work. Additionally, it is shown that dFC can match, or sometimes outperform, other standard MRI-based models for classification of biological gender [176]. In this vein, this chapter presents a novel way to extract dFC *states* from task fMRI (t-fMRI) and resting state fMRI (rs-fMRI). The *states* are formulated as a constrained tensor decomposition problem that has unique solution. An algorithm utilizing alternative least square technique is derived that identifies the unique component *states*.

The chapter considers the analysis of both task-fMRI (t-fMRI) and resting-state fMRI (rs-fMRI). A brief description of t-fMRI or rs-fMRI is given next. During t-fMRI, the person performs a number of repetitive tasks, *e.g.*, tapping fingers, watch pictures, make decision etc. while inside the scanner. These behaviors invoke the hemodynamic response known as blood-oxygen level dependent (BOLD) signal corresponding to the repetitive task [122]. Task fMRI contain valuable information about a subject's behavioral abilities, gender [180], age [181]. On the other hand, rs-fMRI measures the spontaneous fluctuation of BOLD signal during awake rest. In case of many psychiatric illnesses, rs-fMRI signal of the patient is highly meaningful and predictive of individual traits [182] and psychiatric disorder [7, 25, 183].

5.1.1 Prior Work

Gender effect on dFC is not well characterized

In recent years, a number of studies have found brain functional connectivity differences for different biological gender using various neuroimaging modalities. These differences are especially prominent in several cognitive and behavioral characteristics, such as verbal abilities, working memory abilities and spatial orientations [184]. However, these studies have mainly addressed the psychometric or behavioral differences at the group population level. Whether functional connectivity differences have predictive capability of biological gender is of utmost interest. A few prior publications have also investigated functional and anatomical brain network dissimilarities for classifying male *vs.* female [185–187]. Anatomical connectivity differences for biological gender were reported in [185] using structural diffusion tensor imaging (DTI). Zhang et al. [186] used rs-fMRI and partial least square modeling to classify gender. Moreover, global network properties extracted from *static* connectivity were found to differ in emotion regulation [187]. Stronger functional connectivity has been noticed in default mode network for females. Particularly, Buhm et al. [188] concluded that functional networks consisting of posterior cingulate cortex (PCC), precuneus and bilateral medial prefrontal cortex are active for females in rs-fMRI. Strong intra-hemispheric network connectivity were reported in females whereas strong inter-hemispheric connections were prominent for males [189] during rest. Similar conclusion was also reached in the case of anatomical networks [190]. Although predicting biological gender based on *static* functional connectivity and anatomical connectivity are well studied, there is lack of scientific literature on understanding the predictive ability of *dynamic* connectivity for biological gender. Recent work by [176, 177] have made preliminary progress in this direction. Menon et al. [176] were successful in classifying biological gender based on intrinsic functional connectivity such as edge consistency, edge variability and differential power measures. The partial *static* connectivity and dFC were able to classify biological gender with an accuracy of 0.90 and 0.80, respectively in a leave-one-out model. Default Mode Network, visuospatial networks were found have moderate variability among groups. Additionally, fronto-parietal and attention networks had high functional variability. Cai et al. [177] performed an association study using rs-fMRI data to investigate biological

gender differences. This study employed a novel GICA-TVGL framework and found out that males and females have significant differences with respect to visual network. Additionally, differences in dFC state transition time was reported.

IQ affect on dFC is not well characterized

Similarly, the predictability of IQ from dFC is not well characterized. A few studies have attempted to associate and predict individual intelligence metrics from structural and functional MRI until now. Among them, the work by Finn et al. [191] was able to successfully establish the importance of *static* connectivity to predict fluid intelligence using a cross-validation and machine-learning modeling. Additionally, Dubois et al. [192] conducted a study by utilizing a fully cross-validated model to show that functional connectivity in human brain could predict 20 percent of the total variations for the intelligence distribution in population. The model was built by the factor analysis of intelligence scores for 10 different tasks. Similar study was carried out in [193] and it was concluded that functional activation maps of brain is predictive of general intelligence. Although progress has been made to associate intelligence with functional connectivity profile of brain, very few studies have demonstrated the predictability of intelligence quotient (IQ) using non-stationary functional profile of brain activity. In addition, more work needs to be done to understand whether finding from one cohort of subjects can directly be extrapolated to different sub-groups of populations.

Computing Dynamic Functional Connectivity

The most common way of extracting dFC from fMRI is by sliding-window correlation matrix. Since fMRI is spatio-temporal, one can conceive of the network of the spatial pattern to be *dynamic* instead of *static*. A very interesting direction in fMRI neuroimaging study is the extraction of spatial couplings that vary over time. In order to extract the spatial couplings, blind source separation (BSS) models, in particular, independent component analysis (ICA), non-negative matrix factorization, principal component analysis and tensor decomposition, have been widely adapted in data-driven pattern studies [14–16, 194]. A study by Kiviniemi et al. [16] investigated the stability of ICA components over time segments to understand the changes in spatial coupling of the default mode network. In another model, an atlas is used to parcellate the brain

into spatial maps using BSS, where each map has distinct time courses associated with it. Following this, the time-varying property of the component time courses [17] is captured by calculating Pearson's correlation using windowing [19, 195]. Following this, ICA, PCA, etc. are performed to find out the brain states. Although PCA and ICA are widely used for extracting *dynamic* functional connectivity, they suffer from two drawbacks. PCA decomposition constrains both connectivity maps as well as the time courses (activity level) of the maps to be orthogonal to other maps and time courses. This can severely hamper the expressiveness of model. ICA can overcome the orthogonality constraint in the time domain, although the uniqueness of spatial maps requires the sources to be non-Gaussian. Tensor decomposition, specifically PARAFAC decomposition can alleviate both concerns, as the required constraints can be added to a particular mode without affecting other modes.

5.1.2 Contribution

The contribution of this chapter is four-fold.

- The chapter presents *yet* another method for extracting dFC from sliding window correlation using tensor decomposition. The uniqueness conditions for the tensor decomposition are formulated. In addition, we provide an algorithm utilizing alternating least square based approaches for finding the unique decomposition.
- The chapter investigates the importance of dFC for biological gender classification from fMRI. It is shown that gender can be predicted accurately from most of the task-related connectivity patterns in brain.
- The chapter successfully demonstrates the importance of dFC for prediction of intelligence metrics from fMRI. We find that subject-wise weights of *dynamic* spatio-temporal maps are predictive of intelligence.
- The chapter proposes a novel method to extract related *dynamic* sub-networks associated with gender and intelligence prediction. Statistical tests are also carried out to validate the significance of the proposed sub-networks.

5.2 PARAFAC-based Decomposition Model

5.2.1 Notations

In this chapter, tensors are denoted in caligraphic letters (*e.g.*, $\mathcal{X}$), matrices in uppercase letters (*e.g.*, A) and vectors in lowercase letters (*e.g.*, a_f). $||.||_F$ denotes Frobenius norm, $\odot$ denotes Khatri-Rao product, $*$ denotes Hadamard product.

5.2.2 Preliminaries

Regional time-series from each fMRI scan are extracted and they are reshaped to a matrix (dim 1 = spatial, dim 2 = temporal. From this matrix, a new *dynamic* connectivity matrix based on sliding window of pre-defined strides are formed. More details can be found in Section III (Experimental Setup). In brief, each subject's regional time-series yield multiple time-series windows based on their strides, which are then used to create Pearson's correlation between regions for each time-window. Following this, the Pearson's correlation matrices are vectorized and multiple connectivity vectors are stacked to create a dFC matrix for each subject where (dim 1 = edges, dim 2 = temporal). The scans from a group of subjects are concatenated to form a 3-way tensor where the dim 3 = subject. We denote the 3-way tensor of size $I_1 \times I_2 \times I_3$ as $\mathcal{X}_{I_1,I_2,I_3}$.

5.2.3 Traditional PARAFAC

Traditional unconstrained PARAFAC [196] modeling for decomposing a tensor $\mathcal{X}_{I_1,I_2,I_3}$ into F number of rank-1 tensors can be written as

$$\mathcal{X}_{I_1,I_2,I_3} \;=\; \sum_{f\,=\,1}^{F} a_f \circ b_f \circ c_f, \;\; \mathcal{X} \;=\; (A, B, C) \tag{5.1}$$

where A, B, C are of size $I_1 \times F$, $I_2 \times F$ and $I_3 \times F$ respectively. $a_f = A_{:,f}$, $b_f = B_{:,f}$, $c_f = C_{:,f}$ where $A_{:,f}$ is the f^{th} column of A and $\circ$ denotes outer product. For unconstrained PARAFAC decomposition, each rank-1 tensor will consist of one matrix (A) representing spatial couplings (column in A), corresponding time variation of the component (each column of B) and the distinct weights of the time-varying spatial-coupling map for each subject (column in C). Precisely, this decomposition optimizes

the following function:

$$\min_{A,B,C} ||X_1 - (C \odot B)A^T||_F^2 \tag{5.2}$$

where $X_1 = X_{I_2 I_3, I_1}$. More specifically, X_1 is tensor $\mathcal{X}$ reshaped as a matrix with number of rows $I_2 \times I_3$ and columns I_1. Likewise we also define $X_2 = X_{I_3 I_1, I_2}$ and $X_3 = X_{I_2 I_1, I_3}$ where X_2 and X_3 correspond to reshaped matrix form of tensor $\mathcal{X}$. Previous works have shown that unconstrained PARAFAC decomposition itself is unique under very mild conditions [196–198].

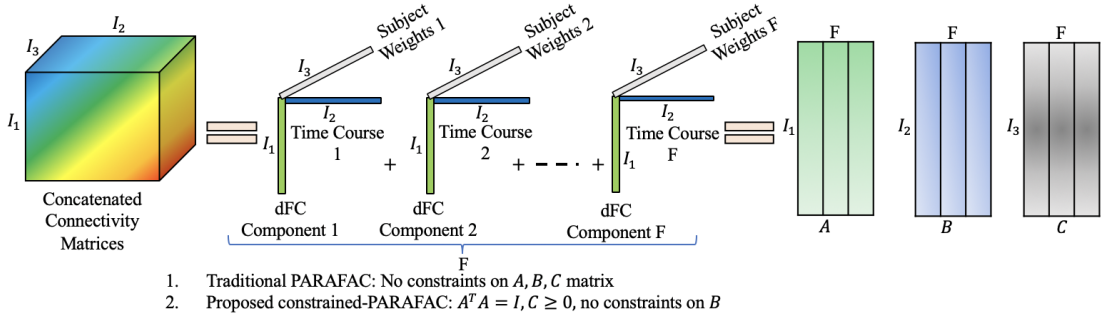

Figure 5.1: PARAFAC decomposition conceptual illustration. A 3-D tensor is divided into rank-1 tensors where each of then is outer product of three vectors. The outer product vectors for each dimension from rank-1 tensors are collected in matrices.

5.2.4 Constrained-PARAFAC

Although unconstrained PARAFAC tensor may have unique decomposition under mild conditions, the optimization process used to find the decomposition matrices may introduce many correlated components [196]. Moreover, in the case of decomposing *dynamic* connectivity tensor into common spatio-temporal components, it may introduce connectivity profiles that are hard to interpret from a biological perspective. Thus in order to alleviate these two problems, we introduce orthogonality in dim -1. This guarantees that the spatial connectivity components extracted from the tensor are uncorrelated. In addition, we ensure that the decomposition profile is validated by previous work on BSS for fMRI (using ICA, PCA) which follows the hypothesis that cross-talk among spatial-coupling should be small [178, 199]. These two cases are satisfied by using $A^TA = I$, where I is a identity matrix. Also, for interpretability, we can assume the weighting of

spatio-temporal maps in each subject to be non-negative ($C \geq 0$). Thus, decomposition problem has milder uniqueness conditions than traditional PARAFAC. The corresponding uniqueness and an efficient algorithm for finding these components are derived later. A conceptual illustration of PARAFAC and the proposed constrained-PARAFAC models is given in Fig. 5.1.

The corresponding optimization is stated as:

$$\min_{\tilde{\mathcal{X}}} ||\mathcal{X} - \tilde{\mathcal{X}}||_F^2 \; s.t. \; \tilde{\mathcal{X}} = (A, B, C), A^T A \; = \; I, \; C \geq 0 \tag{5.3}$$

Note that each sub-problem (for A, B and C) can be solved optimally using generalized solution to the orthogonal procrustes problem [200], generalized least square solution [201] and non-negative least squares solution [202], respectively.

This constrained-PARAFAC decomposition was proposed in [122] for extracting the *static* functional activation maps from raw fMRI data. In contrast, this chapter utilizes the decomposition model for extracting *dynamic* spatial couplings that vary over time and uses the distinct subject-wise loading vectors to associate and predict gender (respectively, intelligence) from both t-fMRI and rs-fMRI. Here we note that, although the proposed tensor decomposition has straight forward interpretations for t-fMRI since all subjects perform pre-scheduled tasks, resting-state fMRI is not synchronized between subjects. However, during rest, fMRI scans have shown synchronization among regions of brain in humans. This is especially true for default mode network (DMN) [7] in brain. Recently, trilinear tensor factorization was also applied explicitly to rs-fMRI in [167,203]. We explored the predictive performance of the same technique as an exploratory measure for rs-fMRI as well to predict biological traits. The model performance showed that straight forward application of constrained-PARAFAC tensor decomposition is useful for rs-fMRI for classification of biological gender and prediction of intelligence.

Uniqueness

Uniqueness conditions for the proposed model are derived in the following two theorems.

5.2.5 Theorem 1.

Consider $\mathcal{X} \in \mathcal{R}^{I_1 \times I_2 \times I_3}$. Let $A \in \mathcal{R}^{I_1 \times F}, B \in \mathcal{R}^{I_2 \times F}, C \in \mathcal{R}^{I_3 \times F}$ represent the tensor decomposition matrices such that $C \geq 0$ and $A^T A = I$. In this case a global minimum

for (6.2.3) exists. In other words, there is only one solution for $\tilde{X}$ that minimizes (6.2.3).

Proof. We prove this theorem following Proposition 3.1 of [204]. Note that (6.2.3) can be written in unfolded format as follows,

$$\min_{A,B,C} ||X_2 - (A \odot C)B^T||_F^2 \;\; s.t.\; A^T A \;=\; I,\; C \geq 0 \tag{5.4}$$

Let us denote, $f(A, B, C) = ||X_2 - (A \odot C)B^T||$. Solving (6.2.3) is equivalent to finding the minimum for $f(A, B, C)$. Since $A^T A = I$, $(A \odot C)^T (A \odot C) = I$. Thus solving for B, $B^T = [(C \odot A)^T X_2]$. Substituting B^T into (5.4) yields,

$$g(A, C) = ||X_2 - (A \odot C)(A \odot C)^T X_2||_F^2 \tag{5.5}$$

Note that $A^T A = I$ and $C \geq 0$. In addition, g is continuous and the domain of g is compact (as the domain of A, B are continuous and compact). Thus the global minimum exists for g. As a result, f has a global minimum. ■

5.2.6 Theorem 2.

If conditions *I* and *II* are satisfied, then the decomposition $\tilde{X} = (A, B, C)$ is unique up to permutation and scaling.

Proof. This can be proved by closely following the proof for the unrestricted case as given in [198]. The only difference is the relaxation of restriction on the columns of C in our case. Note that the restrictions on columns for A to be a full column rank is fully satisfied by the fact that $A^T A = I$

Let $BC = (B \odot C)$. Conditions *I* and *II* imply that the non-trivial combination of BC can not be written as represented as tensor product of two vectors which satisfies the necessary and sufficient conditions of [198]. ■

Algorithm for Solving the Problem

An algorithm for finding the solution of (6.2.3) is given in Algorithm 5.

5.2.7 Theorem 3.

Algorithm 5 finds the uniquely identifiable decomposition of (6.2.3).

Algorithm 5: Alternating Least Square Algorithm for Solving Constrained PARAFAC in (6.2.3)

Input : Tensor $\mathcal{X}$, rank F

Output: Estimated connectivity maps A, time courses B, subject-wise contribution C

(X_1, X_2, X_3) = Unfold $\mathcal{X}$ along axis 1, 2, 3 respectively.

Initialize A, B, C

for $i = 1$ **to** *until convergence* **do**

  `% Solve for A from unfolding` X_1

  $M = [(B \odot C)^T X_1]$

  $M = U\Sigma V^T$

  $A^T = UV^T$

  `% Solve for B from unfolding` X_2

  $B^T = [(C \odot A)^T X_2]$

  `% Solve for C from unfolding` X_3

  $N = (A \odot B)^T X_3$

  $C^T = [N_+]$ where N_+ contains only the positive elements of N

end

Proof. The Lagrangian for (6.2.3) can be written as

$$L(A, B, C, \Lambda_1, \Lambda_2) = ||X_2 - (A \odot C)B^T||_F^2 + Tr(\Lambda_1(A^T A - I)) + Tr(\Lambda_2(-C))$$

The domain set of A, B and C are in $R^{I_1 \times F}, R^{I_2 \times F}$ and $R^{I_3 \times F}$, respectively and hence they are convex set. Note that every update in Algorithm 5 is an optimal update for each sub-problem. Using proposition 2.7.1 of [205], (A^*, B^*, C^*) is a stationary point.

For the unconstrained PARAFAC decomposition, there does not exist any proof of convergence, which may not converge, or converge to a local minimum [206]. However, there exists research that describes global convergence for block-nonlinear alternating least square under convex constraints. As the function $||X_2 - (A \odot C)B^T||_F^2$ is quasi-convex on $R^{I_1 \times F} \times R^{I_2 \times F} \times R^{I_3 \times F}$, according to Proposition 5 of [207],(A^*, B^*, C^*) is a critical point of (6.2.3). From Theorem 1, (A^*, B^*, C^*) finds the uniquely identifiable

decomposition of (6.2.3). ■.

Table 5.1: Demographic and task score information for the subjects.

Demographic Information	Male	Female	Range
# of samples (n)	196	279	-
Age − mean (SD)	29.30 (3.31)	29.23 (3.48)	22-36
Task Score Information	**Male**	**Female**	**Range**
Fluid Intelligence - mean (SD)	16.56 (5.21)	15.76 (5.13)	4-24
Fluid Ability Metrics - mean (SD)	99.50 (16.35)	101.85 (16.14)	47-150

5.3 Experimental Setup

5.3.1 Dataset

The dataset used in the analysis is taken from Q2 release of Human Connectome Project database [29,34]. The dataset consisting of 475 subjects is used to classify gender (male vs. female) and predict intelligence of the subject. The subjects in the database were scanned while they performed the following seven tasks i) emotion, ii) gambling, iii) working memory, iv) relational, v) language, vi) motor, vii) social. Additionally rs-fMRI was also captured.

Biological Gender

Number of females 279, number of males 196.

Intelligence

Following [29], two relevant behavioral tasks were chosen as metrics of intelligence [182] quotient. Table 5.1 provides the the age and task scores along with the range of score values. There were no significant differences ($p > 0.05$) between males and females with respect to the scores.

- *Fluid Intelligence.* Fluid intelligence was measured using the Penn's Progressive Matrices (PMAT) [208]. PMAT is a shortened version of Raven's Progressive

Matrices. In this test, the participants were given puzzles that contained visual patterns. In the puzzles, a piece was missing and they were asked to fill the blank piece from a number of candidate pieces.

- *Fluid Ability Metrics.* The Pattern Comparison Processing Test is a measure of speed of processing, which is considered a 'fluid ability' because it steadily improves from childhood to adolescence, and then begins to decline in adulthood (Range 47-150). This test for ages 7-85 asks participants to identify if the two pictures shown in the screen are same. The age-adjusted scale score was used for our experiment. Participant score was normalized using the age appropriate band of Toolbox Norming Sample (bands of ages 18-29, or 30-35). A score of 100 signifies performance that is same as national average, whereas 1 standard deviation away score is equivalent to increase or decrease of 15 points.

5.3.2 Data Acquisition and Preprocessing

The fMRI dataset consisted of 475 subjects taken from Human Connectome Project database [29,34]. All the tasks and resting state data were used. The fMRI data can be publicly accessed from [1] . Functional magnetic resonance imaging data were acquired using a customized Siemens 3T Connectome Skyra scanner. The scans were taken using 2 mm isotropic voxels with TR = 720ms, TE = 33.1 ms as described in [20]. Details of the task paradigms can be found in WU-Minn HCP 500 Subjects Data Release Manual available from [2] .

The HCP fMRI data was first processed following the HCP "fMRI Volume" pipeline (v3.4), which includes gradient unwrapping, motion/distortion correction, registration to structural scan, nonlinear registration into MNI152 space, and intensity normalization as reported in [10]. Subsequently, spatial smoothing and activation maps generation using the generalized linear model implemented in FSL's FILM (FMRIB's Improved Linear Model with autocorrelation) were performed. Using Freesurfer cortical parcellation atlas [54], 85 regions of interest were identified as shown in Table A.5 in Supplementary Information. Mean time-series values of voxels in every region for each subject were

[1] `https://db.humanconnectome.org`
[2] `https://www.humanconnectome.org/`

then extracted. For *static* connectivity analysis, one-shot absolute Pearson's correlation values are extracted for each subject from the mean time-series.

The time-series for each subjects were then divided into multiple sliding windows of varying strides $(1, 5, 10, 15)$. The window size were kept fixed at 50s following the recommendations from [209]. Absolute Pearson's correlation were calculated for each subject and each time window between the 85 regions. Note that the correlation coefficient values are bidirectional. Hence only one set of values for each pair of regions were kept and thus we get $\binom{85}{2} = 3570$ edge correlation values (or vector of size 3570×1) for each window. Correlation vectors extracted from different time-windows were stacked to form a *dynamic* functional connectivity matrix (size $3570 \times T$ where T depends on the sliding window stride). *Dynamic* functional connectivity matrix were then concatenated to form a 3 dimensional tensor of size $3570 \times T \times 475$. A workflow diagram for the proposed prediction scheme is given in Fig. 5.2.

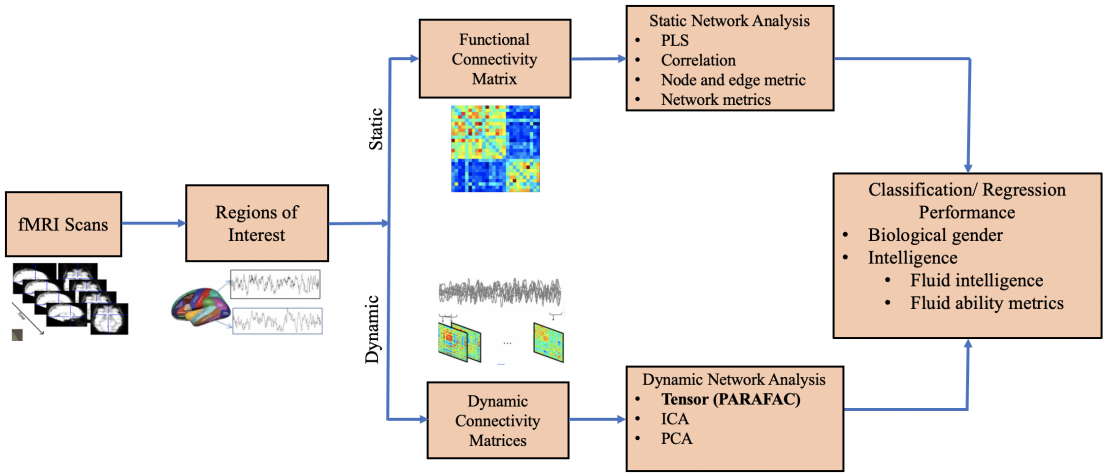

Figure 5.2: The workflow for proposed classification/ regression framework. *Static* and *dynamic* connectivity matrices are extracted from brain regions. The features extracted from these matrices are used to predict biological gender and intelligence.

5.3.3 Performance Comparison

We compare the performance of proposed dFC against the following baseline methods:

Partial Least Squares (PLS) [187]: Partial least squares method is useful for

associating neuroimaging markers with behavior. PLS finds a new projection of the response variables and independent variables into a new common space. PLS was run on the *static* correlation matrix extracted for the group of subjects for classification and prediction. The number of components for PLS were chosen based on cross-validation performance.

Correlation Coefficients [210]: Raw values of correlation coefficients were used as features for classification and prediction scheme. However, the number of features is very large compared to number of samples (475) and hence there is a chance of reduced prediction power for curse of dimensionality. As a result, feature selection becomes important for prediction task [180]. Feature selection was implemented using Minimum Redundancy Maximum Relevance (mRMR) [139].

Network Features [22]: Adjacency matrices were used to calculate network characteristics using *Brain Connectivity Toolbox* (BCT) [3] as described in [25]. At a local (node) level in the network, three features, namely *local efficiency (LE), clustering coefficient (CC)* and *betweenness centrality (BC)*, were computed [60,61]. At a global level, we calculated two features: *modularity* and *global efficiency* [60]. The local and global features in the network represent complementary viewpoints of the network for *segregation* and *integration* of nodes, respectively. Hence from each subject, we extracted $85 \times 3 \times 2$ (for 3 features at each node) $+ 2 \times 2$ (for *modularity and global efficiency*) $=$ 514 network features.

An overview of the network based features is discussed next as described in [134]. *Local efficiency* is computed using the summation of inverse of the shortest paths to the neighbors of a node. This metric is used to understand how efficient a node is for transferring information between two neighboring nodes. *Clustering coefficient* is calculated by the number of triangles created around a node out of all possible triangles. *Betweenness centrality* of a node is calculated as the percentage of shortest paths that contain the node. *Modularity* metric measures how a network is sub-divided into smaller dense sub-networks with sparse inter-connections. *Global efficiency* describes the efficiency of information transfer within the whole graph. More details of the network measures can be found in [22].

Sub-Graph Entropy [20]: We have recently shown that sub-graph entropy metrics

[3] `https://sites.google.com/site/bctnet/`

are well suited for identifying brain states [20] and classifying patients suffering from metal disorders [25]. From *static* one-shot connectivity matrix, node entropy and edge entropy were calculated and they were used for further analysis.

Principal Component Analysis (PCA) [199]: Principal Component Analysis was carried out on the concatenated correlation values from sliding window for all subjects. This procedure extracted common network space and unique time-courses for each subject that are orthonormal to each other. The average value of unique time-courses were used as features for prediction. The number of components for PCA were chosen based on cross-validation performance.

Independent Component Analysis (ICA) [178]: Independent Component Analysis is a popular method for analysis dFC. In our experiments, ICA was also carried out on the concatenated correlation values from sliding window for all subjects. Like PCA, this analysis extracted common network space and unique time-courses for each subject that are independent of each other in statistical sense. The average value of unique time-courses were used as features for prediction. The number of components for ICA were chosen based on cross-validation performance.

Mean dFC: For comparison to existing sliding window approach, average absolute Pearson correlation value for all the sliding window correlation matrices were calculated for each subject. This average edge weights of size 3570×1 is then used directly for classification (respectively, regression).

5.3.4 Statistical Analysis

We divided the dataset randomly into 5 unique sets that were later used for 5-fold cross-validation. For each of the tasks, 5-fold cross validation (CV) [211] was performed over the dataset, where 4 folds are used for training each time and the rest for testing with hyper-parameters chosen using in-fold validation. In this chapter, we reported the CV accuracy as well as other performance measures such as sensitivity and specificity. For intelligence prediction, we reported normalized mean square error (MSE) as well as mean absolute error (MAE) and standard deviation of error (SD). Normalized mean square error was calculated by dividing the mean square error by the square of actual values. For all the prediction performance random forest classifier (respectively, regressor) was employed. For hyperparamter tuning, a standard set of number

of trees $\{2^i | i = 1, .., 7\}$ was followed using in-fold cross-validation. We used the inbuilt implementation of random forest available in MATLAB [4] .

Additionally, t-tests were carried out to find out the connectivity maps that have statistically different loading in male *vs.* female. Similarly, Pearson's correlation test was performed to extract the connectivity components with statistically *higher* correlation values with fluid intelligence and fluid ability metrics. Note that, in both cases, the subject-wise loadings (columns of C) of the components were used for finding the statistical significance. As the test involves multiple comparisons for multiple components, the significance level (α) for rejecting the *null* hypothesis that there was no significant difference (classification task/ biological gender identification) or there was no significant correlation (regression/IQ prediction task), was fixed at 0.05 with Bonferroni correction.

5.4 Results

5.4.1 Classification Results

The results for classifying biological gender and prediction of IQ are described next.

All features were able to classify gender with high accuracy. The results for using six distinct methods as described above are shown in Fig. 5.3. We note that the proposed dFC (tensor) turns out to be one of the two best performing features (other one is edge entropy). For individual performances in each task, features extracted from *emotion* task had the best performance for classifying male *vs.* female with accuracy, sensitivity and specificity of 0.84, 0.89 and 0.81, respectively. This was closely followed by rs-fMRI. The results of the performance for each type of features are shown in Table. 5.2.

Overall, dFC extracted from the concatenation of tasks together performed the best in classifying biological gender. In order to understand which *stride* for calculating dFC performs the best for classifying gender, we tested the classification scheme for *stride* $= 1, 5, 10, 15$. The winning *stride* is chosen for the *"final"* classifier. The results are shown in Fig. 5.4. In particular, *stride* $= 10$ had best overall performance for each task where it classified biological gender most precisely for 7 out of 8 tasks.

Finally, the best performance for each class of features is shown in Table 5.2.

[4] `www.mathworks.com`

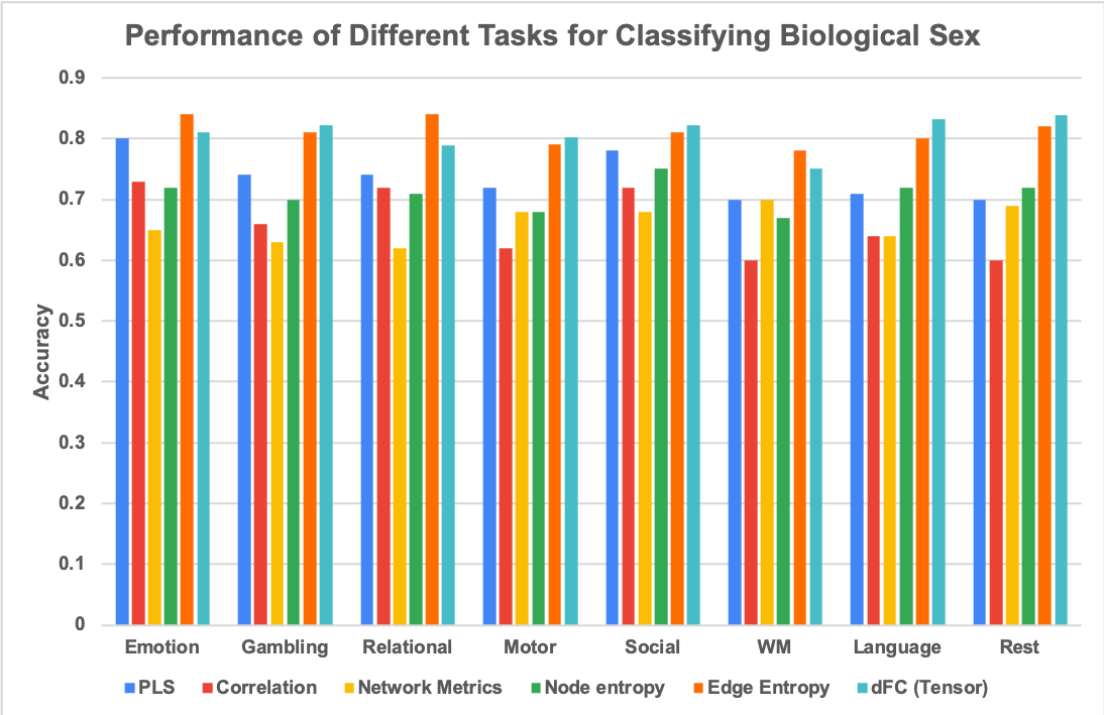

Figure 5.3: Average 5-fold cross-validation accuracy for each task employing different feature engineering techniques. Here more the height of the bar, better the performance. The accuracy performance for different features in Table 5.2 are shown for each task. Our proposed dFC (Tensor) always performs within top two methods for predicting biological gender.

The proposed method for classifying biological gender was compared with other ways of calculating dFC and the results are shown in Table 5.3.

Fluid intelligence and Fluid ability metrics were predicted in the same way. Figs. 5.5 and C.1 in Appendix C demonstrate the results of using *static* and *dynamic* network based features for predicting fluid intelligence and fluid ability metrics, respectively. For fluid intelligence, the mean absolute error were in the range of $5 - 6$ for all the methods. Note that, among the tasks, working memory task was most predictive of fluid intelligence as it gave the task wise best performance for 2 out of 5 *static* connectivity features as shown in Table 5.4 followed by emotion task. However, combining the tasks together and applying the proposed tensor decomposition yielded the best prediction

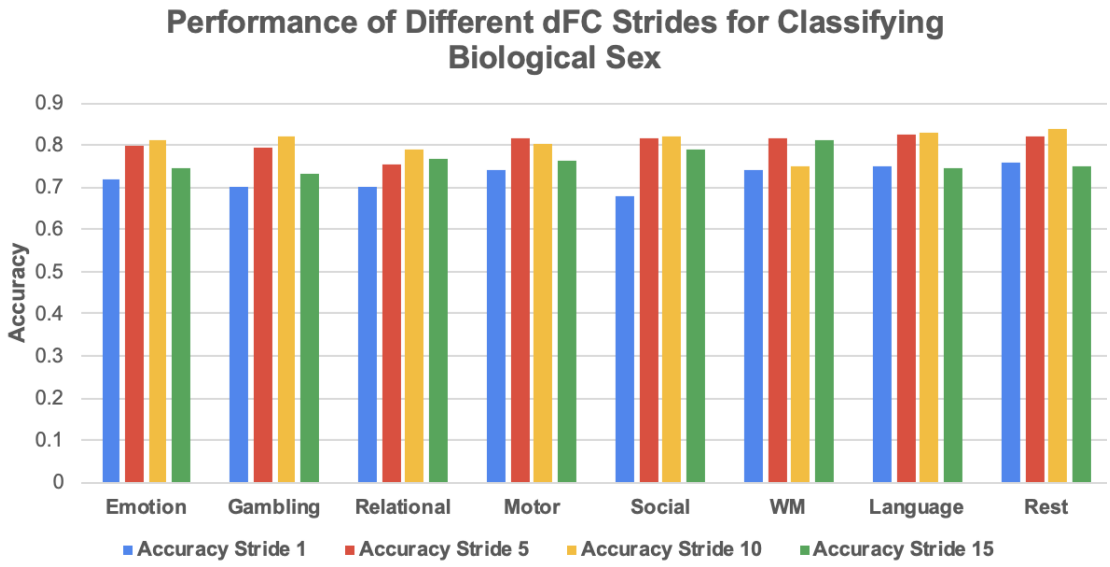

Figure 5.4: Average 5-fold cross-validation accuracy for each task employing different sliding window strides for calculating dFC. Here more the height of the bar, better the performance. Stride 10 yields best accuracy most of the times.

performance with MSE, MAE of 0.13 and 5.1, respectively.

For fluid ability metrics, the mean absolute error were in the range of $13 - 16$ for all the methods. No task had a consistently good performance across all *static* connectivity features as shown in Table 5.4. Combining the tasks together and applying the proposed tensor decomposition yielded the best prediction performance with MSE, MAE of 0.031 and 15.37, respectively.

Additionally, Figs. 5.6 and C.2 in Appendix C show the prediction results for dFC with different sliding window strides. For fluid intelligence prediction, stride = 5 performed the best whereas for fluid ability metrics stride = 10 had the best performance.

Similar to the case of gender prediction, the winning model from each types of features and task is listed in Table 5.4.

The proposed method was also compared with other ways of calculating dFC (PCA, ICA) and the results are shown in Table 5.5. The dFC based features were able to predict 27% of the variations for fluid intelligence and 22% of variations for fluid ability metrics. Both of these values are higher than that reported in [192].

Table 5.2: 5-Fold cross validation classification results for biological gender classification

	Task	Features	Accuracy	Sensitivity	Specificity
Partial Least Square [187]	Emotion	15	0.80	0.66	0.86
Correlation [210]	Emotion	15	0.73	0.64	0.75
Network Features [22]	Rest	54	0.69	0.74	0.65
Node Entropy [20]	Social	85	0.75	0.83	0.66
Edge Entropy [20]	Emotion	3570	0.84	0.89	0.81
Dynamic Connectivity (Proposed)	Combined	25	**0.94**	**0.97**	**0.87**

Table 5.3: 5-Fold cross validation classification results for biological gender classification using different decomposition techniques from dFC.

	Task	Features	Accuracy	Sensitivity	Specificity
Tensor (Proposed)	Combined	25	**0.94**	**0.97**	**0.87**
ICA [173]	Combined	75	0.71	0.55	0.85
PCA [199]	Combined	75	0.5	0.48	0.51
Mean dFC	Emotion	3570	0.74	0.85	0.66

To check the robustness of our results from dFC, we carried out the classification scheme using a different brain atlas based on functional organization [212]. The results on gender classification, and intelligence predictions are reported in Tables C.1 and C.2 (Appendix C). The results are always within $\sim 2\%$ of the performances compared to the anatomical brain parcellations.

5.4.2 Important Networks

The dFC component maps extracted by combining sliding window correlation values across tasks were highly predictive of biological gender, and individual intelligence metrics. In order to understand if the extracted maps were loaded in significantly different ways in male *vs.* female groups, we performed t-test on the individual weight matrix (C) of the decomposed tensor. Note that column of C correspond to loading of spatio-temporal components and the rows of C represent individual variations of different components. Hence t-tests were carried out separately on each column of C based

Table 5.4: 5-Fold cross validation regression results for predicting IQ.

	Fluid Intelligence					Fluid Ability Metrics				
	Task	Features	MSE	MAE	SD	Task	Features	MSE	MAE	SD
Partial Least Square [187]	Emotion	15	0.58	11.42	2	Language	15	0.70	82.71	4.57
Correlation [210]	Motor	15	0.15	5.36	4.3	Relational	15	0.044	16.78	0.86
Network Features [22]	WM	425	0.15	5.35	0.33	Rest	425	0.045	17.03	3.43
Node Entropy [20]	Emotion	85	0.16	5.62	0.36	Emotion	85	0.037	15.85	1.05
Edge Entropy [20]	WM	3570	0.147	5.17	0.36	Motor	3570	0.041	15.38	0.64
Dynamic Connectivity (Proposed)	Combined	25	**0.139**	**5.1**	0.2	Combined	25	**0.031**	**15.37**	1.01

Table 5.5: 5-Fold cross validation regression results for predicting IQ using different decomposition techniques from dFC.

	Fluid Intelligence					Fluid Ability Metrics				
	Task	Features	MSE	MAE	SD	Task	Features	MSE	MAE	SD
Tensor (Proposed)	Combined	25	**0.139**	**5.1**	0.2	Combined	25	**0.031**	**15.37**	1.01
ICA [178]	Combined	75	0.453	10.31	3	Combined	75	0.043	18.01	2
PCA [199]	Combined	75	0.516	11.34	4.2	Combined	75	0.087	31.49	5
Mean dFC	Motor	3570	0.169	5.80	0.13	Relational	3570	0.034	15.67	1.43

on biological gender labels. Two components were found to be statistically different ($p < 0.002$) after Bonferroni correction of significance level. In order to visualize the component, the edges with values in the top 5% are visualized by overlaying them on an MNI brain using BrainNet toolbox [55]. The components are illustrated in Fig. 5.7. We see that the corresponding weights are well distributed among the subjects, which signifies that this component was prevalent in most people in the group. In particular, Spatial Map 1 in Fig. 5.7 has higher weights for females compared with males. On the other hand, Spatial Map 2 in Fig. 5.7 has higher weights for males compared with females.

To infer about the important states in the case of intelligence metrics, Pearson's correlation test is carried out on the column of C corresponding to each spato-temporal map. In each case, there were multiple components that had $p < 0.05$, however the number of components that passed Bonferroni correction were 3 and 2 for fluid intelligence and fluid ability metrics, respectively. In both cases, two components with lowest p-values are shown in Fig. 5.8 and C.3 in Appendix C, respectively. In order to visualize the component, the edges with values in the top 5% are visualized by overlaying them

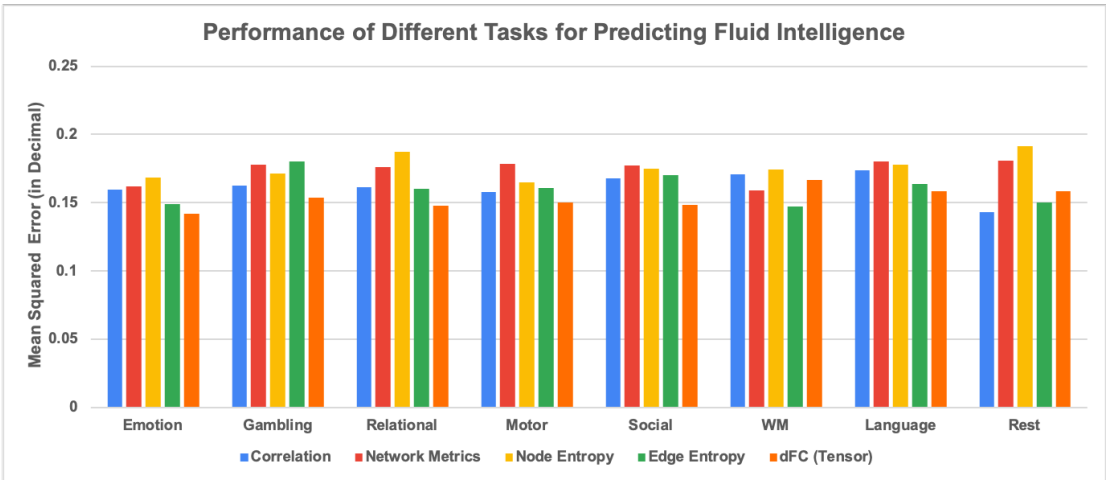

Figure 5.5: Average 5-fold cross-validation normalized mean square error for each task employing different feature engineering techniques to predict fluid intelligence. The normalized mean square error performance for different features in Table 5.4 are shown for each task. Here less the height of the bar, better the performance. Our proposed dFC (Tensor) always performs within top two methods for predicting biological gender.

on an MNI brain using BrainNet toolbox [55]. For fluid intelligence, we see that the corresponding weights are well distributed among the subjects, which signifies that this component was prevalent in most people in the group. In particular, Spatial Map 1 and Spatial Map 2 in Fig. 5.8 have $p = 0.0012$ and $p = 0.0063$, respectively with the fluid intelligence metric. However, for fluid ability, the corresponding weights have longer tail towards the lower range values and hence are not well distributed among the subjects. In particular, Spatial Map 1 has a negative correlation with $p = 0.0003$ and Spatial Map 2 has a positive correlation with $p = 0.0006$ with the fluid ability metric.

5.5 Discussion

In this chapter, we presented a novel method for extracting *dynamic* functional connectivity using constrained-PARAFAC decomposition technique. Conditions for uniqueness were derived and an algorithm utilizing alternative least squares was provided to find out the unique spatio-temporal decomposition. Tensor based dFC approach was able

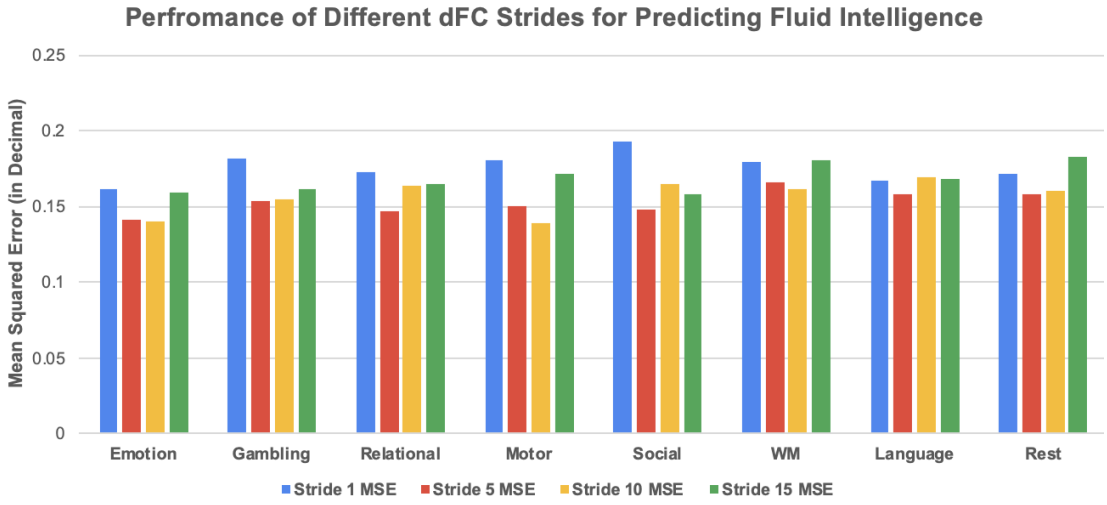

Figure 5.6: Average 5-fold cross-validation normalized mean square error to predict fluid intelligence for each task employing different sliding window strides for calculating dFC. Here less the height of the bar, better the performance. Stride 5 yields best accuracy most of the times.

to predict biological gender with high accuracy and intelligence with low prediction error compared with traditional *static* and *dynamic* function connectivity based features. We also extracted the *dynamic* network maps that are associated with gender and IQ through tensor decomposition. Key observations of biological significance relative to the existing literature are described next.

5.5.1 Gender effect on dFC

Although, biological gender has a large impact in *static* and *dynamic* brain connectivity, there are differences in scientific conclusions regarding their effects. Several connectivity studies have reported the apparent connectivity differences. The spatial map (spatial map 1) extracted from our analysis implicated regions from prefrontal cortex, precuneus and posterior cingulate cortex (PCC) that had higher connectivity in females which are similar to that reported in the previous study in [188]. Previously, in the graph theory based analysis in [210], males showed significantly higher network connections in the right hemisphere compared to females and lower left hemispheric connections compared

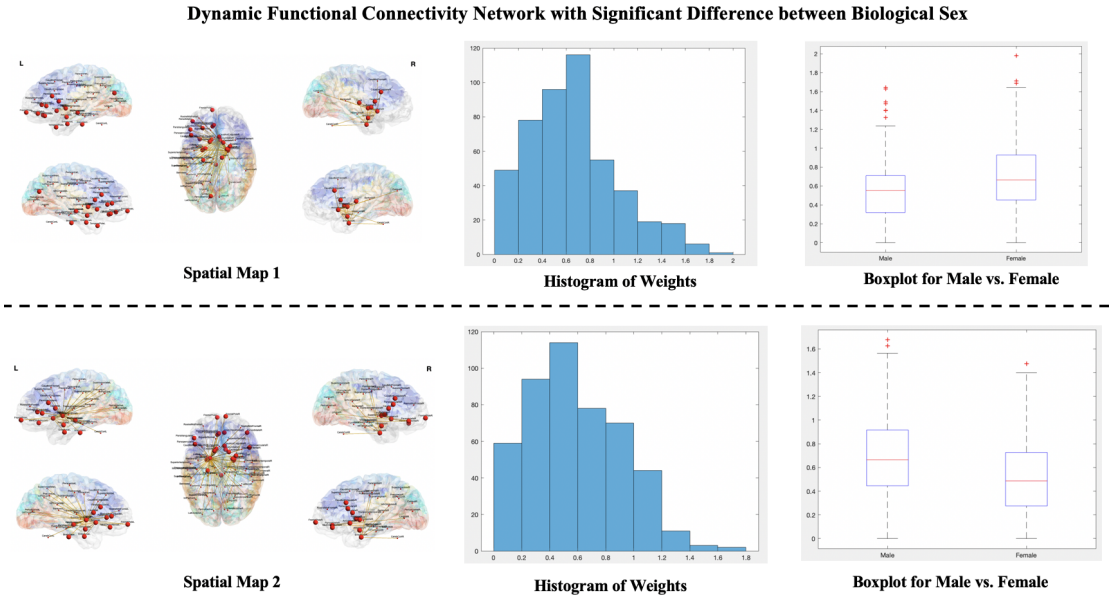

Figure 5.7: Statistically significant spatial components along with the weight distributions for differentiating male *vs.* female. *Left*: Spatial map with top 5% connectivity values. *Middle*: histogram of the weight loading for all subjects. Most of the subjects have non-zero values for weights signifying that this map is present in the majority. *Right*: box-plot of the individual weights values for different biological gender groups.

to female group. Spatial map 1 seems to also suggest that female brain has higher functional connections to the regions in the left hemisphere. However, the connections are mainly inter-hemispherical, *i.e.,* the connections criss-cross across the central gyrus. This is also supported from anatomical connectivity literature [190]. Number of left brain regions with high functional connections is more for females compared with male. But they are mainly connected to regions in the other hemisphere. Here the component had significantly higher prevalence in females compared with males. In our work, within hemisphere connectivity is noted in spatial map 2. Here the component had significantly higher prevalence in males compared with females.

The study performed by [189] carried out statistical comparison of *static* network connectivity metrics between biological gender groups using ICA. The spatial maps

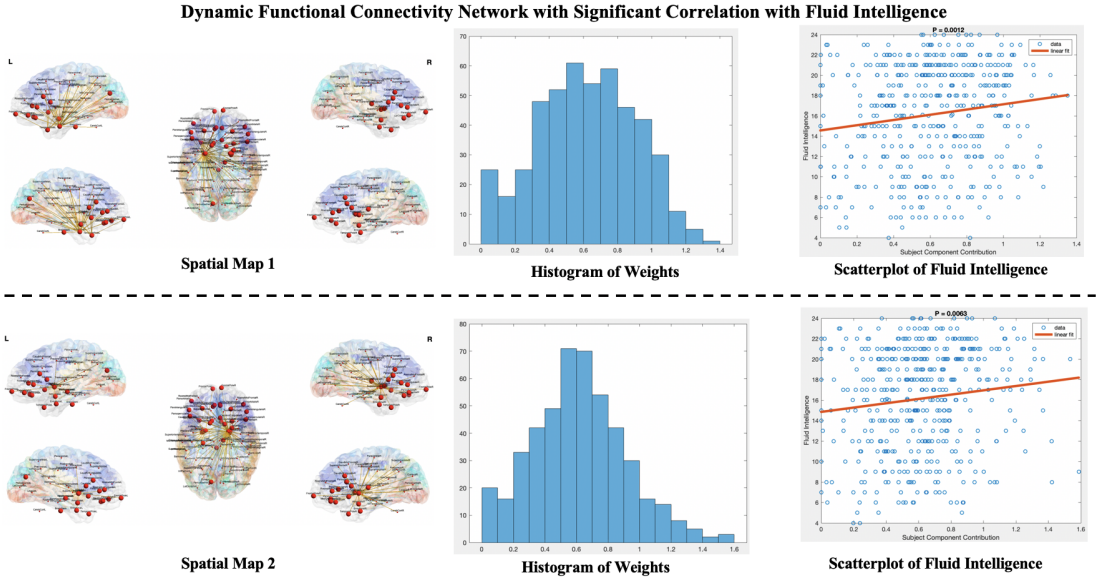

Figure 5.8: Statistically significant spatial components along with the weight distributions for correlating with fluid intelligence. *Left*: Spatial map with top 5% connectivity values, *Middle*: histogram of the weight loading for all subjects. Most of the subjects have non-zero values for weights signifying that this network is present in the majority. *Right*: scatter plot with correlation curve and corresponding p-values for individual weights.

found in sensorimotor, salience, attention and auditory regions showed statistically significant changes in network measures. Spatial map 2 in our analysis has a hub region in temporal lobe in the left hemisphere. The associated functional connectivity may indicate more involvement of auditory networks in most behavioral tasks more for males. For Spatial map 1, well-connected regions involve pre-central and post-central regions in left hemisphere which is part of sensorimotor network whereas for spatial map 2, the regions are sparsely connected. Thus sensorimotor networks have higher inter-hemispherical connections in female whereas they have somewhat reduced inter- and intra-hemisphereical connections in males. Moreover, in our results, the predictive sub-network contains regions from salience network (hippocampus) and regions from striatum. It also contains the hippocampus which is part of salience network [25].

Dynamic functional connectivity has been shown to predict biological gender accurately in [176] (accuracy 0.80). Our proposed method employed a constrained-tensor decomposition process to extract subject dependent features which improved leave-one-out accuracy to 0.94 using dFC. Consistent with Menon et al. [176] we note that both spatial maps that had significant statistical differences involved regions from fronto-parietal and attention network (precuneus). Similarly, the spatial maps contained lateral occipital node that is part of visual network [177] in the brain. Despite these findings, more experiments need to be performed for better understanding of biological gender effect on dFC.

5.5.2 IQ affect on dFC

There has been progress in our understanding of intelligence and its associated neural correlates using newer MRI techniques. Recent works have reported the relation between an individual's intelligence metrics and thickness in gray matter [213], white matter [214], and cortical thickness [215]. Our method extracted regions from distributed regions in brain that are correlated with intelligence metrics as shown in Figs. 5.8 and C.3 in Appendix C. This was also supported in previous works on functional connectivity (FC) [216,217]. In addition, the connectivity maps with most functional edges for fluid intelligence belong to the frontal-parietal circuit and default mode networks in the brain that was also supported in [182, 218]. Moreover, In our results, the predictive sub-network contains regions from salience network (hippocampus) and regions from striatum. Interestingly, the two significant spatial maps for fluid intelligence contain regions from different hemispheres separately (and for both cases the correlation is positive), which reinforces that fluid intelligence is a product of distributed intra-hemispheric communication. A thorough investigation using network neuroscience has confirmed that general intelligence can be associated with small world characteristics of the brain that has the potential to assert more cognitive flexibility [219] in addition to the adaptability to the information processing. However, for fluid ability metrics, spatial map 1 consisted of fronto-parietal functional networks in the left hemisphere that has negative correlation with the score. The inter-hemispheric functional connectivity for spatial map 2 in Fig. C.3 in Appendix C may indicate that the increase in inter-hemispheric functional edges improve the fluid ability metrics.

5.6 Conclusion and Future Work

This chapter has demonstrated that dFC of the human brain can contribute substantially towards forming a fingerprint of biological gender and intelligence. In addition, we proposed a fully cross-validated scheme for the individual characteristic prediction. The statistically different sub-network of interest between two groups is extracted and their connection to the existing literature is drawn. Moreover, significant networks are extracted that have significantly high correlation with intelligence metrics. Future work will be directed to the lesson learned from this work to develop and plan group-specific (based on gender, IQ etc.) therapies for patients suffering from psychiatric disorders. Additionally, we will investigate the constrained tensor decompositions of *dynamic* functional connectivity for rs-fMRI where strict trilinearity is not required in the time domain (dim = 2). Accurately inferred spatio-temporal signal and connectivity maps from different groups can also be used to compare differences among other types of sub-groups in the population, *e.g.,* age groups, language groups, and other types of behavioral tasks.

Chapter 6

Classification of Adolescent Major Depressive Disorder via Static and Dynamic Connectivity

6.1 Introduction

Major-depressive disorder (MDD) is a debilitating neuro-psychiatric illness that impacts all aspects of patient's lives. This disorder is generally characterized by thoughts or behaviors that make the patients feel sorrowful, isolated and fearful. It impacts about 322 million people's lives worldwide [220]. Depression is prevalent in a large proportion of general population, however, for patients suffering from MDD, the symptoms of depression are very persistent and critical. Although MDD is a serious life threatening psychiatric disease, experts have disagreements regarding the functional alterations of brain regions during the course of MDD. Among the different age groups of population vulnerable to MDD, adolescents constitute a major subgroup. The current diagnostic process for adolescent MDD involves a subjective understanding of the patient which includes behavioral examinations, symptom ratings and interviews with parents [119]. An artificial intelligence (AI) assisted clinical diagnostic tool based on functional magnetic resonance imaging has the potential to assist a clinician diagnose MDD directly using brain scans.

This chapter develops a machine learning based diagnostic tool (classifier) to discriminate and identify adolescents suffering from MDD from typical healthy developing adolescents. The classifier learns prediction rules based on resting-state functional magnetic resonance imaging (fMRI)-based attributes of subjects. Identifying patients-specific features for classifying adolescent MDD is a very important step, as if left without proper treatment, the subjects may have atypical neuronal development. However, how the resting-state brain functional network changes among adolescents with MDD remains unknown. Thus finding specific markers associated with MDD is of significant interest.

Concurrent fMRI based psychiatric research has shown that fMRI can be used to diagnose different neuronal disorders [25, 61, 120, 221]. Functional magnetic resonance imaging provides an in-vivo measurement of brain activity during resting-state (rs-fMRI) or task (t-fMRI). Specifically, fMRI measures the change of blood-oxygen level dependent (BOLD) signal, when a person is scanned. This produces a 4-D activation image of brain function, where the first three dimensions show the *spatial* brain structure and the fourth dimension shows the change of activation over time [25, 122]. The time component of fMRI scans can be utilized to extract correlation based functional connectivity of brain regions. When a person is awake in rest condition, some regions in the brain are always activated (default mode network). For rs-fMRI, the spontaneous regional interaction between brain regions are measured. Resting state fMRI signal have been hypothesized to be meaningful for understanding psychiatric patients as the hemodynamic response is not confounded by any task response [7]. The current chapter considers only the analysis of rs-fMRI for adolescent MDD patients and typically developing adolescents.

The goal of this chapter is to classify adolescent MDD patients from healthy controls accurately. In this process, we extract a brain sub-network from rs-fMRI that has good classification performance for identifying adolescent MDD *vs.* healthy controls. We use absolute correlation coefficients, graph-theoretic properties of functional network, and *dynamic* connectivity properties of human brain for classifying MDD and healthy controls. First we use *bivariate* and *multivariate* features for predicting MDD. Second, network measures using *sub-graph* entropy [20] and specifically differential node entropy and edge entropy are used to extract most important regions and edges impacted in adolescent MDD. Edge entropy is then used to extract a sub-network containing 105

edges. Finally, a *joint* connectivity approach combining features from *static* and *dynamic* connections leads to a high classification accuracy for MDD *vs*. healthy.

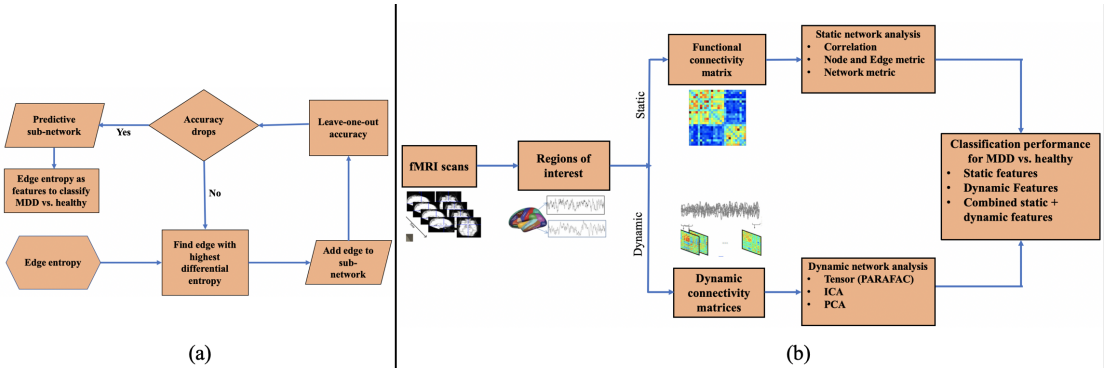

Figure 6.1: (a) Procedure for extracting a predictive sub-network for MDD *vs*. healthy. Edges with highest *differential entropy* are selected to identify the sub-network based on leave-one-out accuracy. The sub-network's *sub-graph* entropy is compared between two groups using t-test for validation. (b) MDD classification pipeline using *static* and *dynamic* features.

6.1.1 Related Work

Recent advancements in machine learning in neuroimaging has unraveled the relationship between computer aided designs and psychiatry. Furthermore, advances in complex network theory, blind source separation have also permeated neuroimaging and psychiatry. In a complex network, different measures can be used to find the important nodes [20, 39]. These metrics denote the cohesiveness or segregation among different nodes. Network *segregation* refers to the *local* characteristics at each node, *i.e.*, how a particular node is affected by the interaction with its neighbors. Network *integration* refers to the large-scale behavior of the whole graph (*global* characteristics). In particular, *local efficiency (LE)* [21], [5], *clustering coefficient (CE)* [22] and *betweenness centrality (BC)* [23] measures are examples of local network *segregation*. Global integration can be specified in terms of *global efficiency (GE)* [21] and *modularity* [24]. An important network metric defines important nodes to be those having the highest number of neighbors. This *metric* is known as degree centrality [41]. A more complex *metric* using *information-theoretic* network measures [51, 53] was used in [52] to extract

leaders and followers from a directed communication network. Mackenzie [51] showed that *information-theoretic* importance can be used as centrality in a communication network. An *information-theoretic* network *segregation metric*, referred as *sub-graph* entropy [20], has been shown to be useful for classifying brain *states*.

Some of the above measures were used previously for comparing characteristics between two groups (*e.g.*, schizophrenia *vs.* healthy [120, 124], Alzheimer's disorder *vs.* healthy [123, 125], bordeline personality disorder *vs.* healthy [61], and obsessive compulsive disorder *vs.* healthy [25, 126]). Hypothesis driven association studies can extract statistically significant functional neural correlates for psychiatric disorder. In the current chapter, we propose a combined *static* and *dynamic* connectivity approach to predict whether an adolescent has MDD. Using tools from communication and network information theory and tensor analysis, we show that a network measure called *sub-graph* entropy (node and edge entropy) introduced in our recent paper [20] and constrained prallel factor analysis (PARAFAC) [122] can perform this task with high accuracy. Additionally, node and edge entropy were used to rank brain regions and edges, respectively. The important predictive sub-network extracted in this process carries information regarding the possible neuronal impairment during MDD.

6.1.2 Contributions

The contributions of this chapter are summarized as follows.

- This chapter investigates the efficacy for a number of rs-fMRI based *static* features, *e.g.*, absolute correlation coefficient values and network metrics for classifying adolescent MDD *vs.* healthy controls. *Bivariate* and *multivariate* features are used for feature selection and classification.

- The chapter formulates the use of *differential sub-graph entropy* to extract a *sub-network* of important regions and edges that can be input to a classifier to achieve a very high accuracy, sensitivity and specificity for classifying MDD *vs.* healthy controls among adolescents. The predictive accuracy is *statistically significant*. The proposed approach also outperforms previous network based measures [26] for this prediction task.

- This chapter ranks brain regions and edges in order of priority that have higher differential *sub-graph* entropy between MDD *vs*. healthy. Empirical results show that the regions and edges identified by the proposed method have biological significance.

- The chapter demonstrates the utility of *dynamic* connectivity profiles for identifying adolescent MDD. *Dynamic* components extracted using constrained-PARAFAC and ICA achieve high sensitivity but poor specificity for classification of MDD.

- Finally, we propose a joint *static* and *dynamic* feature concatenation process to classify MDD from rs-fMRI accurately.

6.2 Materials and Methods

6.2.1 Dataset and Preprocessing

The data collection process and experiments mentioned in the present work that include human subjects were approved by the University of Minnesota *Institutional Review Board* (IRB). The study consisted of 49 adolescents with MDD and 33 healthy control subjects. The subjects were similar with respect to age, sex, or handedness as described in [26,222]. However, the two groups had significantly different values for CDRS-R [223] scores, BDI-II [224] scores, and IDAS dimension [225] scores. Additionally, there were no statistically significant differences in scores at the group level for MDD patients on medication and no-medication. The only exception was IDAS scores for these two groups that measures severity of insomnia, panic and anxiety. We describe the data acquisition and pre-processing steps following [26].

The study involved only adolescent subjects (12-19 years). Resting state functional magnetic resonance images were captured for 6 minutes with the following parameter specifications: repetition time (TR) = 2s, field of view (FOV) = 220×220mm, and voxel size of $3.43 \times 3.43 \times 4$ mm. There were 34 interleaved slices with no skip. During the scanning process, adolescents undergoing the study were awake. They were advised to close their eyes, relax and they were asked not to think about something specific.

Following rs-fMRI data acquisition, FMRIB Software Library (FSL) [129] tools were utilized in order to preprocess the raw voxel time-series. This step involves removing

skulls from images, correcting any distortions, correcting motion that may distort images. Finally, the images were registered to $2mm \times 2mm \times 2mm$ Montreal Neurological Institute space (**MNI**). In order to remove many physiological artifacts (e.g., heart rate, respiration signal, white matter and cerebrospinal fluid), we used independent component analysis tools available through **melodic** program within FSL. More details of the preprocessing can be found in [127]. After the preprocessing step, the Desikan atlas [54] was used to extract mean time-series from 85 cortical and sub-cortical regions (Table A.5 in Appendix A). The extracted mean time-series from each subjects were then subjected to wavelet frequency decomposition into 4 frequency bands using a db-4 wavelet [61]. The time-series corresponding to the previous frequency bands are described as: B1 (0.015 $\sim$ 0.03 Hz), B2 (0.03 $\sim$ 0.06Hz), B3 (0.06 $\sim$ 0.12 Hz), B4 (0.12 $\sim$ 0.25 Hz) as described in [26].

6.2.2 *Static* Features

Correlation Features

A number of connectivity measures have been described in literature [12] to estimate human brain functional connectivity. In this chapter, we use Pearson correlation coefficient as the metric for representing functional connectivity. Pearson correlation coefficient was calculated for every frequency band ($B1...B4$) using the formulae given below,

$$P^f_{i,j} = P^f_{j,i} = \frac{E[(r^f_i - \hat{r}^f_i)(r^f_j - \hat{r}^f_j)]}{\sqrt{E[(r^f_i - \hat{r}^f_i)^2]}\sqrt{E[(r^f_j - \hat{r}^f_j)^2]}} \tag{6.1}$$

.

Here $\hat{r}^f_i$ is the average of time-series for frequency band f and the region id is denoted by i. Here four adjacency matrices are created for every pair of brain regions for each subject. In this view, each of these matrices may represent adjacency matrices in functional graph where each entry represents an edge. Absolute value of these correlation coefficients are used for further processing. Thus each frequency band yields of features for each frequency band is $\frac{85\times84}{2} = 3570$ total number of unique correlation values that are later used as features for the classification task.

Network Features

As mentioned before, from each subject, four 85×85 adjacency matrices [26] were extracted. The adjacency matrices contain absolute Pearson's correlation coefficients. From these adjacency matrices, we calculated network integration and segregation measures that describe each subject's functional brain network structure using *Brain Connectivity Toolbox* (BCT) [1] . Each of the adjacency matrices are then binarized keeping {5%, 20%, 35%, 50%} of the highest values. Thus at each frequency band, every subject has same number of edges at each sparsity level.

On a local node level in the network, three features namely *local efficiency (LE), clustering coefficient (CC)* and *betweenness centrality (BC)* were computed [60, 61]. At a global level, we calculated two features namely, *modularity* and *global efficiency* [60]. The local and global features in the network represent complementary viewpoint of the network for *segregation* and *integration* of nodes, respectively. Hence from each subject, we extract $85 \times 3 \times 4$ (for 3 features at each node)$+4 \times 2$ (for *modularity and global efficiency*) = 1028 network features corresponding to two frequency bands.

An overview of the network based features is mentioned next following the descriptions in [26]. *Local efficiency* is computed using the summation of inverse of the shortest paths to the neighbors of a node. This metric is used to understand how efficient a node is for transferring information between two neighboring nodes. *Clustering coefficient* is calculated by the number of triangles created around a node out of all possible triangles. *Betweenness centrality* of a node is calculated as the percentage of shortest paths that contain the node. *Modularity* metric measures how a network is sub-divided into smaller dense sub-networks with sparse inter-connections. *Global efficiency* describes the efficiency of information transfer within the whole graph. These network measures were also previously used for classifying MDD *vs.* healthy from fMRI data as described in [26]. More details of the network measures can be found in [22].

Sub-graph Entropy

We have recently shown that *sub-graph* entropy can effectively classify brain *states* for task *vs.* no-task [20] and healthy *vs.* psychiatric patients [25]. Sub-graphs can denote

[1] `https://sites.google.com/site/bctnet/`

any portion or sub-structure of the main graph. For a sub-graph $G_s = (V_s, E_s)$, of main graph $G = (V, E)$, the sub-graph entropy can be computed as follows:

$$H\left(G_s\right) = -\sum_{x,x' \in V_s} q(x, x') \log\left(q(x, x')\right)$$

where $q(x, x')$ denotes the normalized edge weight between nodes (x, x') for sub-graph G_s. For calculating the node entropy of node x, only the sub-graph containing the 1-hop neighborhood of node x is used. Here logarithm is computed with respect to base 2. Usefulness of graph entropy as a centrality measure has been demonstrated in [51, 52] and extended to sub-graph entropy in [20].

Node Entropy: Node entropy [20] refers to a sub-graph entropy of structure containing a graph node and its immediate neighbors. Although 1-hop neighborhood has been generally used to define node substructure, k-hop neighborhood may also be considered. In this chapter, we only consider well understood 1-hop neighborhood structure to calculate node entropy. Thus only the edges in the immediate neighborhood of a node are extracted. The node entropy values are used separately as features for classification.

Edge Entropy: Edge entropy [20] refers to a sub-graph entropy of structure containing an edge and the immediate neighbors of nodes that the edge connects. In this chapter, we only consider well understood 1-hop neighborhood structure of an edge to calculate edge entropy. Thus only the edges in the immediate neighborhood of the two nodes of an edge are extracted for the calculation. The edge entropy values are used separately as features for classification.

Differential *Sub-graph* (Node and Edge) Entropy:

Differential (node/ edge) entropy refers to difference in node or edge entropy values when a same graph is gone through two different conditions. Thus when a subject suffers through a mental disorder, it is hypothesized that a healthy functional connectivity structure is disrupted and thus the segregation/integration pattern of nodes/edges change [20]. The node/edges that undergo most change in local structural pattern can be extracted based on highest change in the sub-graph entropy. Here we are mainly interested in change of a relative distribution of edge values for each subject. A brief description for differential node entropy is given next. Assume there are two groups G^1 and G^2 (in the current scenario, they refer to healthy and MDD, respectively). The

node entropy for node v_i for G^1 and G^2 are denoted as $H(G^1_{v_i})$ and $H(G^2_{v_i})$, respectively. Then differential node entropy is calculated as $|H(G^1_{v_i}) - H(G^2_{v_i})|$ [20]. The regions having higher differential node entropy are thought to have undergone the most functional connectivity changes. The same calculation process for extracting edge that have underdone disruption for MDD is carried out as well. In the next section, we describe how a leave-one-out classification process is able to extract a sub-network containing important edges that may be responsible for MDD. An algorithm for ranking the regions and edges that have high differential entropy is given in Algorithm 3 in Chapter 2.

Extracting Predictive Sub-network Based on Edge Entropy

As mentioned earlier, the edge entropy values were used to classify two groups (healthy *vs.* MDD). In order to extract a *sub-graph* that may be associated with the disruption of functional network during MDD, we used a leave-one-out analysis based on classification accuracy [25, 137]. This edge selection framework involves finding top ranked edges at each iteration and add it to the sub-network. Then the leave-one-out accuracy of the edge entropy values (that belong to only the sub-network) is measured. We stop adding edges to the sub-network once the accuracy drops beyond certain number of edges. This process is illustrated in Fig. 6.1(a). Leave-one-out classification scheme is a commonly used classification scheme for mitigating the overfitting effect due to small sample size and high number of features [124]. In all iterations, the classifier used is support vector machine with radial basis kernel. The ranking process is also carried out in a leave-one-out manner, where it is performed 82 times. At each time, the ranking of regions/edges is carried out keeping one out and then a histogram demonstrating the stability of ranking process is plotted. In order to compare the predictive performance with other sub-networks, *union* and *intersection* of top regions and edges are employed for classification [20]

6.2.3 *Dynamic* Features

To extract *dynamic* network features, regional time-series from each fMRI scan are extracted and they are reshaped to a matrix (dim 1 = spatial, dim 2 = temporal). From this matrix, a new *dynamic* connectivity matrix based on sliding window of predefined strides are formed. Each subject's regional time-series yield multiple time-series

Table 6.1: Leave-one-out classification results

Types of features	Methods	# of Features	Accuracy	Sensitivity	Specificity	Classifier
Static features	Correlation [26]	10	0.74	0.82	0.64	SVM RBF
	Network features [26]	10	0.67	0.84	0.42	SVM RBF
	Correlation + Network features [26]	20	0.79	0.86	0.70	SVM RBF
	Node entropy	25	0.67	0.84	0.42	SVM RBF
	Edge entropy (Predictive Network)	105	0.8	0.84	0.76	SVM RBF
	Union sub-graph entropy	130	0.8	0.84	0.76	SVM RBF
	Intersection sub-graph entropy	95	0.77	0.82	0.7	SVM RBF
Dynamic features	Tensor components	20	0.61	0.96	0.15	SVM RBF
	ICA	20	0.62	0.92	0.18	RF # of T 10
	PCA	20	0.57	0.86	0.15	RF # of T 10
Combined features	Feature Concatenation	125	0.82	0.84	0.79	SVM RBF

windows based on their strides, which are then used to create Pearson's correlation between regions for each time-window. Following this, the Pearson's correlation matrices are vectorized and multiple connectivity vectors are stacked to create a dFC matrix for each subject where ($\dim 1$ = edges, $\dim 2$ = temporal). The scans from a group of subjects are concatenated to form a 3-way tensor where the $\dim 3$ = subject. We denote the 3-way tensor of size $I_1 \times I_2 \times I_3$ as $\mathcal{X}_{I_1,I_2,I_3}$.

Tensor Component Analysis

Tensor component analysis is a relatively new model to extract *dynamic* components from functional networks [226]. Tensor decomposition is a high-dimensional blind source separation approach that separates the mixed signals into multiple axial components. Compared to matrix decomposition, tensor analysis has better uniqueness properties and interpretability [196]. We use a constrained parallel factor tensor decomposition (PARAFAC), implemented in [122]. The constrained PARAFAC decompostion is stated as:

$$\min_{\tilde{\mathcal{X}}} ||\mathcal{X} - \tilde{\mathcal{X}}||_F^2 \; s.t. \; \tilde{\mathcal{X}} = (A, B, C), A^T A \; = \; I, \; C \geq 0$$

Principal Component Analysis (PCA)

[199]: Principal Component Analysis was carried out on the concatenated correlation values from sliding window for all subjects. This procedure extracted common network space and unique time-courses for each subject that are orthonormal to each other. The

average value of unique time-courses were used as features for prediction. The number of components for PCA were chosen based on cross-validation performance.

Independent Component Analysis (ICA)

[178]: Independent Component Analysis is a popular method for analyzing dFC. In our experiments, ICA was also carried out on the concatenated correlation values from sliding window for all subjects. Like PCA, this analysis extracts common network space and unique time-courses for each subject that are independent of each other in statistical sense. The average value of unique time-courses are used as features for prediction. The number of components for ICA is chosen based on cross-validation performance.

6.2.4 Classifier

Each set of the features described before employs either Support Vector Machine (SVM) or Random Forest (RF) algorithms to learn classifiers since these two classifiers have been demonstrated to work reasonably well for limited samples. Specifically SVM with radial basis function (RBF) and linear kernel was utilized for all the experiments. In case of SVM with RBF kernel, a standard set of parameters $\gamma \in \{0.1 \times 2^i | i = -10, -9.., 9, 10\}$ is followed using in-fold cross-validation. The hyper-parameter C for SVM learning algorithm is kept at 1, *i.e.*, $C = 1$. For RF, number of trees was chosen based on a cross-validation by varying its range from 3 to 30. The leave-one-out classification accuracy, specificity and sensitivity are also calculated to validate our approach.

A pipeline demonstrating the whole experimental process is shown in Fig. 6.1(b).

6.3 Results

6.3.1 *Bivariate* Analysis

Using a minimum redundancy maximum relevance (mRMR) in-fold feature selection [139], 10 features that are most important according to the criterion, are selected. The selected features belong to lower frequency sub-band (B2). The classification performance by leave-one-out method was 0.74 with specificity 0.64 and sensitivity 0.82 as shown in Table 6.1 using the absolute Pearson correlation coefficients. The results show that Pearson

correlation between *FrontalPoleL - TemporalPoleR, PrecuneusL - RostralAntCingulateR and CerebCortL - BankststsL* are selected 82 out of 82 times during the mRMR feature selection and leave-one-out classification. We note that, the involvement of these regions is also confirmed by previous work [227, 228].

6.3.2 *Multivariate* Analysis

Network Features

Following the *bivariate* experiment as described in previous section, an in-fold mRMR feature selection is employed (with 10 most significant features) using network based features extracted from the functional brain graphs containing 85 regions. The leave-one-out classification accuracy using these five features was 0.67 with 0.84 sensitivity and 0.42 specificity (Table 6.1). Note that, *Clustering coefficient* of *insula* (at sparsity 50%) and *clustering coefficient* of *caudal middle frontal* (at sparsity 50%) were selected in each fold by the mRMR feature selection process. The selected features belong to lower frequency sub-band (B2). A concatenation of selected features from correlation and network based measures improved the classification accuracy to 0.79 with sensitivity 0.86 and specificity 0.70.

Node Entropy

The lower frequency band (B2) was used for calculating *sub-graph* entropy based on the classification performance. Using differential node entropy, the regions affected during MDD were identified. The regions extracted using this procedure are illustrated as a table listing of the top-25 regions in Table 6.2. In addition, the corresponding *differential entropy* value and p-value for each region's node entropy are also shown in the same Table. There are 4 regions with statistically significant difference ($p < 0.05$) in node entropy among the 25 regions. Most of the regions identified in this process belong to the default mode areas that are well known to be active during resting condition [7] [140]. Node entropy of top-25 regions extracted using Algorithm S1 had the following classification performance: accuracy 0.67 with specificity 0.42 and sensitivity 0.84 (same as network features).

Note that, the ranking can be validated for MDD by considering the regions from

executive control circuitry, default mode network and salience network [229]. Our ranking methodology is able to capture the regions from that circuit in top 15% of these most important nodes. In addition, we also show the mean *differential entropy* value and standard deviation (std) in the same figure. There are 13 regions with *differential entropy* more that 1-std away from mean. Also, 38 regions have differential entropy values more than mean. The leave-one-out classification performance using all node entropy values is shown in Table 6.1.

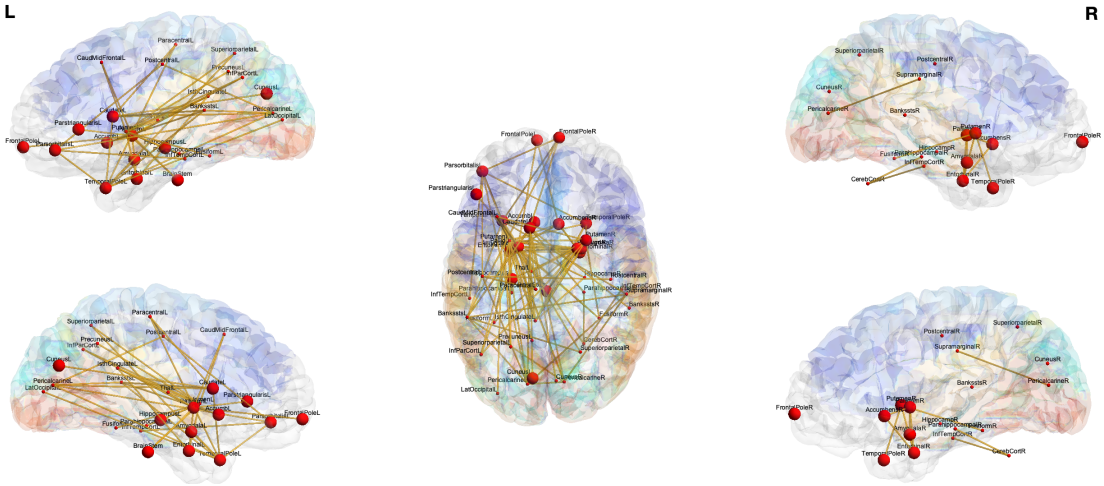

Figure 6.2: Predictive sub-network extracted using *differential edge entropy* and leave-one-out analysis.

6.3.3 Extracting Predictive Sub-network

Accuracy of Predictive Sub-network

Following the method as outlined in Fig. 6.1, we ran our edge ranking procedure Algorithm S1 for edges 82 times, each time selecting top edges for leave-one-out classification. The change in classification accuracy with the number of edges using SVM and radial basis function kernel (using only selected edges) is shown in Fig. D.2 (Appendix D). The classification accuracy has a behavior similar to traditional feature selection algorithms where it improves up to 105 edges and then starts to decrease. In order to understand the significance of the current work with the information about sub-network, the result is compared with a number of baseline network based features in terms of classification

accuracy. The comparisons of classification results is shown in Table 6.1. Edge entropies of the proposed predictive sub-network achieves 0.80 accuracy with identifying 25 out of all healthy and 41 out of 49 MDD subjects correctly. A close inspection of the results reveals several observations. First, for each group ranking procedure reveals edges that are distributed throughout the lateral and medial cortical part of the brain and some of them belong to the default mode network. Second, *differential entropy* elevates the edges that belong to fornto-parietal and frontal-subcortical areas. The regions that are connected using the edges belong to frontal lobe, parietal lobe, anetrior and posterior cingulate gyrus, thalamus proper, default mode (DMN), accumbens (striatal area) and amygdala.

Sub-network Visualization and Statistical Analysis

The identified sub-network comprising 33 regions and 105 edges is shown in Fig. 6.2. We have provided a table containing the regions from predictive sub-network in Table D.1 (Appendix D). We select these top-105 features in each iteration for leave-one-out training, and plot their occurrences using a histogram as shown in Fig. D.1 in Appendix D. The top ranked edges shown in Fig. 6.2 are also very important for classification as they are selected most of the times as top edges. In addition, the predictive sub-network achieves a p-value of 0.13 for a t-test of edge entropies between MDD *vs*. healthy. The box plot for the t-test is shown in Fig. 6.3.

6.3.4 *Dynamic* Functional Connectivity:

Dynamic connectivity features extracted through tensor, ICA, PCA in isolation had a lacklustre performance compared to *static* features. Constrained-PARAFAC with 20 components yielded an accuracy of 0.61 with sensitivity 0.96 and specificity 0.15, respectively. The classifier used in this case was support vector machine with RBF kernel. ICA produced accuracy of 0.62 with sensitivity 0.92 and specificity 0.18, respectively, whereas the corresponding results for PCA were 0.57, 0.86 and 0.15. Random forest classifier (number of trees = 10) had the best performance while using ICA and PCA features. Notably, ICA had the best accuracy and specificity values among the dFC features. Constrained-PARAFAC had the best sensitivity.

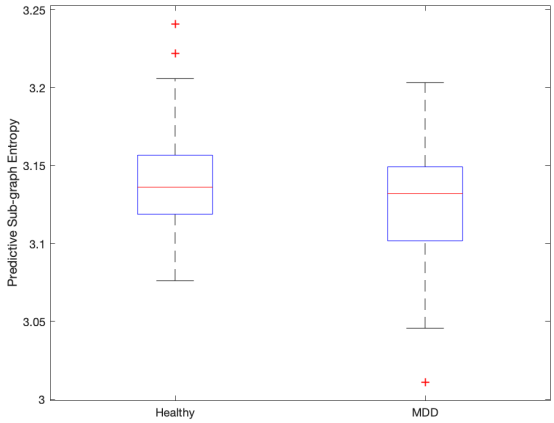

Figure 6.3: Box-plot of *sub-graph entropy* values for MDD *vs.* healthy for predictive sub-network.

6.3.5 Combined Feature Set from *Static* and *Dynamic* Connectivity:

From the *static* and *dynamic* connectivity measures, the best performing features were identified with respect to sensitivity and specificity. Thus, from *static* connectivity measures, edge entropies of predictive sub-network were selected. For *dynamic* connectivity measure, constrained-PARAFAC was selected. The two types of features were then combined to create feature vector for each subject. A leave-one-out cross-validation using this combined feature improved the performance to accuracy of 0.82, sensitivity of 0.84 and specificity of 0.79. The hyper-parameter for the classifier RBF-SVM were chosen infold and the range were chosen from the set $[2^i]$ where $i \in [-10, 10]$.

6.4 Discussion

This chapter explored the viability of automated diagnostic process for adolescent MDD patients based on rs-fMRI. We explored the feasibility of a combined *static-dynamic* feature combination scheme using edge entropy and tensor components for identifying a predictive sub-network and classification of adolescent MDD *vs.* healthy controls. The features that had the highest classification performance belonged to hemodynamic response frequency band B2 ($0.03 \sim 0.06$ Hz). This section discusses important observations from different classification schemes from mentioned the results.

6.4.1 Regions and Edges

Previous neuroimaging studies involving MDD patients have connected the disfunction of fronto-limbic circuitry. This sub-network has traditionally been responsible for regulating human emotion and the is impacted in patho-psychological analysis of MDD. Literature support for the involvement of this sub-network in MDD can be found in [230–232]. Traditionally, regions such as amygdala, insula and prefrontal cortex were demonstrated to have differntial functions for youths with MDD. In particular, an imbalance in synchronization between the frontal regions (responsible for controlling) and limbic areas specifically anterior cingulate cortex or ACC (responsible for emotion) [233, 234] is thought to cause severe symptoms for MDD patients [235]. Neuroimaging studies have also implicated reduced functional connectivity between ACC and temporal-frontal brain regions [236]. Children with depression also showed atypical functional network connections in ACC and posterior cingulate cortex (PCC) [237, 238]. This was hypothesized to be associated with lower levels of emotion regulation capability among the participant children. Additionally, adolescent MDD duration was shown to associate with the connectivity between amygdala and post central gyrus [231].

The proposed method and predictive sub-network are able to extract well-known default mode network regions for rs-fMRI scans from healthy humans [144]. For resting-state brain networks, all top regions extracted are either default mode or associated with resting-state. Adolescent MDD group showed higher differential node entropy for regions such as putamen, pallidum, accumbens, cingulate, postcentral gyrus, amygdala, pars-orbitalis and thalamus. Some of these regions were also identified in [25, 26] to have higher change in node entropy between healthy and disease states. These regions are part of of the fronto-limbic circuit [239] in brain.

Fig. 6.2 illustrates the the sub-network that was extracted using the leave-one-out classification process for healthy *vs.* adolescent MDD. As can be seen in the brain plot, the network consists of a number of nodes that have more connections than the others and thus act as hub regions [12]. The edges include connections from frontal pole to striatal node. In case of MDD *vs.* healthy, the link between DMN and limbic system also has higher importance. Additionally the sub-network contain regions like accumbens, putamen, operculum, thalamus.

6.4.2 *Dynamic* Functional Connectivity

Dynamic connectivity approaches separately were not able to perform the classification task with higher accuracy. They had very high sensitivity, i.e., they could identify true MDD subjects but had difficulty identifying the healthy controls. The poor specificity may be due to the fact that rs-fMRI may not contain many different *dynamic* states between healthy vs. adolescent MDD patients. A task based fMRI may be able to magnify the state differences between healthy controls and MDD patients.

6.4.3 Validation

In order to demonstrate that the combined *static-dynamic* features have better than chance statistical significance for classification, bionomial tests were performed on the results [25,221]. The proposed feature set had significantly more predictive performance ($\mathrm{p} = 9.24 \times 10^{-09}$ for classifying healthy *vs.* adolescent MDD with respect to a naive random chance classifier. However, with respect to [60], the test yielded $p = 0.32$. A box-plot containing the sub-graph entropies for predictive network is illustrated in Fig. 6.3. It is evident that, MDD patients tend to have lower entropy compared with healthy controls.

6.4.4 Predictive Sub-network as Part of Other Known Networks

The key observations from our experiments implied that a number of regions and functional connections from brain sub-networks that were discovered before and well-known in fMRI literature are affected for adolescent MDD.

Default Mode Network (DMN)

When a person is not actively doing a particular tasks, some regions of brain are still activated. The network consisting these regions are so called default mode network of human brain [7,145]. These regions active during rest are thought be be responsible for our day dreams, wandering minds, self ruminations etc. The algorithm prescribed in this chapter using differential sub-graph entropy is able to extract regions such as cingulate cortex, temporal pole, parahippocampus, precuneus and medial prefrontal cortex, that

are traditionally thought to be part of DMN. Previous research have supported the hypothesis that adolescent MDD brain goes through changes in DMN [240, 241].

Salience

Salience network (SN) is typically associated with regions that show increased activation when a subject tries to decide the where to focus their attention. Additionally, SN supports a mechanism that helps subjects attend important visual/other cues that are prominent compared with the background. The adolscent MDD predictive network includes entorhinal, hippocampus from SN [149, 150] network. Apart from that, salience network involves regions from cingulate, pallidum, thalamus etc. The regions and functional edges extracted through leave-one-out process may indicate that adolescent MDD subjects focus on physical cues in a different way compared to healthy adolescents [242, 243].

Executive Network

The executive network (EN) of human brain consists of neuronal units from frontal-parietal network. EN is hypothesized to support higher cognitive functions in humans, . *e.g.*, making a decision and/or solving a problem at hand. Many nodes belonging to fronto-parietal network were extracted as part of the predictive sub-network (Fig. 6.1). These regions include parsorbitalis, hippocampus, caudate, frontal pole, temporal cortex, and putamen. The implication of these fronto-parietal regions may illuminate a possible change in exectutive network functions for adolescents suffering from MDD in comparison with healthy subjects [229, 244].

Fronto-Limbic

Fronto-limbic system in brain controls the resistance of distraction for any goal oriented behavior. The predictive sub-network consisted regions from this special brain circuits. Regions such as accumbens, hippocampus and postcentral in the predictive network are responsible for lower-level emotional responses in brain (fight or flight). Their dysfunction for adolescent MDD has been reported in the literature [229, 240].

6.5 Conclusion and Future Work

This chapter explored a number of rs-fMRI based *static* and *dynamic* connectivity approaches to classify adolescents with MDD *vs*. healthy subjects. Using edge entropy and leave-one-out analysis, we showed that a predictive sub-network containing subsections of multiple large scale brain networks yields good prediction performance in terms of accuracy and specificity. The regions and edges in this sub-network indicate possible functional deterioration of brain cuircuits during adolescent MDD. However, features exploiting *dynamic* connectivity approaches alone did not yield good performance. However, a the combined feature set from *static* and *dynamic* connectivity had the highest classification accuracy. Some of the regions and edges extracted by high differential sub-graph entropy had significantly different sub-graph entropy values. Future work will include predicting the clinical scores based on these feature sets. Additionally, future effort will be directed towards understanding effect of psychotropic medications on MDD patients with respect to sub-graph entropy and other large-scale network measures.

Table 6.2: Top-25 regions extracted using *differential node entropy* for MDD *vs*. healthy data.

Rank	Region / Hemisphere	Diff. Entropy	p-value
1	Putamen - L	0.5505	0.0076
2	Parsorbitalis - L	0.4662	0.0353
3	Pallidum - L	0.4126	0.1316
4	Putamen - R	0.4114	0.0477
5	Isthmus Cingulate - L	0.3796	0.0072
6	Accumbens - R	0.3509	0.1872
7	Entorhinal - R	0.3500	0.2403
8	Caudate - L	0.3280	0.1512
9	Pallidum - R	0.3134	0.2771
10	BrainStem	0.2890	0.3126
11	CerebCort - R	0.2881	0.2706
12	Pericalcarine - R	0.2792	0.1154
13	Pericalcarine - L	0.2694	0.1036
14	Postcentral - L	0.2682	0.1745
15	Supramarginal - R	0.2669	0.1727
16	Thalamus - L	0.2627	0.2208
17	Fusiform - R	0.2589	0.1316
18	Fusiform - L	0.2317	0.2052
19	Bankssts - L	0.2275	0.3956
20	CaudMidFrontal - L	0.2101	0.2655
21	Precuneus - L	0.2065	0.0946
22	Lateral Occipital - L	0.2005	0.3162
23	Bankssts - R	0.2003	0.3449
24	InfParCort - L	0.1959	0.2124
25	Amygdala - R	0.1898	0.4927

References

[1] M.C. Rosario-Campos, E.C. Miguel, S. Quatrano, P. Chacon, Y. Ferrao, D. Findley, L. Katsovich, L. Scahill, R.A. King, S.R. Woody, et al., "The dimensional yale–brown obsessive–compulsive scale (DY-BOCS): an instrument for assessing obsessive–compulsive symptom dimensions," *Molecular Psychiatry*, vol. 11, no. 5, pp. 495, 2006.

[2] Gail A Bernstein, Andrea M Victor, Peter M Nelson, and Susanne S Lee, "Pediatric obsessive–compulsive disorder: Symptom patterns and confirmatory factor analysis," *Journal of Obsessive-Compulsive and Related Disorders*, vol. 2, no. 3, pp. 299–305, 2013.

[3] A. R. Hariri et al., "The amygdala response to emotional stimuli: a comparison of faces and scenes," *NeuroImage*, vol. 17, no. 1, pp. 317–323, 2002.

[4] M. R. Delgado et al., "Tracking the hemodynamic responses to reward and punishment in the striatum," *Journal of Neurophysiology*, vol. 84, no. 6, pp. 3072–3077, 2000.

[5] O. Sporns, "Graph theory methods for the analysis of neural connectivity patterns," in *Neuroscience Databases*, pp. 171–185. Springer, 2003.

[6] M. W. Cole et al., "Intrinsic and task-evoked network architectures of the human brain," *Neuron*, vol. 83, no. 1, pp. 238–251, 2014.

[7] M. D. Greicius, B. Krasnow, A. L. Reiss, and V. Menon, "Functional connectivity in the resting brain: a network analysis of the default mode hypothesis,"

Proceedings of the National Academy of Sciences, vol. 100, no. 1, pp. 253–258, 2003.

[8] K. J. Friston et al., "Functional connectivity: the principal-component analysis of large (pet) data sets," *Journal of Cerebral Blood Flow & Metabolism*, vol. 13, no. 1, pp. 5–14, 1993.

[9] K. J. Friston, "Functional and effective connectivity in neuroimaging: a synthesis," *Human Brain Mapping*, vol. 2, no. 1-2, pp. 56–78, 1994.

[10] S.-H. Chu et al., "Function-specific and enhanced brain structural connectivity mapping via joint modeling of diffusion and functional mri," *Scientific reports*, vol. 8, no. 1, pp. 4741, 2018.

[11] G. Atluri et al., "The brain-network paradigm: Using functional imaging data to study how the brain works," *computer*, vol. 49, no. 10, pp. 65–71, 2016.

[12] E. Bullmore and O. Sporns, "Complex brain networks: graph theoretical analysis of structural and functional systems," *Nature Reviews Neuroscience*, vol. 10, no. 3, pp. 186, 2009.

[13] M. Preti et al., "The dynamic functional connectome: state-of-the-art and perspectives," *NeuroImage*, vol. 160, pp. 41–54, 2017.

[14] V. D Calhoun et al., "A method for making group inferences from functional mri data using independent component analysis," *Human Brain Mapping*, vol. 14, no. 3, pp. 140–151, 2001.

[15] C. Beckmann and S. Smith, "Probabilistic independent component analysis for functional magnetic resonance imaging," *IEEE transactions on medical imaging*, vol. 23, no. 2, pp. 137–152, 2004.

[16] V. Kiviniemi et al., "A sliding time-window ica reveals spatial variability of the default mode network in time," *Brain Connectivity*, vol. 1, no. 4, pp. 339–347, 2011.

[17] M. J. Jafri et al., "A method for functional network connectivity among spatially independent resting-state components in schizophrenia," *NeuroImage*, vol. 39, no. 4, pp. 1666–1681, 2008.

[18] Ü. Sakoğlu et al., "A method for evaluating dynamic functional network connectivity and task-modulation: application to schizophrenia," *Magnetic Resonance Materials in Physics, Biology and Medicine*, vol. 23, no. 5-6, pp. 351–366, 2010.

[19] E. A. Allen et al., "Tracking whole-brain connectivity dynamics in the resting state," *Cerebral Cortex*, vol. 24, no. 3, pp. 663–676, 2014.

[20] B. Sen, S. H. Chu, and K. K. Parhi, "Ranking regions, edges and classifying tasks in functional brain graphs by sub-graph entropy," *Scientific Reports*, vol. 9, no. 1, pp. 1–20, 2019.

[21] V. Latora and M. Marchiori, "Efficient behavior of small-world networks," *Physical Review Letters*, vol. 87, no. 19, pp. 198701, 2001.

[22] M. Rubinov and O. Sporns, "Complex network measures of brain connectivity: uses and interpretations," *NeuroImage*, vol. 52, no. 3, pp. 1059–1069, 2010.

[23] L. C. Freeman, D. Roeder, and R. R. Mulholland, "Centrality in social networks: Ii. experimental results," *Social networks*, vol. 2, no. 2, pp. 119–141, 1979.

[24] M. E. J. Newman, "Modularity and community structure in networks," *Proceedings of the National Academy of Sciences*, vol. 103, no. 23, pp. 8577–8582, 2006.

[25] B. Sen, G. A. Bernstein, B. A. Mueller, K. R. Cullen, and K. K. Parhi, "Sub-graph entropy based network approaches for classifying adolescent obsessive-compulsive disorder from resting-state functional mri," *NeuroImage: Clinical*, vol. 26, pp. 102208, 2020.

[26] B. Sen, , B. A. Mueller, Bonnie Klimes-Dougan, K. R. Cullen, and K. K. Parhi, "Classification of major depressive disorder from resting-state fMRI," in *IEEE 41st Annual International Conference of the Engineering in Medicine and Biology Society (EMBC)*, 2019.

[27] T. Bolt, P. J. Laurienti, R. Lyday, A. Morgan, and D. Dagenbach, "Graph-theoretical study of functional changes associated with the Iowa gambling task," *Frontiers in human neuroscience*, vol. 10, pp. 314, 2016.

[28] L. Quante, Daniel S. Kluger, P. C. Burkner, M. Ekman, and R. Schubotz, "Graph measures in task-based fMRI: Functional integration during read-out of visual and auditory information," *PloS one*, vol. 13, no. 11, pp. e0207119, 2018.

[29] D. C. Van Essen et al., "The WU-Minn human connectome project: an overview," *NeuroImage*, vol. 80, pp. 62–79, 2013.

[30] GD Honey, CHY Fu, J Kim, MJ Brammer, TJ Croudace, J Suckling, EM Pich, SCR Williams, and ET Bullmore, "Effects of verbal working memory load on corticocortical connectivity modeled by path analysis of functional magnetic resonance imaging data," *NeuroImage*, vol. 17, no. 2, pp. 573–582, 2002.

[31] F. Homae et al., "Selective enhancement of functional connectivity in the left prefrontal cortex during sentence processing," *NeuroImage*, vol. 20, no. 1, pp. 578–586, 2003.

[32] T. Vanderwal et al., "Individual differences in functional connectivity during naturalistic viewing conditions," *NeuroImage*, vol. 157, pp. 521–530, 2017.

[33] J. Richiardi et al., "Decoding brain states from fMRI connectivity graphs," *NeuroImage*, vol. 56, no. 2, pp. 616–626, 2011.

[34] D. C. Van Essen et al., "The Human Connectome Project: a data acquisition perspective," *NeuroImage*, vol. 62, no. 4, pp. 2222–2231, 2012.

[35] D. A. Fair et al., "A method for using blocked and event-related fMRI data to study "resting state" functional connectivity," *NeuroImage*, vol. 35, no. 1, pp. 396–405, 2007.

[36] X. Zuo et al., "Network centrality in the human functional connectome," *Cerebral Cortex*, vol. 22, no. 8, pp. 1862–1875, 2011.

[37] H. Cao et al., "Test–retest reliability of fMRI-based graph theoretical properties during working memory, emotion processing, and resting state," *NeuroImage*, vol. 84, pp. 888–900, 2014.

[38] V. D. Calhoun et al., "The chronnectome: time-varying connectivity networks as the next frontier in fmri data discovery," *Neuron*, vol. 84, no. 2, pp. 262–274, 2014.

[39] K. E. Joyce, P. J. Laurienti, J. H. Burdette, and S. Hayasaka, "A new measure of centrality for brain networks," *Plos One*, vol. 5, no. 8, pp. e12200, 2010.

[40] C. F. Beckmann et al., "General multilevel linear modeling for group analysis in fmri," *NeuroImage*, vol. 20, no. 2, pp. 1052–1063, 2003.

[41] G. Sabidussi, "The centrality index of a graph," *Psychometrika*, vol. 31, no. 4, pp. 581–603, 1966.

[42] P. Bonacich, "Factoring and weighting approaches to status scores and clique identification," *Journal of mathematical sociology*, vol. 2, no. 1, pp. 113–120, 1972.

[43] M. E. J. Newman, "A measure of betweenness centrality based on random walks," *Social networks*, vol. 27, no. 1, pp. 39–54, 2005.

[44] A. Zalesky et al., "Network-based statistic: identifying differences in brain networks," *NeuroImage*, vol. 53, no. 4, pp. 1197–1207, 2010.

[45] C. E. Shannon, "A mathematical theory of communication," *The Bell system Technical Journal*, vol. 27, no. 3, pp. 379–423, 1948.

[46] V.A. Skorobogatov and A. A. Dobrynin, "Metrical analysis of graphs," *MATCH*, vol. 23, pp. 105–155, 1988.

[47] N. Trinajstivc, "Chemical graph theory," *CRC Press*, vol. 23, 1992.

[48] E. Trucco, "A note on the information content of graphs," *Bulletin of Mathematical Biology*, vol. 18, no. 2, pp. 129–135, 1956.

[49] A. Mowshowitz, "Entropy and the complexity of graphs: I. an index of the relative complexity of a graph," *The Bulletin of Mathematical Biophysics*, vol. 30, no. 1, pp. 175–204, 1968.

[50] M. Dehmer, "Information processing in complex networks: Graph entropy and information functionals," *Applied Mathematics and Computation*, vol. 201, no. 1-2, pp. 82–94, 2008.

[51] K. D. Mackenzie, "The information theoretic entropy function as a total expected participation index for communication network experiments," *Psychometrika*, vol. 31, no. 2, pp. 249–254, 1966.

[52] J. Shetty and J. Adibi, "Discovering important nodes through graph entropy the case of enron email database," in *Proceedings of the 3rd international workshop on Link discovery*. ACM, 2005, pp. 74–81.

[53] C. Noble and D. Cook, "Graph-based anomaly detection," in *Proceedings of the ninth ACM SIGKDD international conference on Knowledge discovery and data mining*. ACM, 2003, pp. 631–636.

[54] R. S. Desikan et al., "An automated labeling system for subdividing the human cerebral cortex on mri scans into gyral based regions of interest," *NeuroImage*, vol. 31, no. 3, pp. 968–980, 2006.

[55] M. Xia, J. Wang, and Y. He, "BrainNet Viewer: a network visualization tool for human brain connectomics," *Plos One*, vol. 8, no. 7, pp. e68910, 2013.

[56] A. Barrat et al., "The architecture of complex weighted networks: Measurements and models," in *Large Scale Structure And Dynamics Of Complex Networks: From Information Technology to Finance and Natural Science*, pp. 67–92. World Scientific, 2007.

[57] B. Sen and K. Parhi, "Predicting tasks from task-fMRI using blind source separation," *53rd Asilomar Conference on Signals, Systems, and Computers*, pp. 2201–2205, 2019.

[58] T. Xu et al., "Classification of single-trial meg during sentence processing for automated schizophrenia screening," in *6th International IEEE/EMBS Conference on Neural Engineering (NER)*. IEEE, 2013, pp. 363–366.

[59] T. Xu et al., "Classification of borderline personality disorder based on spectral power of resting-state fmri," in *IEEE 36th Annual International Conference of the IEEE Engineering in Medicine and Biology Society.*, 2014, vol. 2014, pp. 5036–5039.

[60] B. Sen et al., "Classification of obsessive-compulsive disorder from resting-state fMRI," in *IEEE 38th Annual International Conference of the Engineering in Medicine and Biology Society (EMBC), 2016*. IEEE, 2016, pp. 3606–3609.

[61] T. Xu et al., "Network analysis of functional brain connectivity in borderline personality disorder using resting-state fmri," *NeuroImage: Clinical*, vol. 11, pp. 302–315, 2016.

[62] M. W. Cole, S. Pathak, and W. Schneider, "Identifying the brain's most globally connected regions," *NeuroImage*, vol. 49, no. 4, pp. 3132–3148, 2010.

[63] D. Tomasi and N. D. Volkow, "Functional connectivity density mapping," *Proceedings of the National Academy of Sciences*, vol. 107, no. 21, pp. 9885–9890, 2010.

[64] G. McCarthy et al., "Face-specific processing in the human fusiform gyrus," *Journal of Cognitive Neuroscience*, vol. 9, no. 5, pp. 605–610, 1997.

[65] H. Kawasaki et al., "Processing of facial emotion in the human fusiform gyrus," *Journal of Cognitive Neuroscience*, vol. 24, no. 6, pp. 1358–1370, 2012.

[66] F. Apicella et al., "Fusiform gyrus responses to neutral and emotional faces in children with autism spectrum disorders: a high density erp study," *Behavioural Brain Research*, vol. 251, pp. 155–162, 2013.

[67] M. Barrot et al., "CREB activity in the nucleus accumbens shell controls gating of behavioral responses to emotional stimuli," *Proceedings of the National Academy of Sciences*, vol. 99, no. 17, pp. 11435–11440, 2002.

[68] C. S. Monk et al., "Amygdala and nucleus accumbens activation to emotional facial expressions in children and adolescents at risk for major depression," *american Journal of Psychiatry*, vol. 165, no. 1, pp. 90–98, 2008.

[69] S. B. Floresco, "The nucleus accumbens: an interface between cognition, emotion, and action," *Annual Review of Psychology*, vol. 66, pp. 25–52, 2015.

[70] G. Bush et al., "Cognitive and emotional influences in anterior cingulate cortex," *Trends in Cognitive Sciences*, vol. 4, no. 6, pp. 215–222, 2000.

[71] J. M. Allman et al., "The anterior cingulate cortex: the evolution of an interface between emotion and cognition," *Annals of the New York Academy of Sciences*, vol. 935, no. 1, pp. 107–117, 2001.

[72] A. Etkin et al., "Emotional processing in anterior cingulate and medial prefrontal cortex," *Trends in Cognitive Sciences*, vol. 15, no. 2, pp. 85–93, 2011.

[73] E. A. Phelps, "Human emotion and memory: interactions of the amygdala and hippocampal complex," *Current Opinion in Neurobiology*, vol. 14, no. 2, pp. 198–202, 2004.

[74] P. Sarkheil et al., "Emotion unfolded by motion: a role for parietal lobe in decoding dynamic facial expressions," *Social Cognitive and Affective Neuroscience*, vol. 8, no. 8, pp. 950–957, 2012.

[75] T. Ishizu and S. Zeki, "Toward a brain-based theory of beauty," *Plos One*, vol. 6, no. 7, pp. e21852, 2011.

[76] A. Aron et al., "Reward, motivation, and emotion systems associated with early-stage intense romantic love," *Journal of Neurophysiology*, vol. 94, no. 1, pp. 327–337, 2005.

[77] R. D. Lane et al., "Neural correlates of heart rate variability during emotion," *NeuroImage*, vol. 44, no. 1, pp. 213–222, 2009.

[78] A. Kerr and P. D. Zelazo, "Development of "hot" executive function: The children's gambling task," *Brain and Cognition*, vol. 55, no. 1, pp. 148–157, 2004.

[79] B. Knutson et al., "Dissociation of reward anticipation and outcome with event-related fMRI," *Neuroreport*, vol. 12, no. 17, pp. 3683–3687, 2001.

[80] B. Knutson et al., "A region of mesial prefrontal cortex tracks monetarily rewarding outcomes: characterization with rapid event-related fMRI," *NeuroImage*, vol. 18, no. 2, pp. 263–272, 2003.

[81] E. Camara et al., "Microstructural brain differences predict functional hemodynamic responses in a reward processing task," *Journal of Neuroscience*, vol. 30, no. 34, pp. 11398–11402, 2010.

[82] S. C. Tanaka et al., "Prediction of immediate and future rewards differentially recruits cortico-basal ganglia loops," *Nature Neuroscience*, vol. 7, no. 8, pp. 887, 2004.

[83] D. Foti et al., "Event-related potential activity in the basal ganglia differentiates rewards from nonrewards: Temporospatial principal components analysis and source localization of the feedback negativity," *Human Brain Mapping*, vol. 32, no. 12, pp. 2207–2216, 2011.

[84] R. Elliott et al., "Dissociable neural responses in human reward systems," *Journal of Neuroscience*, vol. 20, no. 16, pp. 6159–6165, 2000.

[85] X. Li et al., "The iowa gambling task in fmri images," *Human Brain Mapping*, vol. 31, no. 3, pp. 410–423, 2010.

[86] A. Bechara et al., "Different contributions of the human amygdala and ventromedial prefrontal cortex to decision-making," *Journal of Neuroscience*, vol. 19, no. 13, pp. 5473–5481, 1999.

[87] F. D. Zeeb and C. A. Winstanley, "Functional disconnection of the orbitofrontal cortex and basolateral amygdala impairs acquisition of a rat gambling task and disrupts animals' ability to alter decision-making behavior after reinforcer devaluation," *Journal of Neuroscience*, vol. 33, no. 15, pp. 6434–6443, 2013.

[88] M. M. Botvinick et al., "Conflict monitoring and anterior cingulate cortex: an update," *Trends in Cognitive Sciences*, vol. 8, no. 12, pp. 539–546, 2004.

[89] N. Eshel et al., "Neural substrates of choice selection in adults and adolescents: development of the ventrolateral prefrontal and anterior cingulate cortices," *Neuropsychologia*, vol. 45, no. 6, pp. 1270–1279, 2007.

[90] B. Adinoff et al., "Resting regional cerebral blood flow and gambling task performance in cocaine-dependent subjects and healthy comparison subjects," *American Journal of Psychiatry*, vol. 160, no. 10, pp. 1892–1894, 2003.

[91] H. Fukui et al., "Functional activity related to risk anticipation during performance of the iowa gambling task," *NeuroImage*, vol. 24, no. 1, pp. 253–259, 2005.

[92] J. R. Binder et al., "Mapping anterior temporal lobe language areas with fmri: a multicenter normative study," *NeuroImage*, vol. 54, no. 2, pp. 1465–1475, 2011.

[93] D. M. Barch et al., "Function in the human connectome: task-fmri and individual differences in behavior," *NeuroImage*, vol. 80, pp. 169–189, 2013.

[94] M. F. Glasser et al., "The minimal preprocessing pipelines for the human connectome project," *NeuroImage*, vol. 80, pp. 105–124, 2013.

[95] G. H. Golub and C. Van Loan, "An analysis of the total least squares problem," *SIAM Journal on Numerical Analysis*, vol. 17, no. 6, pp. 883–893, 1980.

[96] K. D. Mackenzie, "Structural centrality in communications networks," *Psychometrika*, vol. 31, no. 1, pp. 17–25, 1966.

[97] C. Chang and C. Lin, "Libsvm: a library for support vector machines," *ACM Transactions on Intelligent Systems and Technology (TIST)*, vol. 2, no. 3, pp. 27, 2011.

[98] Y. Park et al., "Seizure prediction with spectral power of eeg using cost-sensitive support vector machines," *Epilepsia*, vol. 52, no. 10, pp. 1761–1770, 2011.

[99] Z. Zhang and K. K. Parhi, "Low-complexity seizure prediction from ieeg/seeg using spectral power and ratios of spectral power," *IEEE Transactions on Biomedical Circuits and Systems*, vol. 10, no. 3, pp. 693–706, 2016.

[100] T. Xu, M. Stephane, and K. Parhi, "Abnormal neural oscillations in schizophrenia assessed by spectral power ratio of meg during word processing," *IEEE Transactions on Neural Systems and Rehabilitation Engineering*, vol. 24, no. 11, pp. 1148–1158, 2016.

[101] L. James et al., "Development and application of a diagnostic algorithm for posttraumatic stress disorder," *Psychiatry Research: Neuroimaging*, vol. 231, no. 1, pp. 1–7, 2015.

[102] C. Zhang, F. Cong, T. Kujala, W. Liu, J. Liu, T. Parviainen, and T. Ristaniemi, "Network entropy for the sequence analysis of functional connectivity graphs of the brain," *Entropy*, vol. 20, no. 5, pp. 311, 2018.

[103] U. Acharya, H. Fujita, V. Sudarshan, S. Bhat, and J. Koh, "Application of entropies for automated diagnosis of epilepsy using eeg signals: A review," *Knowledge-Based Systems*, vol. 88, pp. 85–96, 2015.

[104] D. Shuman, S. K. Narang, P. Frossard, A. Ortega, and P. Vandergheynst, "The emerging field of signal processing on graphs: Extending high-dimensional data analysis to networks and other irregular domains," *IEEE Signal Processing Magazine*, vol. 30, no. 3, pp. 83–98, 2013.

[105] B. Girault, P. Gonçalves, and É. Fleury, "Translation on graphs: An isometric shift operator," *IEEE Signal Processing Letters*, vol. 22, no. 12, pp. 2416–2420, 2015.

[106] A. Sandryhaila and J. Moura, "Discrete signal processing on graphs," *IEEE Transactions on Signal Processing*, vol. 61, no. 7, pp. 1644–1656, 2013.

[107] S. Segarra and A. Ribeiro, "Stability and continuity of centrality measures in weighted graphs," *IEEE Transactions on Signal Processing*, vol. 64, no. 3, pp. 543–555, 2015.

[108] S. Murai and Y. Yoshida, "Sensitivity analysis of centralities on unweighted networks," in *The World Wide Web Conference*, 2019, pp. 1332–1342.

[109] M. Shaw, "Group structure and the behavior of individuals in small groups," *The Journal of psychology*, vol. 38, no. 1, pp. 139–149, 1954.

[110] L. C. Freeman, "A set of measures of centrality based on betweenness," *Sociometry*, pp. 35–41, 1977.

[111] E. Costenbader and T. W. Valente, "The stability of centrality measures when networks are sampled," *Social Networks*, vol. 25, no. 4, pp. 283–307, 2003.

[112] S. P. Borgatti, K. M. Carley, and D. Krackhardt, "On the robustness of centrality measures under conditions of imperfect data," *Social Networks*, vol. 28, no. 2, pp. 124–136, 2006.

[113] S. Pozza and F. Tudisco, "On the stability of network indices defined by means of matrix functions," *SIAM Journal on Matrix Analysis and Applications*, vol. 39, no. 4, pp. 1521–1546, 2018.

[114] A. Žnidaršič, A. Ferligoj, and P. Doreian, "Stability of centrality measures in valued networks regarding different actor non-response treatments and macro-network structures," *Network Science*, vol. 6, no. 1, pp. 1–33, 2018.

[115] E. Ceci and S. Barbarossa, "Graph signal processing in the presence of topology uncertainties," *IEEE Transactions on Signal Processing*, vol. 68, pp. 1558–1573, 2020.

[116] C. Durón, Y. Pan, D. H. Gutmann, J. Hardin, and A. Radunskaya, "Variability of betweenness centrality and its effect on identifying essential genes," *Bulletin of mathematical biology*, vol. 81, no. 9, pp. 3655–3673, 2019.

[117] S. A. Rasmussen and J. L. Eisen, "The epidemiology and differential diagnosis of obsessive-compulsive disorder," in *Zwangsstörungen/obsessive-compulsive disorders*, pp. 1–14. Springer, 1992.

[118] R. King, H. Leonard, and J. March, "Practice parameters for the assessment and treatment of children and adolescents with obsessive compulsive disorder," *J Am Acad Child Adolesc Psychiatry*, vol. 37(10 suppl), 1998.

[119] K. Grabill, L. Merlo, D. Duke, K. L. Harford, M. L. Keeley, G. R. Geffken, and E. A. Storch, "Assessment of obsessive–compulsive disorder: a review," *Journal of Anxiety Disorders*, vol. 22, no. 1, pp. 1–17, 2008.

[120] D. S Bassett, B. G. Nelson, B. A. Mueller, J. Camchong, and K. O. Lim, "Altered resting state complexity in schizophrenia," *NeuroImage*, vol. 59, no. 3, pp. 2196–2207, 2012.

[121] M. T. Mitterschiffthaler, U. Ettinger, M. A. Mehta, D. Mataix-Cols, and Steve C.R. Williams, "Applications of functional magnetic resonance imaging in psychiatry," *Journal of Magnetic Resonance Imaging: An Official Journal of the International Society for Magnetic Resonance in Medicine*, vol. 23, no. 6, pp. 851–861, 2006.

[122] B. Sen and K. K. Parhi, "Extraction of common task signals and spatial maps from group fMRI using a parafac-based tensor decomposition technique," in *Proc. 2017 IEEE International Conference on Acoustics, Speech and Signal Processing (ICASSP)*. IEEE, 2017, pp. 1113–1117.

[123] A. Dragomir, A. G. Vrahatis, and A. Bezerianos, "A network-based perspective in alzheimer's disease: Current state and an integrative framework," *IEEE Journal of Biomedical and Health Informatics*, vol. 23, no. 1, pp. 14–25, 2018.

[124] J. Huang, Q. Zhu, X. Hao, X. Shi, S. Gao, X. Xu, and D. Zhang, "Identifying resting-state multifrequency biomarkers via tree-guided group sparse learning for schizophrenia classification," *IEEE Journal of Biomedical and Health Informatics*, vol. 23, no. 1, pp. 342–350, 2018.

[125] R. Armañanzas, M. Iglesias, D. A. Morales, and L. Alonso-Nanclares, "Voxel-based diagnosis of Alzheimer's disease using classifier ensembles," *IEEE Journal of Biomedical and Health Informatics*, vol. 21, no. 3, pp. 778–784, 2016.

[126] C. C. Armstrong, T. D. Moody, J. D. Feusner, J. T. McCracken, S. Chang, J. G. Levitt, J. C. Piacentini, and J. O'Neill, "Graph-theoretical analysis of resting-state fMRI in pediatric obsessive–compulsive disorder," *Journal of Affective Disorders*, vol. 193, pp. 175–184, 2016.

[127] G. Bernstein et al., "Abnormal striatal resting-state functional connectivity in adolescents with obsessive–compulsive disorder," *Psychiatry Research: Neuroimaging*, vol. 247, pp. 49–56, 2016.

[128] D. A. Feinberg et al., "Multiplexed echo planar imaging for sub-second whole brain fMRI and fast diffusion imaging," *Plos One*, vol. 5, no. 12, pp. e15710, 2010.

[129] M. Jenkinson et al., "Fsl," *NeuroImage*, vol. 62, no. 2, pp. 782–790, 2012.

[130] O. A. Rosso, S. Blanco, J. Yordanova, V. Kolev, A. Figliola, M. Schürmann, and E. Başar, "Wavelet entropy: a new tool for analysis of short duration brain electrical signals," *Journal of Neuroscience Methods*, vol. 105, no. 1, pp. 65–75, 2001.

[131] M. Lynall, D. Bassett, R. Kerwin, P. J. McKenna, M. Kitzbichler, U. Muller, and E. Bullmore, "Functional connectivity and brain networks in schizophrenia," *Journal of Neuroscience*, vol. 30, no. 28, pp. 9477–9487, 2010.

[132] R. R. Coifman and M. V. Wickerhauser, "Entropy-based algorithms for best basis selection," *IEEE Transactions on Information Theory*, vol. 38, no. 2, pp. 713–718, 1992.

[133] D. L. Donoho, I. M. Johnstone, et al., "Ideal denoising in an orthonormal basis chosen from a library of bases," *Comptes Rendus de L'Académie des Sciences. Série I, Mathématique*, vol. 319, no. 12, pp. 1317–1322, 1994.

[134] B. Sen, B. Mueller, B. Klimes-Dougan, K. Cullen, and K. K. Parhi, "Classification of major depressive disorder from resting-state fmri," in *2019 41st Annual International Conference of the IEEE Engineering in Medicine and Biology Society (EMBC)*, July 2019, pp. 3511–3514.

[135] J. Körner, "Coding of an information source having ambiguous alphabet and the entropy of graphs," in *6th Prague Conference on Information Theory*, 1973, pp. 411–425.

[136] A. Li and Y. Pan, "Structural information and dynamical complexity of networks," *IEEE Transactions on Information Theory*, vol. 62, no. 6, pp. 3290–3339, 2016.

[137] J. Richiardi et al., "Machine learning with brain graphs: Predictive modeling approaches for functional imaging in systems neuroscience," *IEEE Signal Processing Magazine*, vol. 30, no. 3, pp. 58–70, 2013.

[138] T. Bao, B. N. Klatt, S. L. Whitney, K. H. Sienko, and J. Wiens, "Automatically evaluating balance: a machine learning approach," *IEEE Transactions on Neural Systems and Rehabilitation Engineering*, vol. 27, no. 2, pp. 179–186, 2019.

[139] H. Peng, F. Long, and C. Ding, "Feature selection based on mutual information: criteria of max-dependency, max-relevance, and min-redundancy," *IEEE Transactions on Pattern Analysis & Machine Intelligence*, , no. 8, pp. 1226–1238, 2005.

[140] M. E. Raichle et al., "A default mode of brain function," *Proceedings of the National Academy of Sciences*, vol. 98, no. 2, pp. 676–682, 2001.

[141] K. D. Fitzgerald, R. C. Welsh, E. R. Stern, M. Angstadt, G. L. Hanna, J. L. Abelson, and S. F. Taylor, "Developmental alterations of frontal-striatal-thalamic connectivity in obsessive-compulsive disorder," *Journal of the American Academy of Child & Adolescent Psychiatry*, vol. 50, no. 9, pp. 938–948, 2011.

[142] A. M. Weber, N. Soreni, and M. David Noseworthy, "A preliminary study of functional connectivity of medication naive children with obsessive–compulsive disorder," *Progress in Neuro-Psychopharmacology and Biological Psychiatry*, vol. 53, pp. 129–136, 2014.

[143] P. Gruner, A. Anticevic, D. Lee, and C. Pittenger, "Arbitration between action strategies in obsessive-compulsive disorder," *The Neuroscientist*, vol. 22, no. 2, pp. 188–198, 2016.

[144] M. D. Greicius et al., "Resting-state functional connectivity reflects structural connectivity in the default mode network," *Cerebral cortex*, vol. 19, no. 1, pp. 72–78, 2008.

[145] B. Biswal, F. Zerrin Yetkin, V. M. Haughton, and J. S. Hyde, "Functional connectivity in the motor cortex of resting human brain using echo-planar mri," *Magnetic resonance in medicine*, vol. 34, no. 4, pp. 537–541, 1995.

[146] J. C. Beucke, J. Sepulcre, et al., "Default mode network subsystem alterations in obsessive–compulsive disorder," *The British Journal of Psychiatry*, vol. 205, no. 5, pp. 376–382, 2014.

[147] E. R. Stern, K. D. Fitzgerald, R. C. Welsh, J. L. Abelson, and S. F. Taylor, "Resting-state functional connectivity between fronto-parietal and default mode networks in obsessive-compulsive disorder," *PloS One*, vol. 7, no. 5, pp. e36356, 2012.

[148] J. Hou, L. Song, W. Zhang, et al., "Morphologic and functional connectivity alterations of corticostriatal and default mode network in treatment-naive patients with obsessive-compulsive disorder," *PloS One*, vol. 8, no. 12, pp. e83931, 2013.

[149] P. T. Bell and J. M. Shine, "Estimating large-scale network convergence in the human functional connectome," *Brain Connectivity*, vol. 5, no. 9, pp. 565–574, 2015.

[150] R. Yuan, X. Di, P. A. Taylor, S. Gohel, Y.-H. Tsai, and B. Biswal, "Functional topography of the thalamocortical system in human," *Brain Structure and Function*, vol. 221, no. 4, pp. 1971–1984, 2016.

[151] S. L. Bressler and V. Menon, "Large-scale brain networks in cognition: emerging methods and principles," *Trends in Cognitive Sciences*, vol. 14, no. 6, pp. 277–290, 2010.

[152] V. Riedl, L. Utz, G. Castrillón, T. Grimmer, J. P. Rauschecker, M. Ploner, K. J. Friston, A. Drzezga, and C. Sorg, "Metabolic connectivity mapping reveals effective connectivity in the resting human brain," *Proceedings of the National Academy of Sciences*, vol. 113, no. 2, pp. 428–433, 2016.

[153] L. Heine, A. Soddu, F. Gómez, A. Vanhaudenhuyse, L. Tshibanda, M. Thonnard, V. Charland-Verville, M. Kirsch, S. Laureys, and A. Demertzi, "Resting state networks and consciousness," *Frontiers in Psychology*, vol. 3, pp. 295, 2012.

[154] B. T. Yeo, F. M. Krienen, J. Sepulcre, et al., "The organization of the human cerebral cortex estimated by intrinsic functional connectivity," *Journal of neurophysiology*, vol. 106, no. 3, pp. 1125–1165, 2011.

[155] G. Nestadt, V. Kamath, B. S. Maher, and Others, "Doubt and the decision-making process in obsessive-compulsive disorder," *Medical Hypotheses*, vol. 96, pp. 1–4, 2016.

[156] Y.-H. Chen, S.-F. Li, D. Lv, G.-D. Zhu, Y.-H. Wang, X. Meng, Q. Hu, C.-C. Li, L.-T. Zhang, X.-P. Chu, et al., "Decreased intrinsic functional connectivity of the salience network in drug-naive patients with obsessive-compulsive disorder," *Frontiers in Neuroscience*, vol. 12, pp. 889, 2018.

[157] J. Fasching, N. Walczak, G. A. Bernstein, et al., "Automated coding of activity videos from an ocd study," in *2016 IEEE International Conference on Robotics and Automation (ICRA)*. IEEE, 2016, pp. 5638–5643.

[158] H. Kashyap, J. K. Kumar, T. Kandavel, and Y.C. Reddy, "Neuropsychological functioning in obsessive-compulsive disorder: are executive functions the key deficit?," *Comprehensive Psychiatry*, vol. 54, no. 5, pp. 533–540, 2013.

[159] S. Bannon, C. J. Gonsalvez, R. J. Croft, and P. M. Boyce, "Executive functions in obsessive–compulsive disorder: state or trait deficits?," *Australian and New Zealand Journal of Psychiatry*, vol. 40, no. 11-12, pp. 1031–1038, 2006.

[160] J. G. Modell, J. M. Mountz, G. C. Curtis, and J. F. Greden, "Neurophysiologic dysfunction in basal ganglia/limbic striatal and thalamocortical circuits as a pathogenetic mechanism of obsessive-compulsive disorder.," *The Journal of Neuropsychiatry and Clinical Neurosciences*, 1989.

[161] S. Saxena and S. L. Rauch, "Functional neuroimaging and the neuroanatomy of obsessive-compulsive disorder," *Psychiatric Clinics of North America*, vol. 23, no. 3, pp. 563–586, 2000.

[162] S. A. Sheth, J. Neal, F. Tangherlini, M. K. Mian, A. Gentil, G. R. Cosgrove, E. N. Eskandar, and D. D. Dougherty, "Limbic system surgery for treatment-refractory

obsessive-compulsive disorder: a prospective long-term follow-up of 64 patients," *Journal of Neurosurgery*, vol. 118, no. 3, pp. 491–497, 2013.

[163] E. Allen et al., "EEG signatures of dynamic functional network connectivity states," *Brain Topography*, vol. 31, no. 1, pp. 101–116, 2018.

[164] Y. Yang et al., "A state-space model of cross-region dynamic connectivity in MEG/EEG," in *Advances in Neural Information Processing Systems*, 2016, pp. 1234–1242.

[165] T. Roh et al., "A wearable neuro-feedback system with EEG-based mental status monitoring and transcranial electrical stimulation," *IEEE Transactions on Biomedical Circuits and Systems*, vol. 8, no. 6, pp. 755–764, 2014.

[166] Z. Zhang and K. Parhi, "Low-complexity seizure prediction from iEEG/sEEG using spectral power and ratios of spectral power," *IEEE Transactions on Biomedical Circuits and Systems*, vol. 10, no. 3, pp. 693–706, 2015.

[167] E. Al-sharoa et al., "Tensor based temporal and multilayer community detection for studying brain dynamics during resting state fMRI," *IEEE Transactions on Biomedical Engineering*, vol. 66, no. 3, pp. 695–709, 2018.

[168] C. Chang and G. H. Glover, "Time–frequency dynamics of resting-state brain connectivity measured with fMRI," *NeuroImage*, vol. 50, no. 1, pp. 81–98, 2010.

[169] R. Hutchison and J. Morton, "Tracking the brain's functional coupling dynamics over development," *Journal of Neuroscience*, vol. 35, no. 17, pp. 6849–6859, 2015.

[170] M. Yaesoubi et al., "Dynamic coherence analysis of resting fMRI data to jointly capture state-based phase, frequency, and time-domain information," *NeuroImage*, vol. 120, pp. 133–142, 2015.

[171] K. Hilger, M. Fukushima, et al., "Temporal stability of functional brain modules associated with human intelligence," *Human brain mapping*, vol. 41, no. 2, pp. 362–372, 2020.

[172] T. Chen et al., "Distinct global brain dynamics and spatiotemporal organization of the salience network," *PLoS Biology*, vol. 14, no. 6, 2016.

[173] Y. Du et al., "Interaction among subsystems within default mode network diminished in schizophrenia patients: a dynamic connectivity approach," *Schizophrenia Research*, vol. 170, no. 1, pp. 55–65, 2016.

[174] J. Su et al., "Heredity characteristics of schizophrenia shown by dynamic functional connectivity analysis of resting-state functional MRI scans of unaffected siblings," *Neuroreport*, vol. 27, no. 11, pp. 843–848, 2016.

[175] E. Damaraju et al., "Dynamic functional connectivity analysis reveals transient states of dysconnectivity in schizophrenia," *NeuroImage: Clinical*, vol. 5, pp. 298–308, 2014.

[176] S. Menon and K. Krishnamurthy, "A comparison of static and dynamic functional connectivities for identifying subjects and biological sex using intrinsic individual brain connectivity," *Scientific Reports*, vol. 9, no. 1, pp. 1–11, 2019.

[177] B. Cai et al., "A GICA-TVGL framework to study sex differences in resting state fMRI dynamic connectivity," *Journal of Neuroscience Methods*, vol. 332, pp. 108531, 2020.

[178] Y. Du, S. Fryer, et al., "Dynamic functional connectivity impairments in early schizophrenia and clinical high-risk for psychosis," *NeuroImage*, vol. 180, pp. 632–645, 2018.

[179] A. Fong et al., "Dynamic functional connectivity during task performance and rest predicts individual differences in attention across studies," *NeuroImage*, vol. 188, pp. 14–25, 2019.

[180] B. Sen and K. Parhi, "Predicting male vs. female from task-fMRI brain connectivity," in *2019 41st Annual International Conference of the IEEE Engineering in Medicine and Biology Society (EMBC)*. IEEE, 2019, pp. 4089–4092.

[181] A. Greene et al., "Task-induced brain state manipulation improves prediction of individual traits," *Nature Communications*, vol. 9, no. 1, pp. 1–13, 2018.

[182] L. Hearne et al., "Functional brain networks related to individual differences in human intelligence at rest," *Scientific Reports*, vol. 6, pp. 32328, 2016.

[183] L. Yao et al., "Resting tremor detection in parkinson's disease with machine learning and kalman filtering," in *2018 IEEE Biomedical Circuits and Systems Conference (BioCAS)*, 2018, pp. 1–4.

[184] D. I. Miller and D. F. Halpern, "The new science of cognitive sex differences," *Trends in Cognitive Sciences*, vol. 18, no. 1, pp. 37–45, 2014.

[185] J. M. Duarte-Carvajalino et al., "Hierarchical topological network analysis of anatomical human brain connectivity and differences related to sex and kinship," *NeuroImage*, vol. 59, no. 4, pp. 3784–3804, 2012.

[186] C. Zhang et al., "Functional connectivity predicts gender: evidence for gender differences in resting brain connectivity," *Human Brain Mapping*, vol. 39, no. 4, pp. 1765–1776, 2018.

[187] J. Zhang et al., "Gender differences in global functional connectivity during facial emotion processing: A visual MMN study," *Frontiers in Behavioral Neuroscience*, vol. 12, 2018.

[188] R. Bluhm et al., "Default mode network connectivity: effects of age, sex, and analytic approach," *Neuroreport*, vol. 19, no. 8, pp. 887–891, 2008.

[189] E. Allen et al., "A baseline for the multivariate comparison of resting-state networks," *Frontiers in Systems Neuroscience*, vol. 5, pp. 2, 2011.

[190] M. Ingalhalikar et al., "Sex differences in the structural connectome of the human brain," *Proceedings of the National Academy of Sciences*, vol. 111, no. 2, pp. 823–828, 2014.

[191] E. Finn et al., "Functional connectome fingerprinting: identifying individuals using patterns of brain connectivity," *Nature Neuroscience*, vol. 18, no. 11, pp. 1664, 2015.

[192] J. Dubois et al., "A distributed brain network predicts general intelligence from resting-state human neuroimaging data," *Philosophical Transactions of the Royal Society B: Biological Sciences*, vol. 373, no. 1756, pp. 20170284, 2018.

[193] C. Sripada et al., "Towards a " Treadmill Test" for cognition: Reliable prediction of intelligence from whole-brain task activation patterns," *BioRxiv*, p. 412056, 2018.

[194] S. Ma et al., "Automatic identification of functional clusters in fmri data using spatial dependence," *IEEE Transactions on Biomedical Engineering*, vol. 58, no. 12, pp. 3406–3417, 2011.

[195] B. Cai et al., "Capturing dynamic connectivity from resting state fmri using time-varying graphical lasso," *IEEE Transactions on Biomedical Engineering*, vol. 66, no. 7, pp. 1852–1862, 2018.

[196] N. D. Sidiropoulos, L. De Lathauwer, X. Fu, K. Huang, E. E. Papalexakis, and C. Faloutsos, "Tensor decomposition for signal processing and machine learning," *IEEE Transactions on Signal Processing*, vol. 65, no. 13, pp. 3551–3582.

[197] R. Bro, "PARAFAC. Tutorial and applications," in *Chemometrics and intelligent laboratory systems*, 1997, vol. 38(2), pp. 149–171.

[198] T. Jiang and N. D. Sidiropoulos, "Kruskal's permutation lemma and the identification of CANDECOMP/PARAFAC and bilinear models with constant modulus constraints," *IEEE Transactions on Signal Processing*, vol. 52, no. 9, pp. 2625–2636, 2004.

[199] N. Leonardi, J. Richiardi, et al., "Principal components of functional connectivity: a new approach to study dynamic brain connectivity during rest," *NeuroImage*, vol. 83, pp. 937–950, 2013.

[200] P. H. Schönemann, "A generalized solution of the orthogonal procrustes problem," *Psychometrika*, vol. 31, no. 1, pp. 1–10, 1966.

[201] A. C. Aitken, "On least squares and linear combination of observations," *Proceedings of the Royal Society of Edinburgh*, vol. 55, pp. 42–48, 1936.

[202] C. Lawson and R. Hanson, *Solving least squares problems*, vol. 15, Siam, 1995.

[203] F. Mokhtari et al., "Dynamic functional magnetic resonance imaging connectivity tensor decomposition: A new approach to analyze and interpret dynamic brain connectivity," *Brain Connectivity*, vol. 9, no. 1, pp. 95–112, 2019.

[204] M. Sørensen et al., "Canonical polyadic decomposition with a columnwise orthonormal factor matrix," *SIAM Journal on Matrix Analysis and Applications*, vol. 33, no. 4, pp. 1190–1213, 2012.

[205] D. P. Bertsekas, "Nonlinear Programming: Second Edition," *Athena Scientific*, 1999.

[206] P. Comon et al., "Tensor decompositions, alternating least squares and other tales," *Journal of Chemometrics: A Journal of the Chemometrics Society*, vol. 23, no. 7-8, pp. 393–405, 2009.

[207] L. Grippo and M. Sciandrone, "On the convergence of the block nonlinear Gauss–Seidel method under convex constraints," *Operations Research Letters*, vol. 26, no. 3, pp. 127–136, 2000.

[208] W. Bilker et al., "Development of abbreviated nine-item forms of the raven's standard progressive matrices test," *Assessment*, vol. 19, no. 3, pp. 354–369, 2012.

[209] N. Leonardi and D. Van De Ville, "On spurious and real fluctuations of dynamic functional connectivity during rest," *NeuroImage*, vol. 104, pp. 430–436, 2015.

[210] L. Tian et al., "Hemisphere-and gender-related differences in small-world brain networks: a resting-state functional MRI study," *NeuroImage*, vol. 54, no. 1, pp. 191–202, 2011.

[211] S. Arlot et al., "A survey of cross-validation procedures for model selection," *Statistics Surveys*, vol. 4, pp. 40–79, 2010.

[212] J. Power et al., "Functional network organization of the human brain," *Neuron*, vol. 72, no. 4, pp. 665–678, 2011.

[213] T. Ohtani et al., "Medial frontal white and gray matter contributions to general intelligence," *PLoS One*, vol. 9, no. 12, 2014.

[214] E. Genç et al., "Diffusion markers of dendritic density and arborization in gray matter predict differences in intelligence," 2018.

[215] K. Narr et al., "Relationships between iq and regional cortical gray matter thickness in healthy adults," *Cerebral Cortex*, vol. 17, no. 9, pp. 2163–2171, 2007.

[216] G. Pamplona et al., "Analyzing the association between functional connectivity of the brain and intellectual performance," *Frontiers in Human Neuroscience*, vol. 9, pp. 61, 2015.

[217] J. Gläscher et al., "Distributed neural system for general intelligence revealed by lesion mapping," *Proceedings of the National Academy of Sciences*, vol. 107, no. 10, pp. 4705–4709, 2010.

[218] E. Santarnecchi et al., "Network connectivity correlates of variability in fluid intelligence performance," *Intelligence*, vol. 65, pp. 35–47, 2017.

[219] A. K. Barbey, "Network neuroscience theory of human intelligence," *Trends in Cognitive Sciences*, vol. 22, no. 1, pp. 8–20, 2018.

[220] H. Ritchie and M. Roser, "Mental health," *Our World in Data*, 2019, https://ourworldindata.org/mental-health.

[221] B. Sen, N. Borle, R. Greiner, and M. Brown, "A general prediction model for the detection of adhd and autism using structural and functional mri," *PloS One*, vol. 13, no. 4, 2018.

[222] K. R. Cullen et al., "Abnormal amygdala resting-state functional connectivity in adolescent depression," *JAMA psychiatry*, vol. 71, no. 10, pp. 1138–1147, 2014.

[223] E. Poznanski and H. Mokros, *Children's depression rating scale, revised (CDRS-R)*, Western Psychological Services Los Angeles, 1996.

[224] A. Beck et al., "Beck depression inventory-ii," *San Antonio*, vol. 78, no. 2, pp. 490–498, 1996.

[225] D. Watson, M. W. O'hara, et al., "Development and validation of the inventory of depression and anxiety symptoms (IDAS)," *Psychological Assessment*, vol. 19, no. 3, pp. 253, 2007.

[226] M. J. Tobia, K. Hayashi, G. Ballard, I. Gotlib, and C. E. Waugh, "Dynamic functional connectivity and individual differences in emotions during social stress," *Human Brain Mapping*, vol. 38, no. 12, pp. 6185–6205, 2017.

[227] L. Schmaal, D.P. Hibar, et al., "Cortical abnormalities in adults and adolescents with major depression based on brain scans from 20 cohorts worldwide in the enigma major depressive disorder working group," *Molecular Psychiatry*, vol. 22, no. 6, pp. 900, 2017.

[228] W. C. Drevets, J. Savitz, and M. Trimble, "The subgenual anterior cingulate cortex in mood disorders," *CNS Spectrums*, vol. 13, no. 8, pp. 663, 2008.

[229] C. Zhuo, G. Li, X. Lin, D. Jiang, Y. Xu, H. Tian, W. Wang, and X. Song, "The rise and fall of mri studies in major depressive disorder," *Translational Psychiatry*, vol. 9, no. 1, pp. 1–14, 2019.

[230] Q. Jiao, J. Ding, G. Lu, et al., "Increased activity imbalance in fronto-subcortical circuits in adolescents with major depression," *PloS One*, vol. 6, no. 9, 2011.

[231] C. Jin, C. Gao, C. Chen, S. Ma, R. Netra, Y. Wang, M. Zhang, and D. Li, "A preliminary study of the dysregulation of the resting networks in first-episode medication-naive adolescent depression," *Neuroscience Letters*, vol. 503, no. 2, pp. 105–109, 2011.

[232] K. Luking, G. Repovs, A. Belden, M. Gaffrey, K. Botteron, J. Luby, and D. Barch, "Functional connectivity of the amygdala in early-childhood-onset depression," *Journal of the American Academy of Child & Adolescent Psychiatry*, vol. 50, no. 10, pp. 1027–1041, 2011.

[233] M. L. Phillips, W. C. Drevets, S. L. Rauch, and R. Lane, "Neurobiology of emotion perception i: The neural basis of normal emotion perception," *Biological Psychiatry*, vol. 54, no. 5, pp. 504–514, 2003.

[234] W. C. Drevets, "Prefrontal cortical-amygdalar metabolism in major depression," *Annals of the New York Academy of Sciences*, vol. 877, no. 1, pp. 614–637, 1999.

[235] L. A. Hulvershorn, K. Cullen, and A. Anand, "Toward dysfunctional connectivity: a review of neuroimaging findings in pediatric major depressive disorder," *Brain Imaging and Behavior*, vol. 5, no. 4, pp. 307–328, 2011.

[236] K. R. Cullen, D. G. Gee, B. Klimes-Dougan, V. Gabbay, L. Hulvershorn, B. A. Mueller, J. Camchong, C. J. Bell, A. Houri, S. Kumra, et al., "A preliminary study of functional connectivity in comorbid adolescent depression," *Neuroscience Letters*, vol. 460, no. 3, pp. 227–231, 2009.

[237] M. Gaffrey, J. Luby, G. Repovš, A. Belden, K. Botteron, K. Luking, and D. Barch, "Subgenual cingulate connectivity in children with a history of preschool-depression," *Neuroreport*, vol. 21, no. 18, pp. 1182, 2010.

[238] M. Gaffrey, J. Luby, K. Botteron, G. Repovš, and D. Barch, "Default mode network connectivity in children with a history of preschool onset depression," *Journal of Child Psychology and Psychiatry*, vol. 53, no. 9, pp. 964–972, 2012.

[239] M. Oldehinkel, W. Francx, C. Beckmann, J. Buitelaar, and M. Mennes, "Resting state fmri research in child psychiatric disorders," *European Child & Adolescent Psychiatry*, vol. 22, no. 12, pp. 757–770, 2013.

[240] G. S. Dichter, D. Gibbs, and M. J. Smoski, "A systematic review of relations between resting-state functional-mri and treatment response in major depressive disorder," *Journal of Affective Disorders*, vol. 172, pp. 8–17, 2015.

[241] T. Wise, L. Marwood, A. Perkins, A. Herane-Vives, R. Joules, D. J. Lythgoe, W. M. Luh, S. Williams, A. Young, A. Cleare, et al., "Instability of default mode network connectivity in major depression: a two-sample confirmation study," *Translational Psychiatry*, vol. 7, no. 4, pp. e1105–e1105, 2017.

[242] L. Hall et al., "An fmri study of emotional face processing in adolescent major depression," *Journal of Affective Disorders*, vol. 168, pp. 44–50, 2014.

[243] R. H. Kaiser, J. R Andrews-Hanna, T. Wager, and D. A. Pizzagalli, "Large-scale network dysfunction in major depressive disorder: a meta-analysis of resting-state functional connectivity," *JAMA Psychiatry*, vol. 72, no. 6, pp. 603–611, 2015.

[244] H. Karim, C. Andreescu, D. Tudorascu, S. F. Smagula, M. A. Butters, J. F. Karp, C. Reynolds, and H. Aizenstein, "Intrinsic functional connectivity in late-life depression: trajectories over the course of pharmacotherapy in remitters and non-remitters," *Molecular Psychiatry*, vol. 22, no. 3, pp. 450–457, 2017.

Appendix A

Supplementary Information for Chapter 2

The Supplementary Information contains twelve Subsections. Subsection S.1 provides pipeline for the ranking process. Subsection S.2 illustrates the important regions and edges for different task conditions. Subsection S.3 illustrates the ROC curves for classification performance. Subsection S.4 lists edges based on differential edge entropy and lists ranked regions by state-of-the-art centrality measures. Subsection S.5 shows the histograms of occurrences for regions and edges. Subsection S.6 shows distribution of accuracy values during a permutation test. Subsection S.7 compares graph entropy with structural centrality. Subsection S.8 contains images containing comparison of graph entropy and sub-graph (intersection and union of top regions and edges) entropies between two groups. Subsection S.9 describes the details about the atlas used in this paper. Subsection S.10 shows that maximizing *sub-graph* entropy is equivalent to maximizing mutual information. Subsection S.11 contains a theoretical justification for using sample average entropy as proxy for group entropy. Subsection S.12 provides a justification of using absolute correlation as edge weights.

S.1: Pipeline for Ranking of Regions and Edges

This subsection illustrates the pipeline for ranking procedure of nodes and edges.

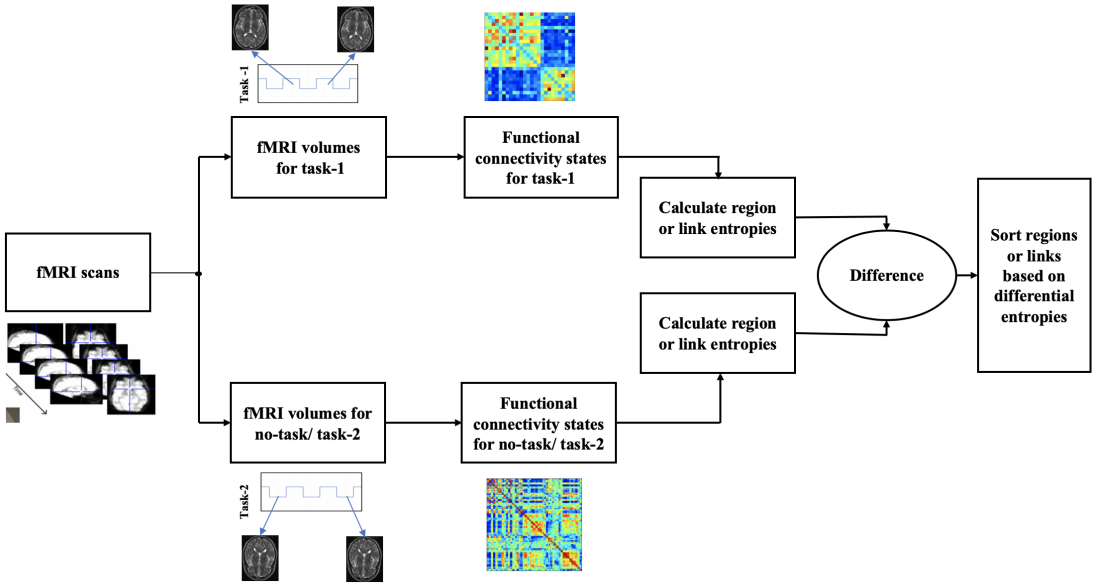

Figure A.1: Pipeline for ranking of regions and edges. After parcellating fMRI scans into regions, *sub-graph* entropies (region and edge entropies) are calculated for each subject's functional network. These differential entropies are then used for ranking the regions and edges.

S.2: Important Regions and Edges

This subsection demonstrates the important nodes and edges for different *states*.

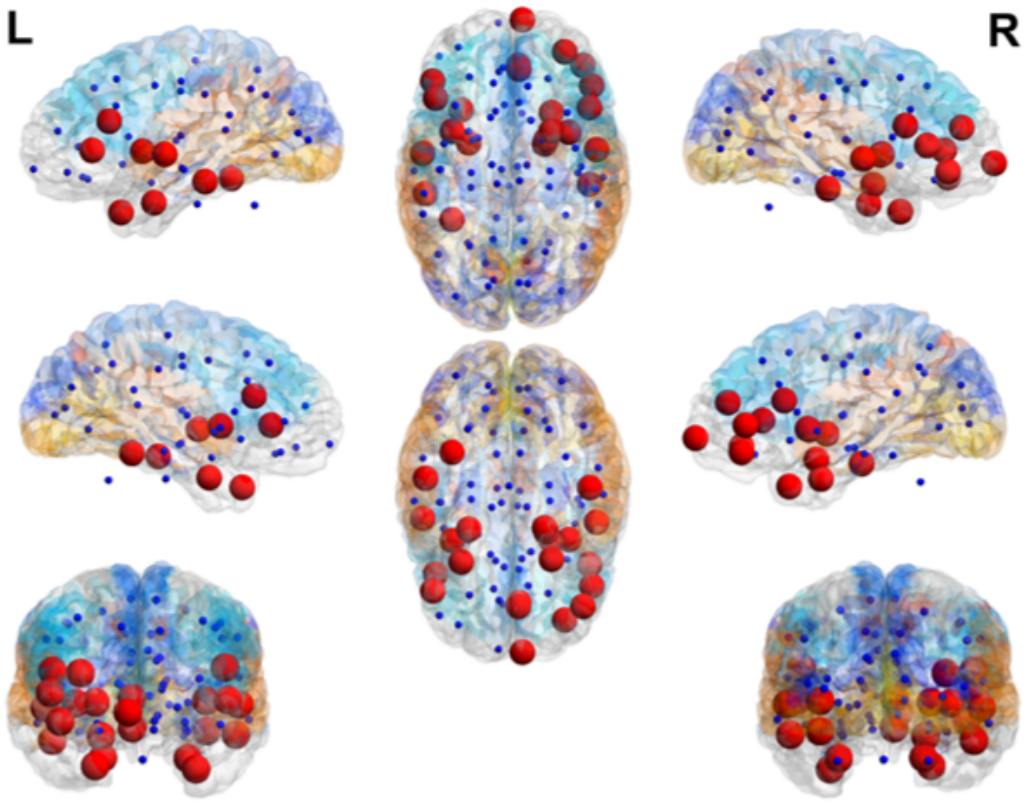

Figure A.2: Visualization of important regions within brain. These regions carry the highest entropies within the functional network related to a *task* representing emotion task. The regional importance is shown by the size of spheres. Top-25 regions are shown in *red*. All regions are at least 2-standard deviations away from mean entropy.

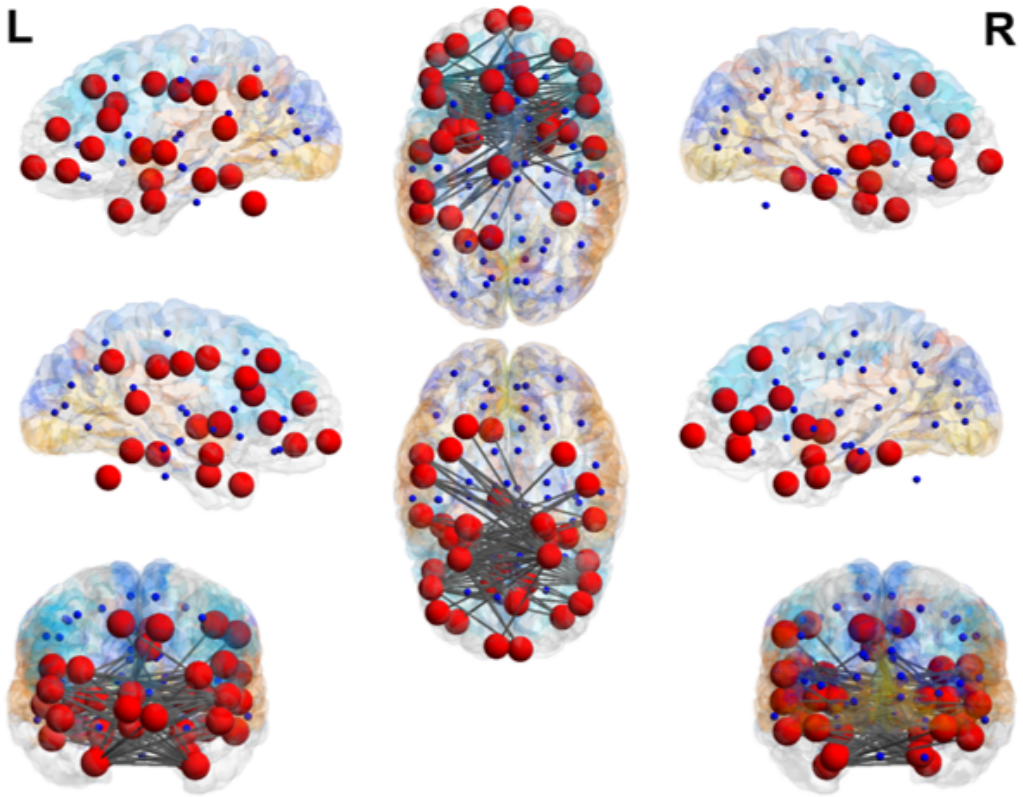

Figure A.3: Visualization of important edges within brain for emotion task. These edges carry the highest entropies within the functional network related to a *task*. The regional importance is shown by the size of spheres. Top-25 regions that are at least 2-standard deviations away from mean entropy are shown in *red*.

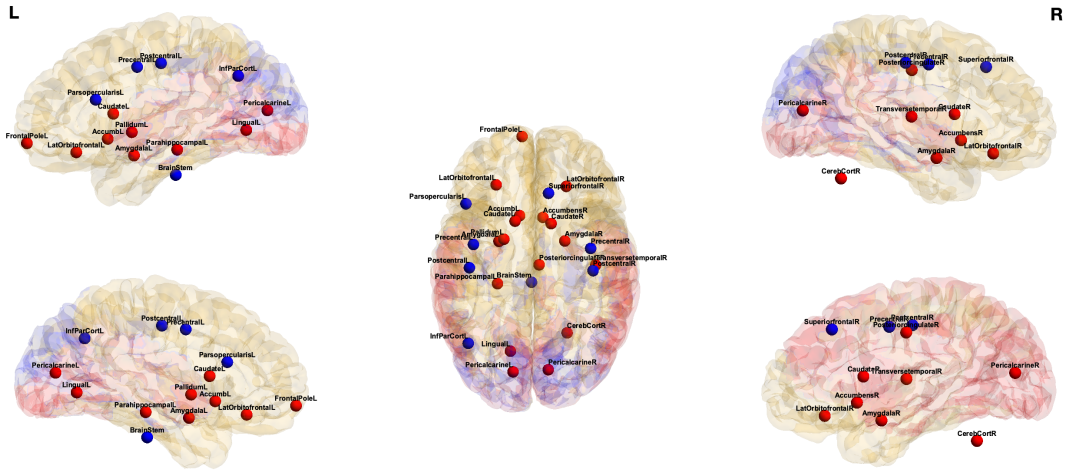

Figure A.4: Visualization of *important* regions that have highest differential entropy between two *states* for gambling task *vs.* no-task. *Red:* regions that have higher node entropy during gambling task, *blue:* regions that have higher node entropy during no-task.

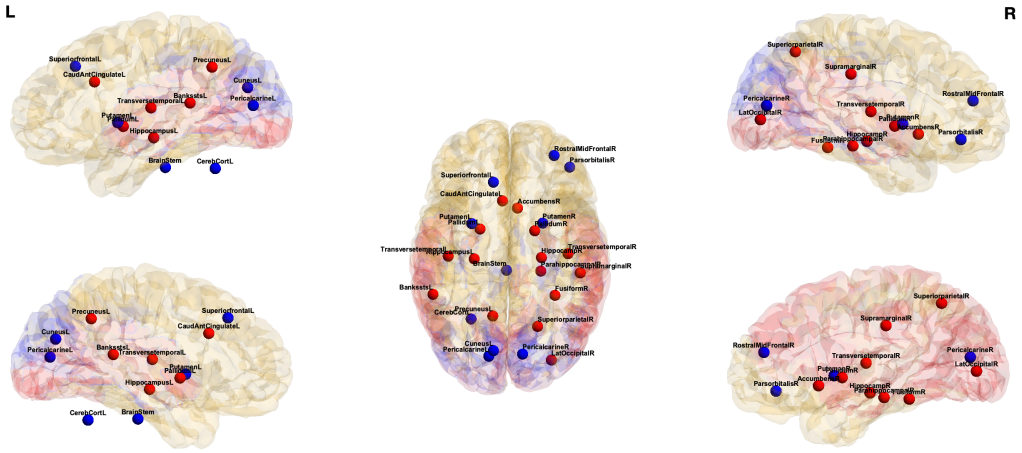

Figure A.5: Visualization of *important* regions that have highest differential entropy between two *states* for emotion *vs.* gambling task. *Red:* regions that have higher node entropy during emotion task, *blue:* regions that have higher node entropy during gambling task.

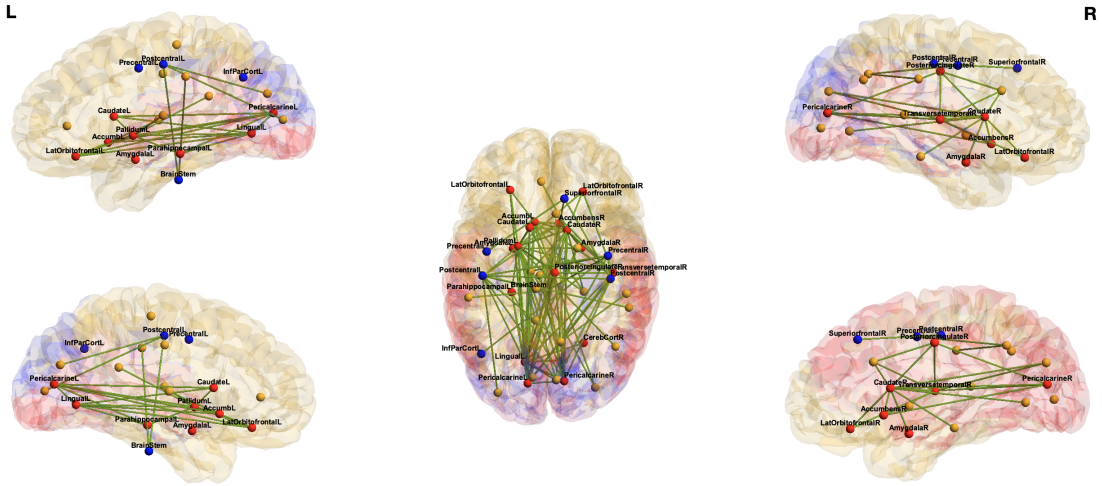

Figure A.6: Visualization of *important* edges that have highest differential entropy between two *states* for gambling task *vs.* no-task. *Red:* regions that have higher node entropy during gambling task, *blue:* regions that have higher node entropy during no-task, *yellow:* regions that are not significant based on only node entropy.

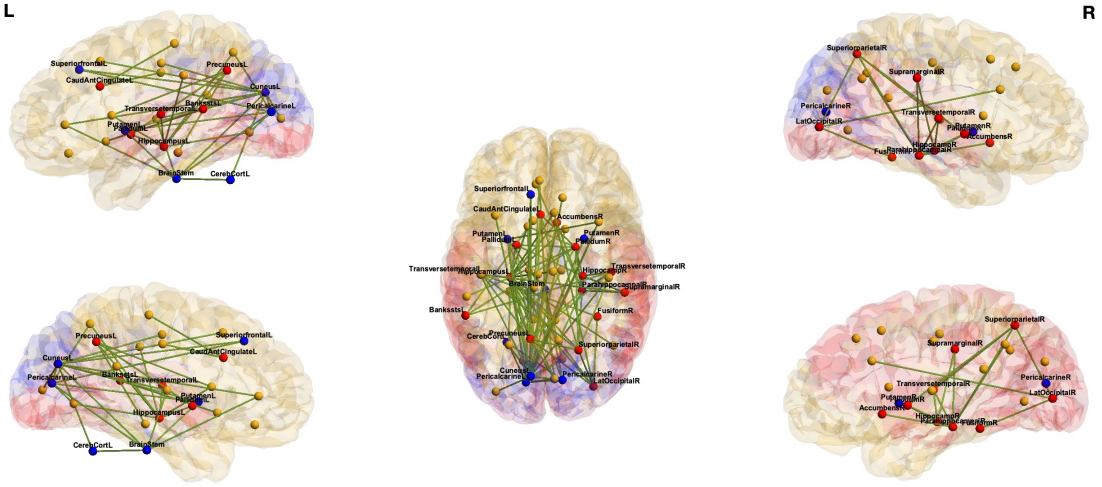

Figure A.7: Visualization of *important* edges that have highest differential entropy between two *states* for emotion *vs.* gambling task. *Red:* regions that have higher node entropy during emotion task, *blue:* regions that have higher node entropy during gambling, *yellow:* regions that are not significant based on only node entropy.

S.3: ROC curve for classification

This subsection compares the Receiver Operating Characteristic (ROC) curves for different classification tasks.

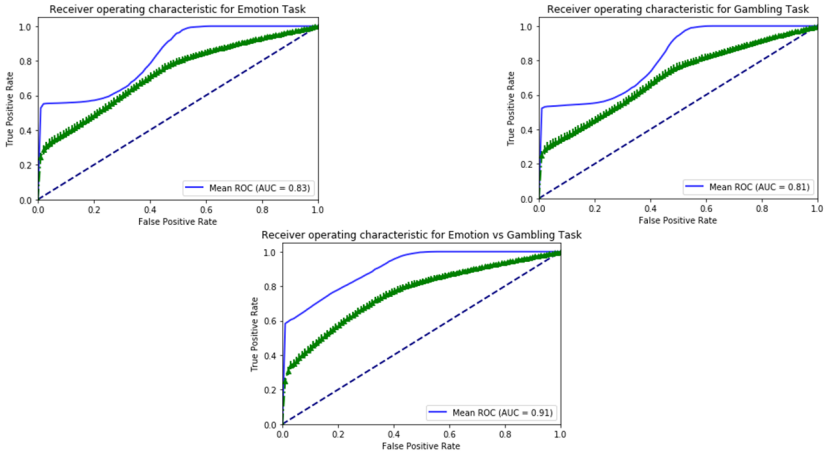

Figure A.8: ROC curve for region based centrality. *blue:* ROC curve using sub - graph entropy, *green:* mean ROC curve using 4-centrality measures: *degree*, *eigenvector*, *betweenness*, *leverage*, *blue broken:* random guessing using ROC baseline.

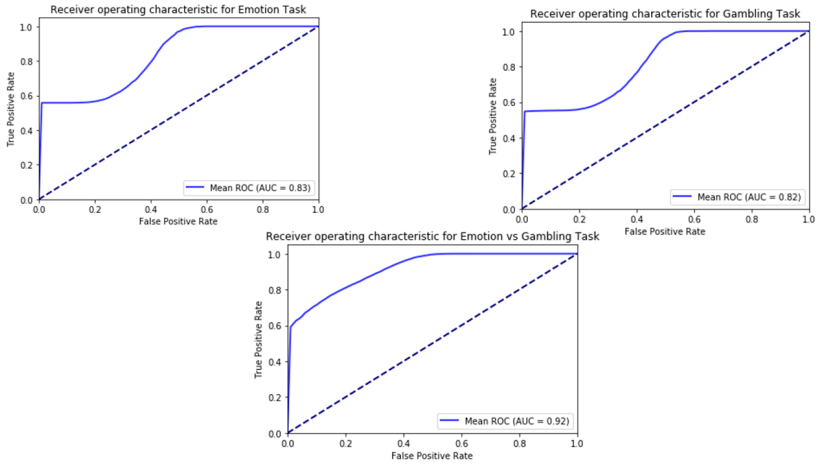

Figure A.9: ROC curve for edge based centrality: *blue:* ROC curve using *sub-graph* entropy, *blue broken:* ROC baseline using random guessing.

S.4: Edge Ranking Based on Differential Entropy

This subsection lists the edges ranked according to their differential entropy.

Table A.1: Edge ranking

Emotion *vs.* No-task			Gambling *vs.* No-task		
Edges		Entropy	Edges		Entropy
ctx_lh_pericalcarine	ctx_rh_pericalcarine	0.1917	Left_Pallidum	Right_Caudate	0.1834
ctx_lh_pericalcarine	ctx_lh_superiorparietal	0.1884	ctx_lh_lingual	ctx_lh_pericalcarine	0.1816
ctx_lh_superiorparietal	ctx_rh_superiorparietal	0.1838	ctx_rh_lateralorbitofrontal	ctx_rh_transversetemporal	0.1758
ctx_lh_superiorparietal	ctx_rh_pericalcarine	0.1843	Left_Accumbens_area	ctx_rh_transversetemporal	0.1647
ctx_lh_pericalcarine	ctx_rh_superiorparietal	0.1778	Left_Caudate	ctx_lh_pericalcarine	0.1641
Right_Pallidum	ctx_lh_isthmuscingulate	0.1997	Left_Accumbens_area	ctx_rh_parahippocampal	0.1613
ctx_rh_pericalcarine	ctx_rh_superiorparietal	0.1495	Left_Pallidum	ctx_lh_pericalcarine	0.1605
Right_Thalamus_Proper	ctx_lh_superiorparietal	0.1431	Left_Caudate	Left_Pallidum	0.1562
ctx_lh_pericalcarine	ctx_rh_lingual	0.1406	ctx_lh_pericalcarine	ctx_rh_transversetemporal	0.15422
ctx_lh_superiorparietal	ctx_rh_lingual	0.1404	ctx_lh_postcentral	ctx_rh_precuneus	0.1515
ctx_lh_pericalcarine	ctx_rh_cuneus	0.1384	Left_Pallidum	ctx_lh_lingual	0.1487
Left_Accumbens_area	Right_Pallidum	0.1382	Left_Caudate	Right_Caudate	0.1484
Right_Caudate	Right_Pallidum	0.1335	Right_Caudate	ctx_rh_parahippocampal	0.1468
ctx_lh_rostralanteriorcingulate	ctx_lh_superiorparietal	0.1312	Left_Accumbens_area	ctx_lh_pericalcarine	0.1463
ctx_lh_parahippocampal	ctx_rh_transversetemporal	0.1303	Left_Accumbens_area	Right_Accumbens_area	0.1443
ctx_lh_isthmuscingulate	ctx_rh_transversetemporal	0.1293	Left_Accumbens_area	Right_Caudate	0.1436
Right_Caudate	ctx_rh_transversetemporal	0.1285	Left_Pallidum	Left_Accumbens_area	0.1424
Right_Caudate	ctx_rh_parahippocampal	0.1273	Left_Pallidum	ctx_rh_cuneus	0.1398
Left_Hippocampus	Right_Pallidum	0.1268	Left_Pallidum	ctx_rh_transversetemporal	0.1392
Left_Hippocampus	ctx_rh_transversetemporal	0.1247	Right_Pallidum	ctx_lh_lingual	0.1391
ctx_rh_lingual	ctx_rh_pericalcarine	0.1240	Left_Pallidum	ctx_lh_parahippocampal	0.1390
ctx_rh_caudalanteriorcingulate	ctx_rh_transversetemporal	0.1228	ctx_lh_lateraloccipital	ctx_lh_postcentral	0.1388
ctx_lh_pericalcarine	ctx_rh_precuneus	0.1209	Right_Pallidum	ctx_lh_pericalcarine	0.1382
ctx_rh_lingual	ctx_rh_superiorparietal	0.1207	Left_Caudate	ctx_lh_lingual	0.1366
Left_Hippocampus	Left_Accumbens_area	0.1206	Right_Caudate	ctx_lh_pericalcarine	0.1357

Table A.2: Edge rank emotion *vs.* gambling

Emotion *vs.* Gambling		
Edges		Entropy
Brain_Stem	ctx_lh_pericalcarine	0.7195
ctx_lh_cuneus	ctx_lh_pericalcarine	0.6580
Left_Hippocampus	Right_Pallidum	0.5991
Brain_Stem	ctx_lh_cuneus	0.5920
Left_Hippocampus	ctx_rh_caudalanteriorcingulate	0.5830
Left_Pallidum	Right_Pallidum	0.5671
Left_Caudate	Left_Hippocampus	0.5614
ctx_lh_pericalcarine	ctx_rh_pericalcarine	0.5489
Left_Hippocampus	ctx_lh_precuneus	0.5439
Brain_Stem	ctx_rh_lingual	0.5422
Left_Putamen	Brain_Stem	0.5317
Brain_Stem	ctx_rh_pericalcarine	0.5283
ctx_lh_cuneus	ctx_rh_pericalcarine	0.5147
ctx_lh_pericalcarine	ctx_lh_superiorfrontal	0.5099
ctx_lh_cuneus	ctx_lh_lateraloccipital	0.5054
Left_Hippocampus	Right_Accumbens_area	0.5026
Right_Hippocampus	ctx_rh_transversetemporal	0.4910
Right_Pallidum	ctx_rh_parahippocampal	0.4900
Left_Putamen	ctx_rh_pericalcarine	0.4800
Left_Hippocampus	ctx_lh_transversetemporal	0.4758
ctx_lh_cuneus	ctx_lh_lingual	0.4605
Left_Hippocampus	ctx_rh_lateraloccipital	0.4599
Left_Hippocampus	Right_Caudate	0.4597
ctx_lh_cuneus	ctx_lh_postcentral	0.4578
ctx_lh_precuneus	ctx_lh_transversetemporal	0.4561

Table A.3: Significant regions extracted by other centrality measures between emotion *vs.* no-task.

Degree	Betweenness	Eigenvector	Leverage
PericalcarineL	PericalcarineL	AmygdalaR	AmygdalaR
SuperiorparietalL	PostcentralL	ParsopercularisL	PrecuneusL
FusiformR	PrecentralL	ParstriangularisL	FusiformR
PericalcarineR	PrecuneusL	PericalcarineL	HippocampusL
SuperiorparietalR	CuneusR	RostralMidFontalL	
RostralAntCingulateR	PericalcarineR	EntorhinalR	
	PrecuneusR	FusiformR	
		RostralAntCingulateR	
		RostralMidFrontalR	

Table A.4: Significant regions extracted by other centrality measures between gambling *vs.* no-task.

Degree	Betweenness	Eigenvector	Leverage
PallidumL	HippocampusL	BrainStem	AmygdalaR
AccumbL	CerebCortR	AccumbL	ParsopercularisL
CaudateR	CaudMidFrontalL	CaudateR	AccumbL
AmygdalaR	InfTempCortL	LingualL	ParsorbitalisR
AccumbensR	LatOrbitofrontalL	ParacentralL	HippocampusL
MidTemporalL	MedOrbitofrontalL	ParstriangularisL	
ParsopercularisL		InsulaL	
PostcentralL		FusiformR	
PrecentralR		InfTempCortR	
SuperiorfrontalR		ParsorbitalisR	

S.5. Histogram

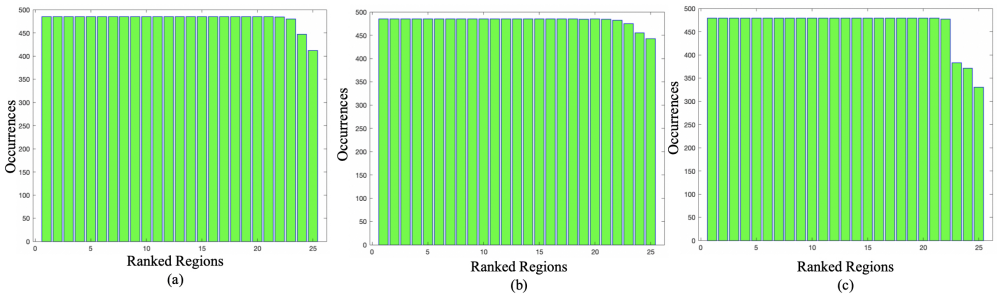

Figure A.10: Histograms of occurrence for top-25 regions during leave-one-out ranking procedure. Algorithm 3 was run 475 times, each time leaving one subject out. Occurrence of top-25 regions among top-25 regions are plotted. The number represents ranked regions in Table 2. (a) Emotion *vs.* no-task, (b) gambling *vs.* no-task, (c) emotion *vs.* gambling.

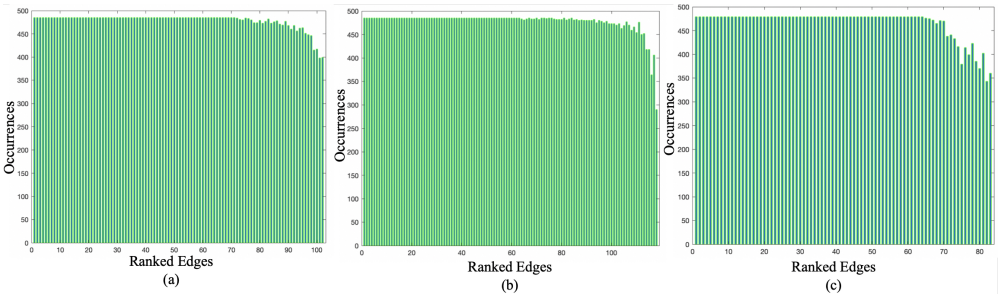

Figure A.11: Histograms of occurrence for significant edges during leave-one-out ranking procedure. Algorithm 3 was run 475 times, each time leaving one subject out. Occurrence of significant edges are plotted. Edge numbers represent ranked edges in Table S1 and Table S2 in this Supplementary Information. (a) Emotion *vs.* no-task, (b) gambling *vs.* no-task, (c) emotion *vs.* gambling.

S.6. Distribution of Accuracy Values

This subsection contains the histograms for performing permutation test on the three classification tasks.

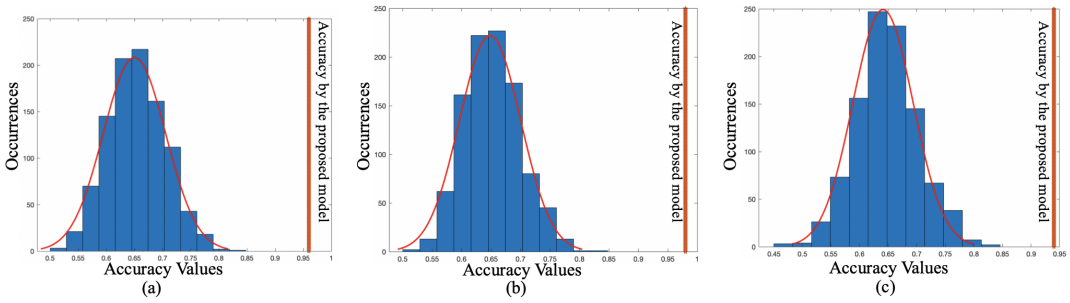

Figure A.12: Permutation tests by randomly assigning labels. Results from 1000 iterations are shown in histogram. Results from proposed model are shown in *red* bar. (a) Emotion *vs*. no-task, (b) gambling *vs*. no-task, (c) emotion *vs*. gambling.

S.7. Structural Centrality and Graph Entropy

Graph entropy is related to *structural centrality* of a graph. In order to investigate the relationship between the two metrics, we simulate 100,000 random graphs consisting of 85 nodes. The edge values are created based on a uniform distribution between 0-1. For each graph, we calculate both *structural centrality* and graph entropy; these are plotted in Fig. A.12. We also overlay the ranges for graph entropy for real brain graphs. These two quantities have an inverse relationship. As structural centrality of a graph increases, its entropy reduces. The opposite is true when entropy increases. A graph is more central and consists of one leader when entropy is less. On the other hand, the impact of nodes is more uniform when entropy of graph increases. Real fMRI datasets from Human Connectome Project consist of entropy values in the middle range.

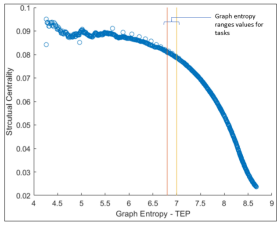

Figure A.13: Structural centrality *vs.* graph entropy. Here 100 thousands random graphs consisting of 85 nodes were created of varying centrality. Each node graph entropy and structural centrality were calculated and plotted. The boundary for highest and lowest value for entropies of human brain network is shown in yellow lines.

S.8. Comparison of Graph Entropy and Sub-graph Entropy between Two Groups

This subsection contains images containing comparison of graph entropy and sub-graph (intersection and union of top regions and edges) entropies between two groups.

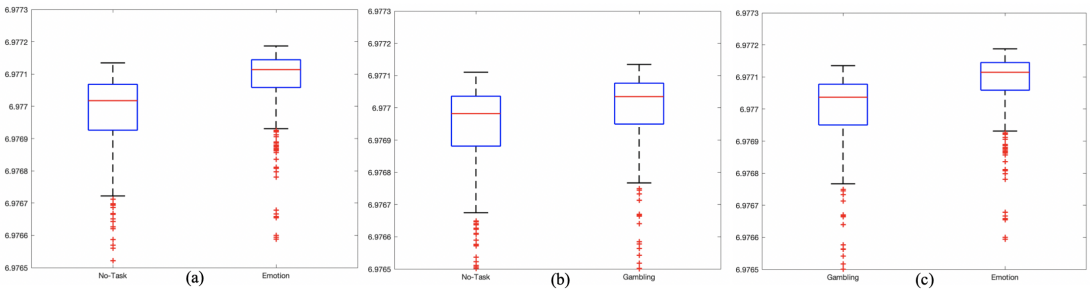

Figure A.14: Comparison of group-level mean values for graph entropy for whole graph between two *states*. a) Emotion *vs.* no-task, b) gambling *vs.* no-task, c) emotion *vs.* gambling. The graph entropies are calculated for each subject and *state*.

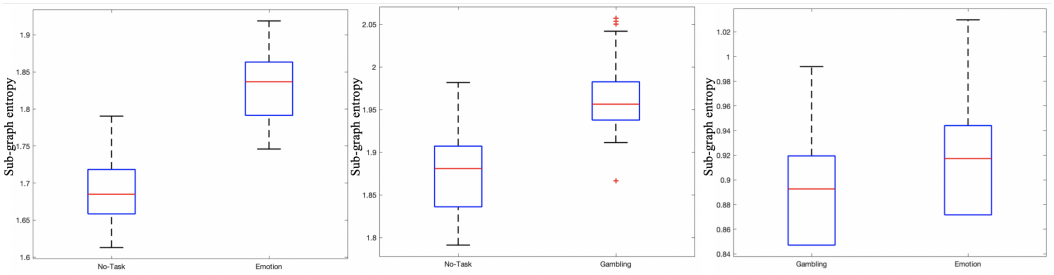

Figure A.15: *Sub-graph - 1*: Comparison of group-level mean values for *sub-graph* entropy for sub-network containing the *intersection* of top-25 regions and significant edges between two *states*. a) Emotion *vs*. no-task (54 edges), b) gambling *vs*. no-task (64 edges), c) emotion *vs*. gambling (17 edges). The graph entropies are calculated for each subject and *state*.

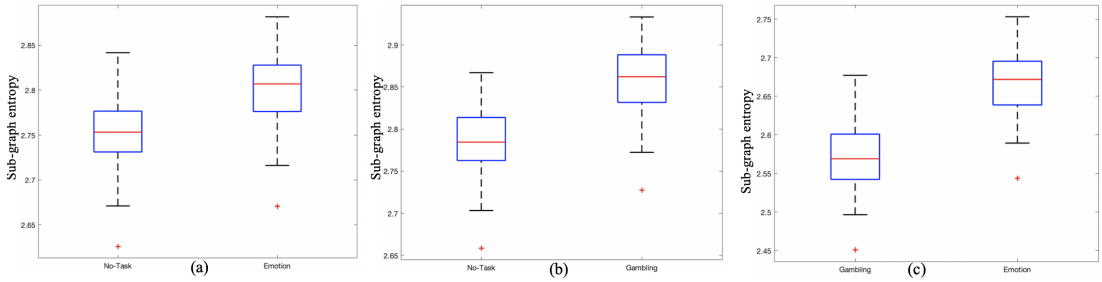

Figure A.16: *Sub-graph - 2*: Comparison of group-level mean values for *sub-graph* entropy for sub-network containing *union* of top-25 regions and significant edges between two *states*. a) Emotion *vs*. no-task (102 edges), b) gambling *vs*. no-task (118 edges), c) emotion *vs*. gambling (83 edges). The graph entropies are calculated for each subject and *state*.

S.9: Atlas Details

This section provides the details of Freesurfer atlas regions and their corresponding coordinates in MNI152 space.

Table A.5: Freesurfer Atlas Coordinates and Regions

X	Y	Z	Region
-22.43799052	-40.01410235	-49.10043329	Left_Cerebellum_Cortex
-9.365745637	2.239886304	-14.37367795	Left_Thalamus_Proper
-10.07260101	27.72348485	-12.26073232	Left_Caudate
-21.98422754	20.16952115	-20.84432891	Left_Putamen
-16.83028771	16.79043546	-23.15999222	Left_Pallidum
-0.075123916	-9.236922464	-48.42339352	Brain_Stem
-20.50547599	-2.062973884	-30.15532856	Left_Hippocampus
-19.81226823	15.48516687	-36.92135352	Left_Amygdala
-7.276182432	31.04307432	-27.10304054	Left_Accumbens_area
21.48534428	-39.86756307	-49.02782405	Right_Cerebellum_Cortex
9.483949985	2.061275227	-13.59662913	Right_Thalamus_Proper
11.78609914	26.20757004	-11.62715517	Right_Caudate
22.79048673	20.47876106	-20.71349558	Right_Putamen
17.75835396	15.67295792	-21.86726485	Right_Pallidum
22.00855593	-1.230696995	-31.1206177	Right_Hippocampus
20.08349546	15.711738	-37.17331388	Right_Amygdala
6.856174699	29.9811747	-26.78840361	Right_Accumbens_area
-46.56135363	-24.43048423	-8.671588408	ctx_lh_bankssts
-2.641475645	34.52602674	4.327244508	ctx_lh_caudalanteriorcingulate
-29.18799213	34.20815342	18.68062611	ctx_lh_caudalmiddlefrontal
-8.394193234	-59.99674691	0.810426155	ctx_lh_cuneus
-21.87644009	14.07402074	-47.78801843	ctx_lh_entorhinal
-30.9386489	-27.44044884	-34.66050092	ctx_lh_fusiform
-38.44759259	-46.19018519	10.055	ctx_lh_inferiorparietal
-45.16522307	-13.35528397	-36.35213969	ctx_lh_inferiortemporal
-6.797138047	-26.52777778	-0.606060606	ctx_lh_isthmuscingulate
-28.81817994	-68.91491475	-14.09027893	ctx_lh_lateraloccipital
-21.51043029	49.65374052	-35.04103453	ctx_lh_lateralorbitofrontal
-12.85870064	-50.95184803	-21.89164371	ctx_lh_lingual
-5.424302789	52.46314741	-33.96962151	ctx_lh_medialorbitofrontal
-51.38255075	-1.05607361	-29.19242037	ctx_lh_middletemporal
-20.70094021	-10.09763742	-33.50470106	ctx_lh_parahippocampal
-6.551643921	-8.080024814	28.71665633	ctx_lh_paracentral
-39.82481355	38.1677284	-3.969468614	ctx_lh_parsopercularis
-37.70623742	60.72183099	-31.45120724	ctx_lh_parsorbitalis
-41.22619629	47.33825684	-19.5916748	ctx_lh_parstriangularis
-11.2699553	-63.45146871	-10.27378672	ctx_lh_pericalcarine
-37.7076791	-0.500245339	17.57396958	ctx_lh_postcentral
-4.185311284	-0.283722438	12.20330739	ctx_lh_posteriorcingulate
-35.30378452	13.60621618	15.33101499	ctx_lh_precentral
-8.750484872	-38.07336113	13.38877036	ctx_lh_precuneus
-3.369775542	54.56656347	-17.64705882	ctx_lh_rostralanteriorcingulate
-27.43047381	65.73664656	-9.245512066	ctx_lh_rostralmiddlefrontal

X	Y	Z	Region
-27.43047381	65.73664656	-9.245512066	ctx_lh_rostralmiddlefrontal
-8.409821118	46.32435307	13.8764545	ctx_lh_superiorfrontal
-21.121497	-41.68930512	23.69906348	ctx_lh_superiorparietal
-46.72014687	8.292424968	-21.74289591	ctx_lh_superiortemporal
-46.00677227	-13.25964187	10.55130854	ctx_lh_supramarginal
-5.798690205	78.87528474	-29.70529613	ctx_lh_frontalpole
-25.94376504	31.79330393	-52.99268244	ctx_lh_temporalpole
-36.91558442	-0.342938312	-11.6599026	ctx_lh_transversetemporal
-30.75487945	20.2217279	-20.08969575	ctx_lh_insula
48.03367217	-19.09704574	-10.55749682	ctx_rh_bankssts
5.245158888	35.7336147	3.08031281	ctx_rh_caudalanteriorcingulate
31.32239106	30.37378154	20.14012328	ctx_rh_caudalmiddlefrontal
5.413062284	-61.50735294	2.649221453	ctx_rh_cuneus
19.14095007	13.38072122	-47.39684466	ctx_rh_entorhinal
30.54333274	-25.02878436	-34.88151553	ctx_rh_fusiform
40.10512232	-41.90762888	9.178134557	ctx_rh_inferiorparietal
43.5415707	-8.394461078	-39.20629894	ctx_rh_inferiortemporal
5.855446927	-27.09696728	-1.528830806	ctx_rh_isthmuscingulate
28.27539489	-65.8775836	-18.00317174	ctx_rh_lateraloccipital
21.03270609	48.73015873	-34.47388633	ctx_rh_lateralorbitofrontal
9.887762593	-49.87773888	-19.71100632	ctx_rh_lingual
4.966974573	55.82042114	-33.24071315	ctx_rh_medialorbitofrontal
50.85591502	-4.637917276	-30.79573414	ctx_rh_middletemporal
21.59495927	-9.769602851	-33.93711813	ctx_rh_parahippocampal
5.574623858	-6.455534659	29.1560317	ctx_rh_paracentral
43.43193444	33.05039788	-5.577159909	ctx_rh_parsopercularis
39.84943842	55.80170411	-30.06438807	ctx_rh_parsorbitalis
44.60538203	44.68959732	-16.17094734	ctx_rh_parstriangularis
10.07145966	-62.11767266	-9.486723738	ctx_rh_pericalcarine
37.2218269	-2.29390681	18.21908602	ctx_rh_postcentral
4.539522514	1.299480455	13.94575705	ctx_rh_posteriorcingulate
35.74047669	11.18046754	17.23375229	ctx_rh_precentral
7.952909887	-39.13619703	12.41339621	ctx_rh_precuneus
5.23004886	53.77137622	-18.7896987	ctx_rh_rostralanteriorcingulate
29.98936817	63.1596294	-6.599787363	ctx_rh_rostralmiddlefrontal
10.21130626	44.56652488	15.72779455	ctx_rh_superiorfrontal
19.52022891	-44.67677003	23.1629292	ctx_rh_superiorparietal
47.22200315	10.34015441	-23.27712519	ctx_rh_superiortemporal
46.5050845	-10.93363136	9.673192179	ctx_rh_supramarginal
7.123893805	80.40376106	-25.63053097	ctx_rh_frontalpole
22.85859073	30.3030888	-51.48117761	ctx_rh_temporalpole
38.81806931	1.170792079	-13.0730198	ctx_rh_transversetemporal
32.27828362	19.71071121	-21.13080728	ctx_rh_insula

S.10: Sample Average Entropy as Group Entropy

Theorem 1

Let H_{opt} be the group graph entropy for a unique state (task or no-task). Let H_k be the graph entropy for for k^{th} subject. We show that the sequence $\frac{1}{n}\sum_{k=1}^{n} H_k \rightarrow H_{opt}$ in probability. In other words, for any arbitrary small $\epsilon > 0$

$$\lim_{n\to\infty} P(|H_{opt} - \frac{1}{n}\sum_{k=1}^{n} H_k| > \epsilon) = 0 \tag{A.1}$$

Proof. Let Σ_{opt} be the corresponding adjacency matrix for H_{opt}. Here, the edge between regions (i, j) is given by $e_{i,j} = \sigma_{i,j} = \Sigma_{opt}(i, j)$. Let $G = (V, E)$, thus

$$q_{i,j} = \begin{cases} \frac{e_{ij}}{\sum(e_{ij}\in E)} \text{ when } i \neq j \\ 0 \text{ when } i = j \end{cases}$$

$$H_{opt} = \sum_{i,j} q_{i,j} \log_2(q_{i,j})$$

For k^{th} subject,

$$H_k = \sum_{i,j} q^k_{i,j} \log_2(q^k_{i,j})$$

It is clear that

$$\begin{aligned} |H_{opt} - \frac{1}{n}\sum_{k=1}^{n} H_k| &= |\sum_{i,j} q_{i,j} \log_2(q_{i,j}) - \frac{1}{n}\sum_{k=1}^{n}\sum_{i,j} q^k_{i,j} \log_2(q^k_{i,j})| \\ &= |\sum_{i,j}(q_{i,j} \log_2(q_{i,j}) - \frac{1}{n}\sum_{k=1}^{n} q^k_{i,j} \log_2(q^k_{i,j}))| \\ &\leq \sum_{i,j} |(q_{i,j} \log_2(q_{i,j}) - \frac{1}{n}\sum_{k=1}^{n} q^k_{i,j} \log_2(q^k_{i,j}))| \text{ according to cauchy schwarz inequality} \end{aligned} \tag{A.2}$$

From, Eqn. A.2 and A.1,

$$\lim_{n\to\infty} P(\sum_{i,j} |(q_{i,j}\log_2(q_{i,j}) - \frac{1}{n}\sum_{k=1}^{n} q_{i,j}^k \log_2(q_{i,j}^k))| > \epsilon) = 0 \rightarrow \lim_{n\to\infty} P(|H_{opt} - \frac{1}{n}\sum_{k=1}^{n} H_k| > \epsilon) = 0 \tag{A.3}$$

Let's see the result for (i, j). Using log-sum inequality,

$$\frac{1}{n}\sum_{k=1}^{n} q_{i,j}^k \log_2(q_{i,j}^k) \geq \frac{1}{n}\sum_{k=1}^{n} q_{i,j}^k \log_2 \frac{(\sum_{k=1}^{n} q_{i,j}^k)}{n}$$

$$\text{or, } -\frac{1}{n}\sum_{k=1}^{n} q_{i,j}^k \log_2(q_{i,j}^k) \leq -\frac{1}{n}\sum_{k=1}^{n} q_{i,j}^k \log_2 \frac{(\sum_{k=1}^{n} q_{i,j}^k)}{n}$$

$$\text{or, } |q_{i,j}\log_2(q_{i,j}) - \frac{1}{n}\sum_{k=1}^{n} q_{i,j}^k \log_2(q_{i,j}^k)| < |q_{i,j}\log_2(q_{i,j}) - \frac{1}{n}\sum_{k=1}^{n} q_{i,j}^k \log_2 \frac{(\sum_{k=1}^{n} q_{i,j}^k)}{n})| \tag{A.4}$$

For simplicity let's define $z = q_{i,j}$ and $z_n = \frac{1}{n}\sum_{k=1}^{n} q_{i,j}^k$. Also, let $G : (0, 1] \rightarrow R$ such that $G(z) = z\log_2(z)$. Clearly G is a continuous function in the range of z.

Using law of law of large numbers $z_n \rightarrow z$ in probability. Now continuous mapping theorem implies $G(z_n) \rightarrow G(z)$ in probability.

Let $z^k = q_{i,j}^k$, **we need to prove that** $\frac{1}{n}\sum_{k=1}^{n} G(z_k) \rightarrow G(z)$ in probability.

As $G(z_n) \rightarrow G(z)$ in probability,

$$\lim_{n\to\infty} P(|G(z) - G(z_n)| > \epsilon) = 0 \tag{A.5}$$

From Eqn. A.4,

$$|G(z) - G(z_n)| > |G(z) - \frac{1}{n}\sum_{k=1}^{n} G(z_k)|$$

Eqn. A.5 implies as $n \rightarrow \infty$,

$$|G(z) - G(z_n)| < \epsilon$$

$$\text{or, } |G(z) - \frac{1}{n}\sum_{k=1}^{n} G(z_k)| < |G(z) - G(z_n)| < \epsilon$$

Hence,

$$\lim_{n\to\infty} P(|G(z) - \frac{1}{n}\sum_{k=1}^{n} G(z_k)| > \epsilon) = 0 \tag{A.6}$$

Hence we prove that,

$\lim_{n\to\infty} P(\sum_{i,j} |(q_{i,j}\log_2(q_{i,j}) - \frac{1}{n}\sum_{k=1}^{n} q_{i,j}^k \log_2(q_{i,j}^k))| > K\epsilon) = 0$ where K is number of edges (constant)

Using the same inequality, it follows that,

$$\lim_{n\to\infty} P(|H_{opt} - \frac{1}{n}\sum_{k=1}^{n} H_k| > \epsilon) = 0$$

where $K\epsilon$ is replaced as ϵ. □

As a corollary, mean value of subject *sub-graph* entropies (H_k^r) also approaches group *sub-graph* (H_{opt}^r) entropy in probability, *i.e.*, for region r.

$$\lim_{n\to\infty} P(|H_{opt}^r - \frac{1}{n}\sum_{k=1}^{n} H_k^r| > \epsilon) = 0$$

S.11: Maximizing *Sub-Graph* Entropy is Equivalent to Maximizing Mutual Information

Proof. Notice that once we know the communication pattern for the whole graph, we also know the communication pattern for the *sub-graph*s. So, given G, the conditional entropy of *sub-graph* G_s given by $H(G_s|G)$ equals 0.

$$\begin{aligned} I(G; G_{v_s}) &= H(G_s) - H(G_s|G) \\ &= H(G_s), \text{ as } H(G_s|G) = 0 \end{aligned}$$

□

S.12: Correlation Coefficient as Edge Weight

Let x denote the fMRI time series from R regions of a subject for a state (task or no-task). It has size $R \times 1$ where R is regions. Also, let x_r be the time series from r^{th} region.

Theorem 2

Let the edge weight $e_{i,j} \sim Ber(\theta_{i,j})$ *where* $Ber(\theta)$ *is Bernoulli distribution with parameter* θ*. Here* $\theta_{i,j}$ *captures the relationship between regions* (i,j)*. Assume that,* $\mathbf{x} \sim N(0,\Sigma)$ *where* Σ *is covariance matrix with* $\Sigma(i,j) = \sigma_{i,j}$*, i.e.,* $\sigma_{i,j}$ *is* $(i,j)^{th}$ *entry of* Σ*. Then the minimum mean square error (MMSE) estimate of* $e_{i,j}$ *is given by* $\hat{e}_{i,j} = \sigma_{i,j}$*.*

Proof. The $(i,j)^{th}$ entry of Σ is given by $\sigma_{i,j} = E[x_i x_j]$. As x is Gaussian, the covariance captures all the information between the relation of two regions (i,j). Hence, $\theta_{i,j} = \sigma_{i,j}$.

To calculate the MMSE estimate, we note that $P(e_{i,j}) = \begin{cases} \theta_{i,j} \ if \ e_{i,j} = 1 \\ 1 - \theta_{i,j} \ if \ e_{i,j} = 0 \end{cases}$

In order to calculate the estimation, we minimize $E[(\hat{e}_{i,j} - e_{i,j})^2]$.

$$\begin{aligned} E[(\hat{e}_{i,j} - e_{i,j})^2] &= (1 - \hat{e}_{i,j})^2\theta + (0 - \hat{e}_{i,j})^2(1-\theta) = (1 - 2\hat{e}_{i,j})\theta + \hat{e}_{i,j}^2 \\ &= (\hat{e}_{i,j} - \theta)^2 + \theta(1-\theta) \geq (\hat{e}_{i,j} - \theta)^2 \text{ as } \theta \in [0,1]. \end{aligned}$$

Also, $E[(\hat{e}_{i,j} - e_{i,j})^2] \geq 0$. So, the value for which MMSE is minimum is achievable by $\hat{e}_{i,j}$ equal to $\theta_{i,j}$. Thus, $\hat{e}_{i,j} = \theta_{i,j} = \sigma_{i,j}$. □

Appendix B

Supplementary Information for Chapter 4

B.1 Tables

Table B.1: Top-25 regions for OCD *vs.* healthy data using 2-hop *differential node entropy*.

Rank	Region / Hemisphere	Diff. Entropy	p-value
1	**Accumbens Area** - L	1.4684	0.0243
2	**Amygdala** - R	1.4610	0.0629
3	**Caudate** - R	1.3656	0.0625
4	**Parstriangularis** - R	1.3561	0.0205
5	**Entorhinal** - L	1.3553	0.0808
6	**Parsopercularis** - R	1.3420	0.0080
7	**Pallidum** - L	1.3409	0.0876
8	**Parsorbitalis** - R	1.0792	0.0610
9	Brain Stem	1.0710	0.0667
10	**Thalamus Proper** - R	1.0226	0.1687
11	**Parsorbitalis** - L	1.0100	0.1618
12	**Lateral Orbitofrontal** - L	1.0079	0.0453
13	**Amygdala** - L	0.9857	0.2305
14	Temporal Pole - R	0.9572	0.2126
15	**Rostral Anterior Cingulate** - L	0.9556	0.0747
16	**Entorhinal** - R	0.9251	0.1188
17	**Lateral Orbitofrontal** - R	0.9178	0.1595
18	**Accumbens Area** - R	0.9163	0.1787
19	**Rostral Anterior Cingulate** - R	0.8364	0.0991
20	**Cuneus** - L	0.7759	0.0337
21	**Putamen** - L	0.7231	0.2933
22	**Caudal Anterior Cingulate** - R	0.7211	0.0860
23	Rostral MidFrontal - R	0.6511	0.1294
24	**Medial Orbitofrontal** - L	0.6466	0.0993
25	Parahippocampal - L	0.6445	0.3569

Table B.2: Leave-one-out classification results by predictive network *edge entropy* using 2-hop neighborhood.

	Features	Accuracy	Specificity	Sensitivity
Sub-network	110	**0.71**	**0.92**	**0.67**

Table B.3: Repeated cross-validation classification results with 5 test subjects

	Features	Accuracy	Specificity	Sensitivity
Edge Sub-network	120	**0.87**	**0.96**	**0.79**
Union Sub-graph	145	**0.87**	**0.96**	**0.79**
Intersection sub-graph	114	0.84	0.88	0.79
CSTC sub-network	120	0.76	0.87	0.64
Node entropy	85	0.71	0.64	0.79
Correlation	5	0.70	0.84	0.60
Network features	5	0.78	0.80	0.72
Correlation + Network features	10	0.79	0.86	0.73
NBS	95	0.68	0.55	0.77
Shannon wavelet entropy	85	0.54	0.39	0.65

Table B.4: Leave-one-out cross-validation classification results with different classifiers for edge sub-network. ANN had one hidden layer with 20 hidden nodes. Random forest classifier had 25 trees and max depth was 5 based on in-fold validation for hyperparameter tuning.

	Features	Accuracy	Specificity	Sensitivity
Support Vector Machine (SVM)	120	**0.89**	**1**	**0.80**
Linear Discriminant Analysis (LDA)	120	0.71	0.77	0.67
Artificial Neural Network (ANN)	120	0.85	0.92	0.80
Random Forest	120	0.79	0.85	0.73

Table B.5: Regions as part of predictive sub-network and CSTC network.

Number	Region/Hemisphere	Predictive Sub-network	CSTC Sub-network
1	Parsopercularis - R	Y	N
2	Thalamus Proper - R	Y	Y
3	Parsorbitalis - L	Y	N
4	Cuneus - L	Y	N
5	Accumbens Area - L	Y	N
6	Postcentral - L	Y	N
7	Parsorbitalis - R	Y	N
8	Pallidum - L	Y	Y
9	Medial Orbitofrontal - L	Y	Y
10	Parstriangularis - R	Y	N
11	Medial Orbitofrontal - R	Y	Y
12	Amygdala - R	Y	N
13	Hippocampus - L	Y	N
14	Lateral Orbitofrontal - L	Y	Y
15	Caudate - R	Y	Y
16	Rostral Anterior Cingulate - R	Y	Y
17	Rostral Anterior Cingulate - L	Y	Y
18	Lateral Orbitofrontal - R	Y	Y
19	Pericalcarine - R	Y	N
20	Caudal Anterior Cingulate - R	Y	Y
21	Entorhinal - L	Y	N
22	Frontal Pole - L	Y	N
23	Insula - L	Y	N
24	Putamen - R	Y	Y
25	Accumbens Area - R	Y	N
26	Accumbens Area- R	Y	N
27	Hippocampus - R	Y	N
28	Pallidum - R	Y	Y
29	Parsopercularis - L	Y	N
30	Parstriangularis - L	Y	N
31	TemporalPole - L	Y	N
32	Entorhinal - R	Y	N
33	Brain Stem	Y	N
34	Putamen - L	N	Y
35	Thalamus Proper - L	N	Y
36	Caudate - L	N	Y
37	Caudal AntCingulate - L	N	Y

Table B.6: Top-50 edges as part of predictive sub-network and CSTC network.

Number	Edge		Predictive Sub-network	CSTC Sub-network
1	MedOrbitofrontalR	RostralAntCingulateR	Y	Y
2	ParsorbitalisL	ParstriangularisR	Y	N
3	ParsorbitalisL	ParsorbitalisR	Y	N
4	PallidumL	ThalR	Y	Y
5	TemporalPoleL	ParsopercularisR	Y	N
6	AccumbL	EntorhinalL	Y	N
7	AccumbL	ParsorbitalisL	Y	N
8	ParsopercularisR	ParstriangularisR	Y	N
9	CaudateL	ThalR	Y	Y
10	ThalR	CaudAntCingulateR	Y	Y
11	PallidumL	RostralAntCingulateL	Y	Y
12	ThalR	MedOrbitofrontalL	Y	Y
13	ThalR	MedOrbitofrontalR	Y	Y
14	ThalR	PallidumR	Y	Y
15	PallidumL	MedOrbitofrontalR	Y	Y
16	AccumbL	ParsopercularisR	Y	N
17	AmygdalaR	ParsopercularisR	Y	N
18	ParsopercularisR	TemporalPoleR	Y	N
19	ParsopercularisR	ParsorbitalisR	Y	N
20	PallidumL	LatOrbitofrontalL	Y	Y
21	ThalR	RostralAntCingulateL	Y	Y
22	CaudateR	MedOrbitofrontalR	Y	Y
23	MedOrbitofrontalL	LatOrbitofrontalR	Y	Y
24	LatOrbitofrontalR	MedOrbitofrontalR	Y	Y
25	CaudateR	MedOrbitofrontalL	Y	Y
26	PallidumL	CaudateR	Y	Y
27	PallidumL	ParsopercularisR	Y	N
28	ParsorbitalisR	FrontalPoleR	Y	N
29	RostralAntCingulateL	ParsopercularisR	Y	N
30	AmygdalaL	ParsopercularisR	Y	N
31	PallidumR	ParsopercularisR	Y	N
32	ParsorbitalisL	ParsopercularisR	Y	N
33	EntorhinalR	ParsopercularisR	Y	N
34	PallidumR	MedOrbitofrontalR	Y	Y
35	PallidumL	MedOrbitofrontalL	Y	Y
36	ThalR	RostralAntCingulateR	Y	Y
37	CaudateL	PallidumL	Y	Y
38	PallidumL	RostralAntCingulateR	Y	Y
39	PallidumL	CaudAntCingulateR	Y	Y
40	EntorhinalL	ParsopercularisR	Y	N
41	AccumbensR	ParsopercularisR	Y	N
42	RostralAntCingulateL	RostralAntCingulateR	Y	Y
43	ParsopercularisR	FrontalPoleR	Y	N
44	ThalR	CaudAntCingulateL	Y	Y
45	PallidumR	MedOrbitofrontalL	Y	Y
46	ThalR	CaudateR	Y	Y
47	BrainStem	ParsopercularisR	Y	N
48	AmygdalaR	ParsorbitalisL	Y	N
49	ThalR	ParsorbitalisL	Y	N
50	FrontalPoleL	ParsopercularisR	Y	N

B.2 Illustrations

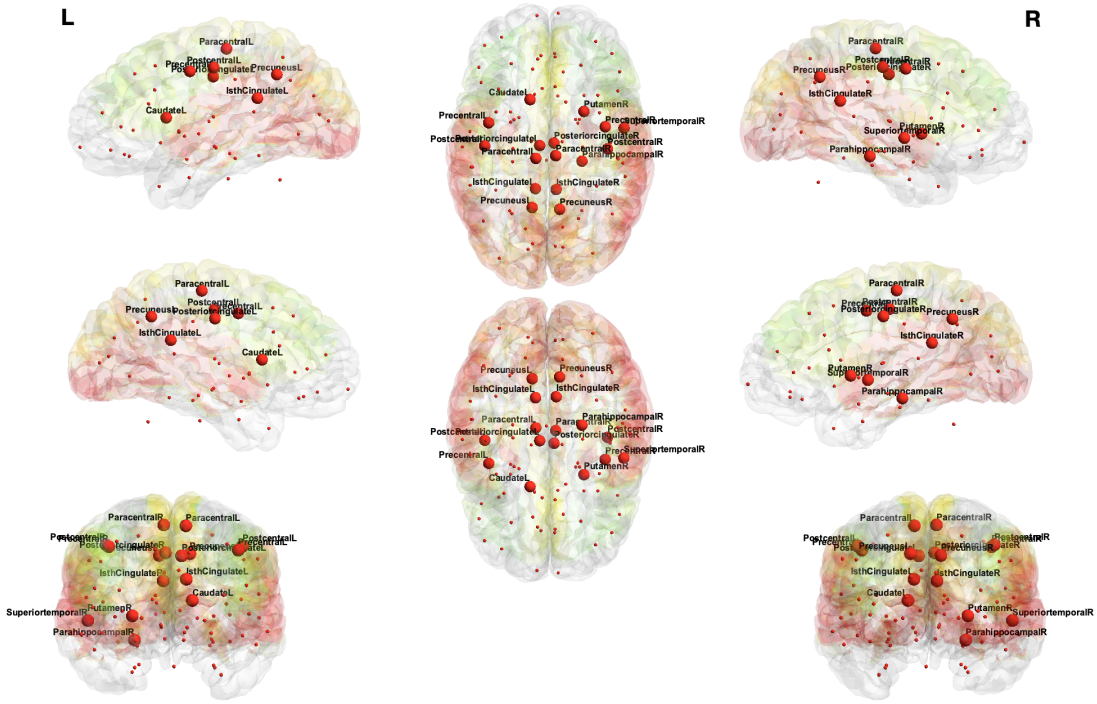

Figure B.1: Regions with significantly different ($p < 0.05$) *univariate* features based on Shannon wavelet entropy.

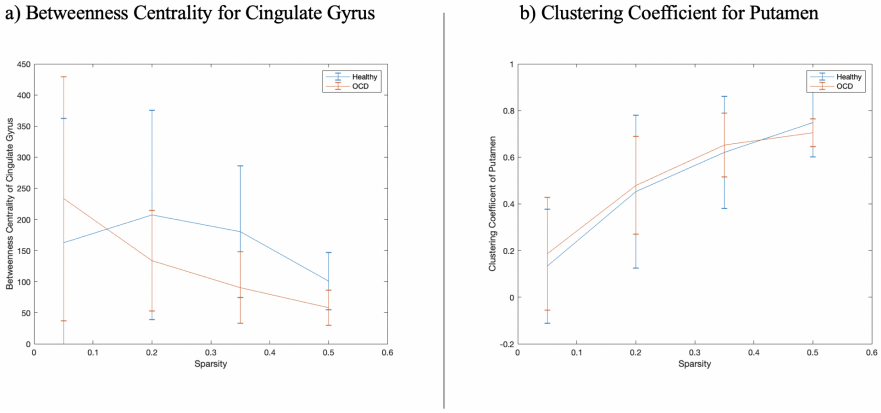

Figure B.2: Network features *metric* at different sparisity levels a) betweenness centrality for cingulate gyrus b) clustering coefficient for putamen. These two features are selected to be most important using feature selection using mRMR.

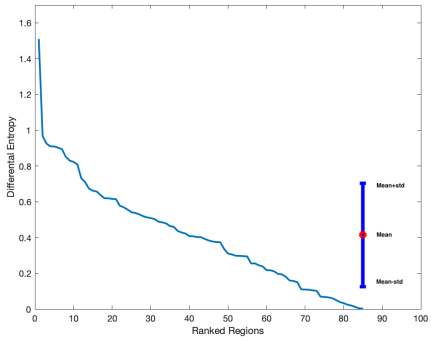

Figure B.3: *Differential node entropy* value of sorted regions for two groups of subjects (OCD *vs*. healthy). Mean value and standard deviation is also shown in right. The X-axis represents ranked region.

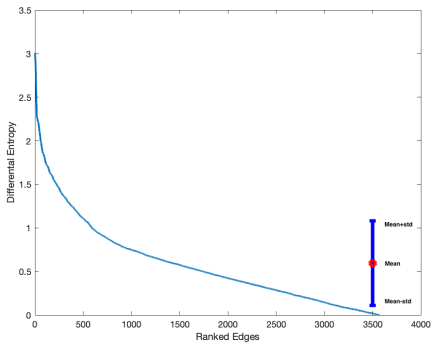

Figure B.4: *Differental edge entropy* value of sorted edges for two groups of subjects (OCD *vs*. healthy).

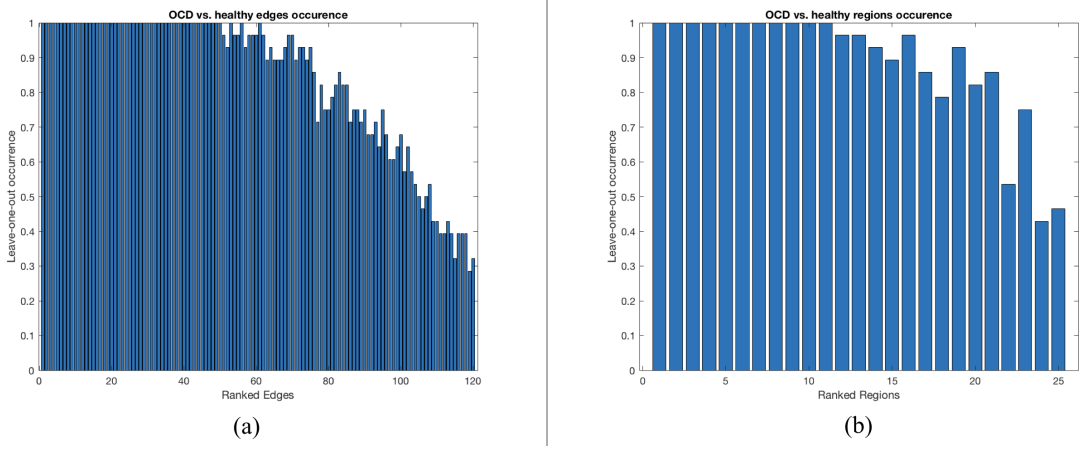

Figure B.5: Histogram of the edges and regions captured by leave-one-out training. The X-axis represents edges/regions with corresponding rank.

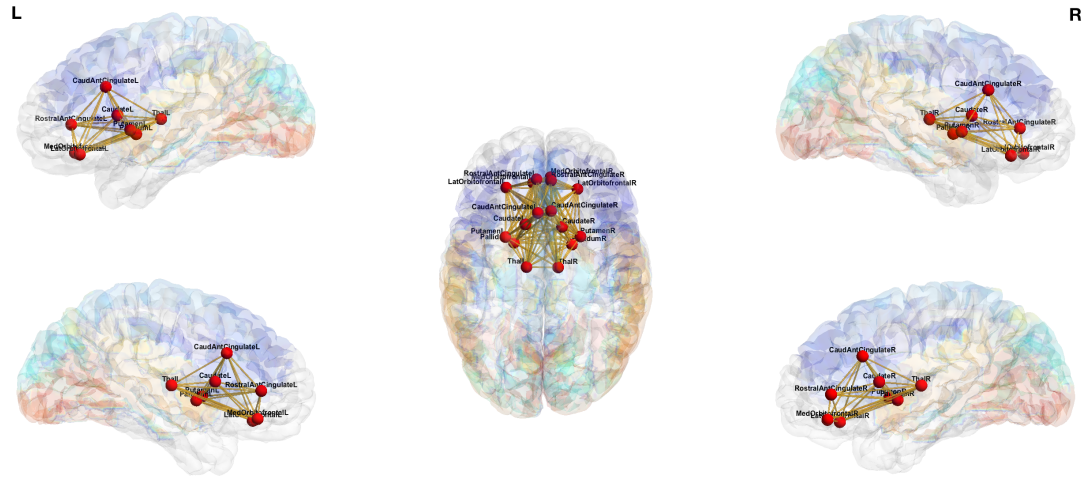

Figure B.6: An illustration of cortico-striato-thalamo-cortical (CSTC) network.

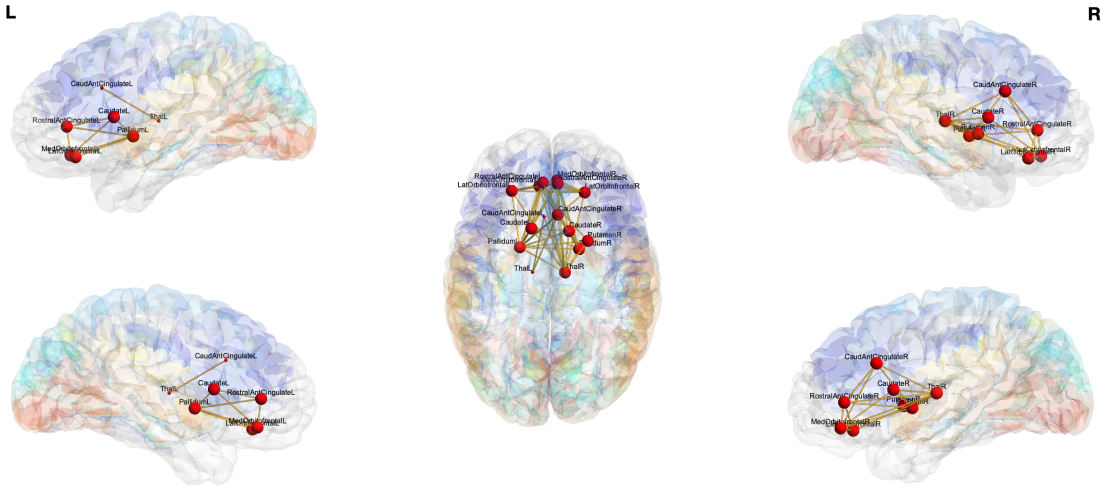

Figure B.7: Intersection sub-network containing common regions and edges between Predictive and CSTC network.

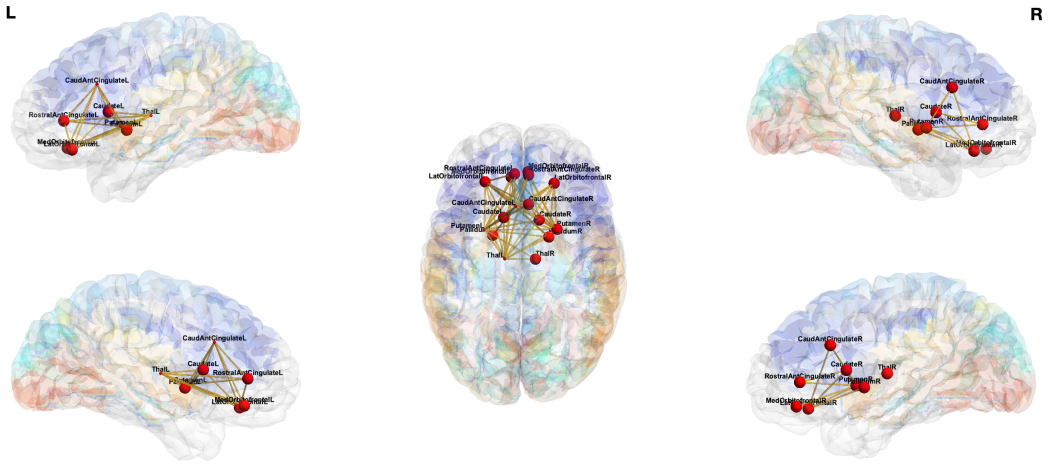

Figure B.8: Sub-network containing edges from CSTC not present in intersection sub-network in Fig. S7.

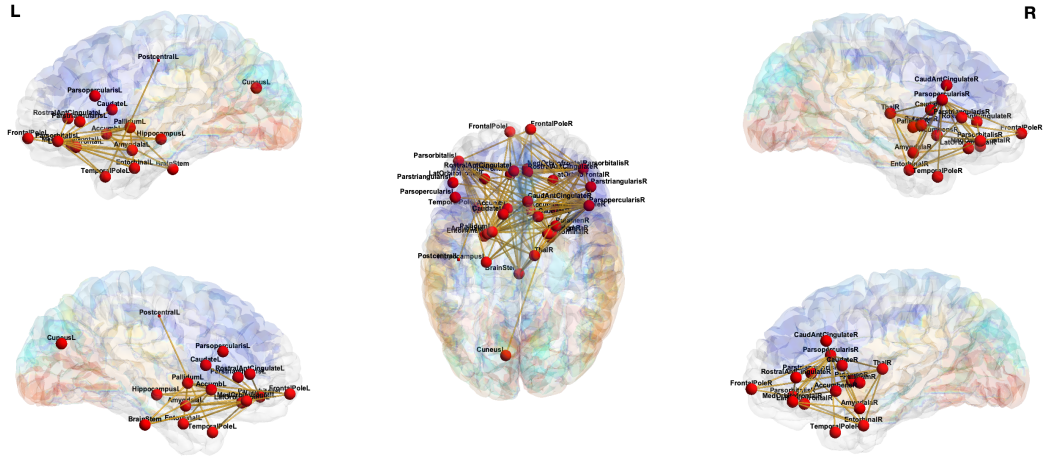

Figure B.9: Sub-network containing edges from predictive sub-network not present in intersection sub-network in Fig. S7.

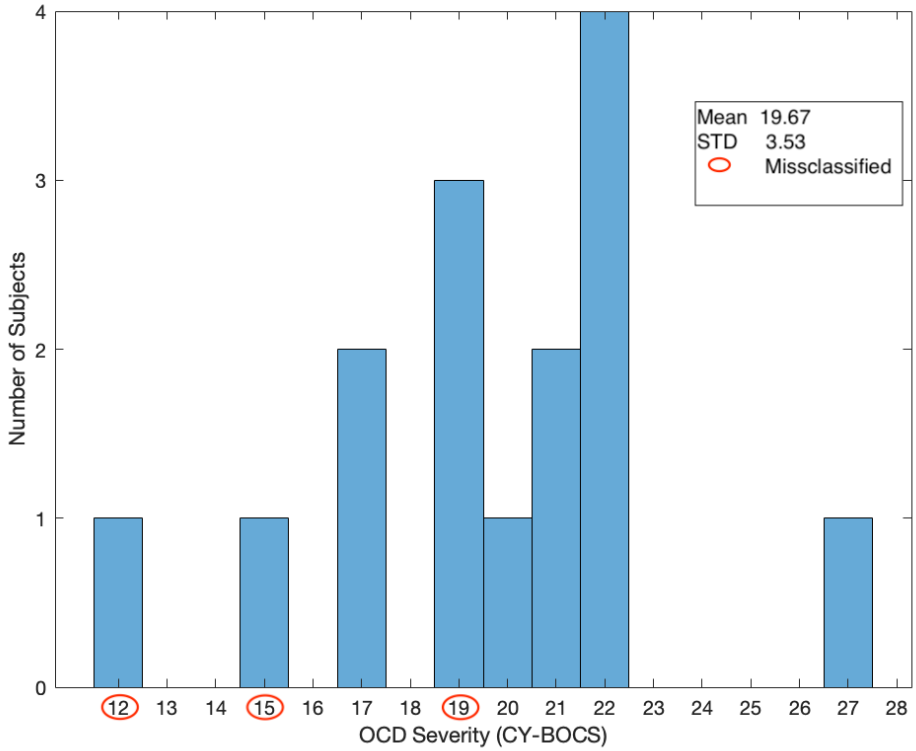

Figure B.10: Histogram of the OCD severity (CY-BOCS) for patient group. The score varies between 12-27. Three subjects were misclassified by the classifier and the scores are shown in red cicle.

Appendix C

Supplementary Information for Chapter 5

C.1 Tables

Table C.1: 5-Fold cross validation classification results for biological gender classification using different decomposition techniques from dFC (for 264 regions).

	Features	Task	Accuracy	Sensitivity	Specificity
Tensor (Proposed)	Combined	25	**0.94**	**0.96**	**0.88**
ICA	Combined	75	0.7	0.56	0.84
PCA	Combined	75	0.5	0.51	0.49

Table C.2: 5-Fold cross validation regression results for predicting IQ using different decomposition techniques from dFC (for 264 regions).

	Fluid Intelligence					Fluid Ability Metrics				
	Task	Features	MSE	MAE	SD	Task	Features	MSE	MAE	SD
Tensor (Proposed)	Combined	25	**0.1313**	**5.05**	0.3	Combined	25	**0.0306**	**14.1**	1.21
ICA	Combined	75	0.4661	10.12	2.8	Combined	75	0.0414	17.81	2.2
PCA	Combined	75	0.5321	12.34	4.1	Combined	75	0.0866	30.79	4.97

C.2 Illustrations

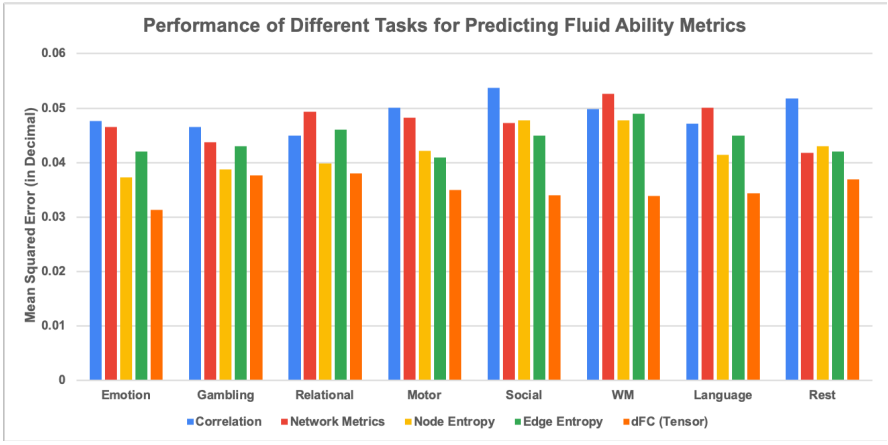

Figure C.1: Average 5-fold cross-validation normalized mean square error for each task employing different feature engineering techniques to predict fluid ability metrics. The normalized mean square error performance for different features in Table 5.3 are shown for each task. Here less the height of the bar, better the performance. Our proposed dFC (Tensor) always performs within top two methods for predicting biological gender.

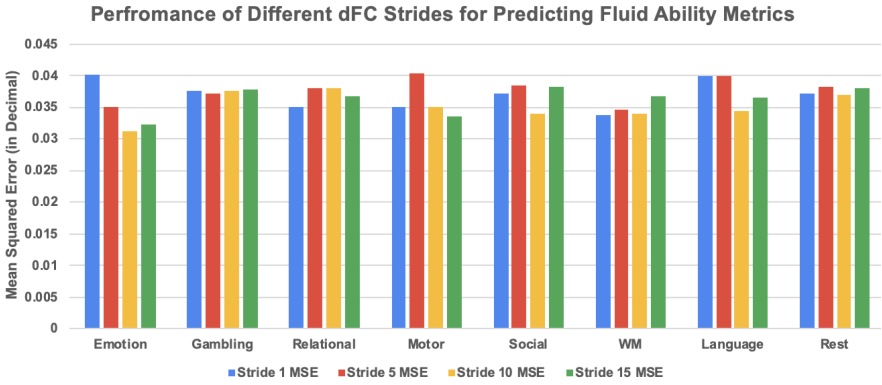

Figure C.2: Average 5-fold cross-validation normalized mean square error to predict fluid ability metrics for each task employing different sliding window strides for calculating dFC. Here less the height of the bar, better the performance. Stride 10 yields best accuracy most of the times.

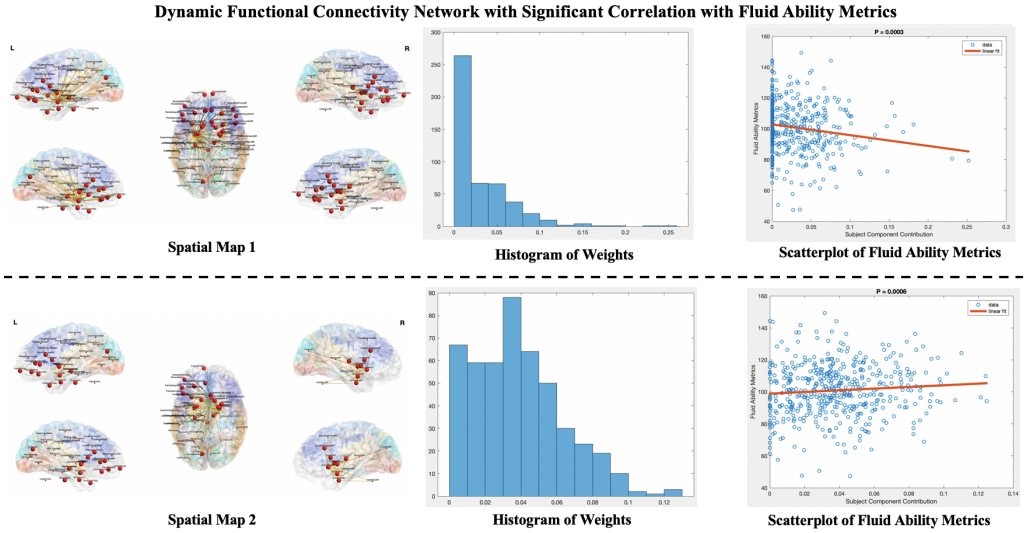

Figure C.3: Statistically significant spatial components along with the weight distributions for correlating with fluid ability metrics. *Left*: Spatial map with top 5% connectivity values. *Middle*: histogram of the weight loading for all subjects. Most of the subjects have non-zero values for weights signifying that this network is present in most of the subject. *Right*: scatter plot with correlation curve and corresponding p-values for individual weights.

Appendix D

Supplementary Information for Chapter 6

Illustrations

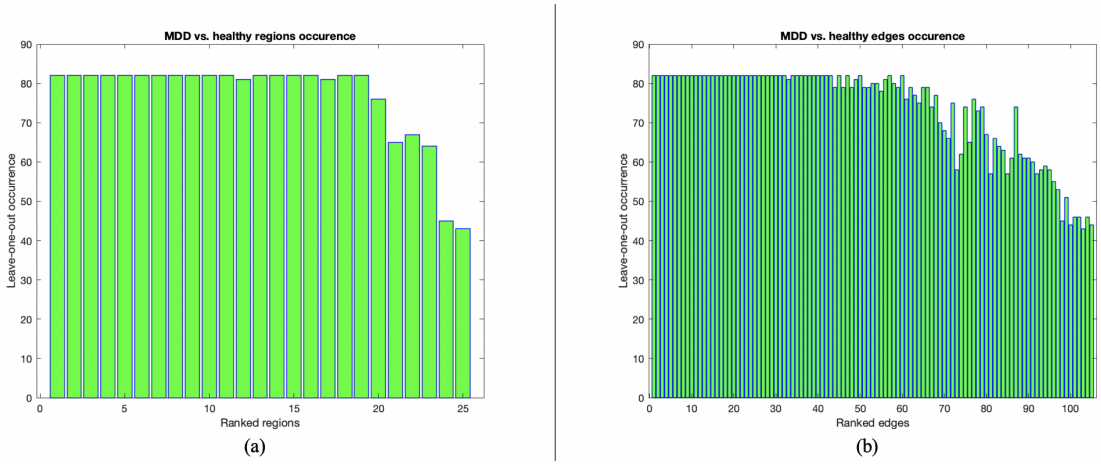

Figure D.1: Histogram of the edges and regions captured by leave-one-out training. X-axis represents edges/regions with corresponding rank.

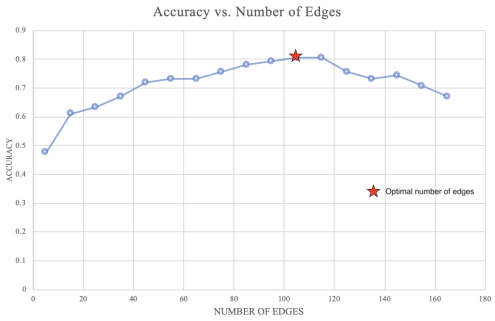

Figure D.2: Leave-one-out accuracy *vs*. number of edges in sub-network.

Tables

Table D.1: Top-25 edges extracted using *differential edge entropy* for MDD *vs*. healthy data.

Rank	Region - 1 / Hemisphere - 1	Region - 2/ Hemisphere - 2	Diff. Entropy	p-value
1	Parsorbitalis - L	Temporal Pole - L	1.0945	0.0034
2	Putamen - L	Pallidum - L	1.0005	0.0147
3	Putamen - L	Entorhinal - R	0.9815	0.0060
4	Pallidum - L	BrainStem	0.9507	0.0334
5	Parsorbitalis - L	FrontalPole - R	0.9502	0.0160
6	Putamen - L	Pallidum - R	0.9490	0.0156
7	TemporalPole - L	FrontalPole - R	0.9298	0.0451
8	Pallidum - R	Accumbens - R	0.9109	0.0355
9	Putamen - L	BrainStem	0.8798	0.0079
10	Caudate - L	Bankssts - L	0.8707	0.0070
11	BrainStem	Pallidum - R	0.8684	0.0555
12	Accumbens - R	Entorhinal - R	0.8314	0.0679
13	Pallidum - L	Pallidum - R	0.8242	0.1002
14	Putamen - L	IsthCingulate - L	0.8178	0.0011
15	Thalamus - L	Putamen - L	0.8056	0.0153
16	Putamen - L	Entorhinal - L	0.8003	0.0278
17	Bankssts - L	Temporal Pole - L	0.7894	0.0439
18	Pallidum - R	Entorhinal - L	0.7712	0.0947
19	Putamen - L	Putamen - R	0.7707	0.0381
20	Putamen - L	Amygdala - R	0.7580	0.0235
21	Pallidum - R	IsthCingulate - L	0.7566	0.0032
22	Putamen - R	Pallidum - R	0.7552	0.0471
23	Putamen - R	Temporal Pole - R	0.7501	0.0449
24	Pallidum - L	IsthCingulate - L	0.7455	0.0052
25	Putamen - L	Temporal Pole - R	0.7448	0.0371